

THESIS FOR THE DEGREE OF DOCTOR OF PHILOSOPHY

Alloy Design for Refractory Alloys with Balancing Mechanical Properties and
Oxidation Resistance

XIAOLONG LI



Department of Industrial and Materials Science

CHALMERS UNIVERSITY OF TECHNOLOGY

Gothenburg, Sweden 2025

Alloy Design for Refractory Alloys with Balancing Mechanical Properties and Oxidation Resistance

XIAOLONG LI

© Xiaolong Li, 2025

ISBN: 978-91-8103-210-9

Doktorsavhandlingar vid Chalmers tekniska högskola

Ny serie nr 5668

ISSN 0346-718X

Department of Industrial and Materials Science

CHALMERS UNIVERSITY OF TECHNOLOGY

SE-41296 Gothenburg, Sweden

Tel: +46 (0) 31-7721000

Cover image:

Next generation high temperature alloys

Printed by Chalmers Reproservice

Gothenburg, Sweden 2025

Dedicated to:

Those of you who are struggling for a PhD

Alloy Design for Refractory Alloys with Balancing Mechanical Properties and Oxidation Resistance

XIAOLONG LI

Department of Industrial and Materials Science
Chalmers University of Technology

Abstract

Refractory alloys including refractory high entropy alloys (RHEAs) and conventional refractory alloys (CRAs) hold great potential as ultrahigh-temperature structural materials ($\geq 1300^\circ\text{C}$), since they are equipped with high melting points enabling the high service temperature, metallic bonding sustaining the ductility, and the single body-centered cubic (bcc) structure ensuring the microstructural and thermal stability. However, alloy design of refractory alloys to simultaneously possess three critical materials requirements for ultrahigh-temperature applications, i.e., excellent high-temperature (HT) strength (Target 1), acceptable room temperature (RT) ductility (Target 2) and decent oxidation resistance (Target 3), is highly challenging which triggers the well-known ‘trade-off’ phenomenon in the alloy development. Thus, innovative strategies are desperately in need, and they constitute the topic of this doctoral thesis. The roadmap of alloy design in this doctoral thesis is to tackle two out of three challenges first, and eventually to tackle three challenges simultaneously.

Firstly, following this roadmap, solid solution softening (SSS) at RT and solid solution hardening (SSH) at HT, were employed to balance the strength at HT (Target 1) and the ductility at RT (Target 2). The softening effect at RT induced by minor substitutional additions of Mn, Al and Cu was identified in an originally ductile RHEA. Next, Mn as the most effective softener was added into an originally brittle RHEA, achieving a simultaneous SSS at RT and SSH at HT. Referring to the yield strength-temperature curve of bcc structured alloys characterized by a three-stage pattern: a temperature-dependent decrease at the low temperature regime, followed by a temperature-independent plateau at the intermediate temperature regime, and finally a temperature-dependent drop at the HT regime, our strategy enabled a reduced temperature dependence of yield strength in bcc-structured RHEAs.

Secondly, Nb alloys were alloyed with Al to balance the oxidation resistance (Target 3) and the RT ductility (Target 2). Although pesting was observed basically in all tested oxidation conditions suggesting the formation of non-protective oxide scales, the oxidation resistance of Nb alloys was significantly improved due to the beneficial effect of Al addition and was much superior to that of the benchmark WC3009 alloy.

Thirdly, an attempt was made to simultaneously meet the ultimate goal of this work: to balance strength at HT (Target 1), ductility at RT (Target 2) and oxidation resistance (Target 3) in Nb-based alloys. The alloying effect of Hf, W and Ti on the mechanical properties at both room-temperature and high-temperatures, the oxidation resistance, and more importantly their balance was explored. Novel Nb alloys were developed, with their oxidation resistance much superior compared to that of the benchmark C103 and WC3009 alloys, together with a reasonably high yield strength at HT.

Key words: Alloy design; refractory high-entropy alloys; refractory alloys; high temperature strength; room temperature ductility; temperature dependence of yield strength; solid solution softening and hardening; oxidation resistance.

Preface

This doctoral thesis is performed at the Department of Industrial and Materials Science at Chalmers University of Technology during the period of September 2020 to May 2025. This work is funded by Swedish Research Council (grant number 2019-03559) and carried out under the main supervision of Professor Sheng Guo and the co-supervision of Dr. Huahai Mao, with Professor Uta Klement as the examiner.

List of Appended Papers

Paper I: Xiaolong Li, Jin Lu, Huahai Mao, Hideyuki Murakami, Sheng Guo, Solid solution softening or hardening induced by minor substitutional additions in a $\text{Hf}_{20}\text{Nb}_{31}\text{Ta}_{31}\text{Ti}_{18}$ refractory high entropy alloy. *AIP Advances*, 13, 085033 (2023).

Paper II: Xiaolong Li, Mao Ding, Qiang Hu, Zhiyuan Liu, Huahai Mao, Sheng Guo, Solid solution softening at room temperature and hardening at elevated temperatures: A case by minor Mn addition in a $(\text{HfNbTi})_{85}\text{Mo}_{15}$ refractory high entropy alloy. *Mater. Res. Express*, 10, 116501 (2023).

Paper III: Xiaolong Li, Yufei Zhao, Huahai Mao, Sheng Guo, Effect of Al addition on oxidation behavior at elevated temperatures of Nb-based refractory alloys. *AIP Advances*, 15, 045012 (2025).

Paper IV: Xiaolong Li, Huahai Mao, Farid Akhtar, Sheng Guo, Balancing mechanical properties and oxidation resistance of Nb-based refractory alloys: the alloying effect of Hf, W and Ti, manuscript submitted.

Contribution of thesis's author to the appended papers

Paper I: Conceptualization, sample preparations, characterization, testing, and data analysis. First draft of the manuscript, with input and revision by all co-authors.

Paper II: Conceptualization, sample preparations, characterization, testing, and data analysis. First draft of the manuscript, with input and revision by all co-authors.

Paper III: Conceptualization, sample preparations, part of the characterization and data analysis. First draft of the manuscript, with input and revision by all co-authors.

Paper IV: Conceptualization, sample preparations, characterization, testing, and data analysis. First draft of the manuscript, with input and revision by all co-authors.

Paper not included in the thesis.

Paper I: D. Mishra, A. Dhal, **XL. Li**, S. Guo, R.L. Narayan, R.S. Mishra, J. Singh, S.S. Nene. "Phase separation induced heterostructure promotes strength-ductility synergy in Cu-rich compositionally complex alloy in as-cast state." *Materials Today Communications* 44 (2025): 112020.

Paper II: XY. Sun, **XL. Li**, S. Guo, L. Zhu, J. Teng, L. Jiang, J. Moverare, XH. Li, RL. Peng. "The impact of Al/Cr ratio on the oxidation kinetics of Y-doped AlCoCrFeNi high-entropy alloys at 1100°C." *Intermetallics* 176 (2025): 108582.

Paper III: S.R. Reddy, **XL. Li**, S. Guo, P.P. Bhattacharjee, A.H. Chokshi. "High Strain Rate Superplastic Flow and Fracture Characteristics of a Fine-Grained Eutectic High Entropy Alloy." *Metallurgical and Materials Transactions A* 55, no. 1 (2024): 173-182.

Paper IV: A.R. Balpande, S. Agrawal, **XL. Li**, S. Suwas, S. Guo, P. Ghosal, S.S. Nene. "Excellent specific strength-ductility synergy in novel complex concentrated alloy after suction casting." *Materials & Design* 242 (2024): 112988.

Paper V: XY. Sun, **XL. Li**, S. Guo, X. Yu, L. Zhu, J. Teng, L. Jiang, J. Moverare, XH. Li, RL. Peng. "Revealing microstructural degradation mechanism induced by interdiffusion between Amdry365 coating and IN792 superalloy." *Materials & Design* 241 (2024): 112937.

Table of Contents

1	Introduction	1
1.1	Background	1
1.2	Research goals	2
2	Refractory alloys: Refractory high-entropy alloys (RHEAs) and conventional refractory alloys (CRAs).....	5
2.1	Refractory high-entropy alloys (RHEAs).....	5
2.2	Conventional refractory alloys (CRAs)	8
3	Roadmap	12
3.1	Strength at high temperatures (Target No.1)	12
3.1.1	Solid solution hardening (SSH).....	12
3.1.2	Secondary phase strengthening.....	17
3.2	Ductility at room temperature (Target No.2)	23
3.2.1	Valence electron concentration (VEC) engineering.....	24
3.2.2	Transformation induced plasticity (TRIP).....	25
3.2.3	Solid solution softening (SSS).....	26
3.3	Oxidation resistance (Target No.3)	32
3.3.1	Thermodynamics of oxidation	32
3.3.2	Kinetics of oxidation.....	34
3.3.3	Complex oxides	36
3.3.4	Surface coating.....	38
4	Experimental method	41
4.1	Arc-melting.....	41
4.2	Vickers hardness measurement.....	41
4.3	Oxidation test.....	42
4.4	High temperature hardness test.....	42
4.5	Universal compression test at room temperature	42
4.6	Gleeble compression test at high temperatures	43
4.7	X-ray diffraction	43
4.8	Microstructural investigation.....	43
5	Summary of key results.....	45
5.1	Trade-off of ductility at RT and strength at HT: Solid solution softening (SSS) and/or solid solution hardening (SSH).....	45
5.1.1	Minor substitutional additions into originally ductile RHEAs: A case for $\text{Hf}_{20}\text{Nb}_{29.75}\text{Ta}_{29.75}\text{Ti}_{18}\text{-X}_{2.5}$ at% (X=Mn, Al, Cu, Fe).....	45
5.1.2	Minor Mn addition into originally brittle RHEAs: A case for $(\text{TiHfNb})_{85}\text{Mo}_{15}\text{Mn}_{(0.03-2 \text{ at}\%)}$	47

5.2	Trade-off between oxidation resistance and ductility at RT: Alloying Nb alloys with Al.....	49
5.3	Trade-off among ductility at RT, strength at HT, and oxidation resistance: Alloying Nb alloys with Hf, W and Ti	51
5.4	Trade-off between ductility and strength at RT: An unexpected effect of oxygen	55
6	Conclusions and future prospects.....	57
7	Acknowledgements.....	61
8	References	63

1 Introduction

1.1 Background

The quest for new ultrahigh-temperature materials is driven by the need to improve the efficiency of aerospace and power-generation gas turbine engines, by operating at higher temperatures (HT). The hotter the engine, the better [1]! For decades, turbine engines have been heavily relying on the development of state-of-the-art Ni-based superalloys (see Figure 1.1a), which have evolved during a period of 80 years through small incremental changes. Ni-based superalloys have various favorable properties enabling them to operate at HT: high tensile strength and more importantly can retain a high level of strength at HT; sufficiently high ductility to be shaped mechanically; can nicely resist oxidation, creep and fatigue. The materials development for Ni-base superalloys witnesses a steady increase in engine operating temperatures and hence improved performance and efficiency. However, operating temperatures for Ni-base superalloys are now approaching the limit set by their melting temperatures (T_m). More specifically, components made by Ni-based superalloys in jet engines can reach temperatures close to 1150°C, just around 200°C below their T_m . Complex cooling systems and protective thermal barrier coatings can enable Ni-base superalloys to exist at HT, like the gas temperatures within the turbines (close to 1500°C), but this is undesirable at the cost of much reduced efficiency. It is estimated that, if engines can operate without auxiliary cooling at about 1300°C, an almost 50% increase in output power could be achieved [1] (see Figure 1.1b), which greatly motivates the development of new ultrahigh-temperature materials replacing Ni-base superalloys to realize more efficient engines.

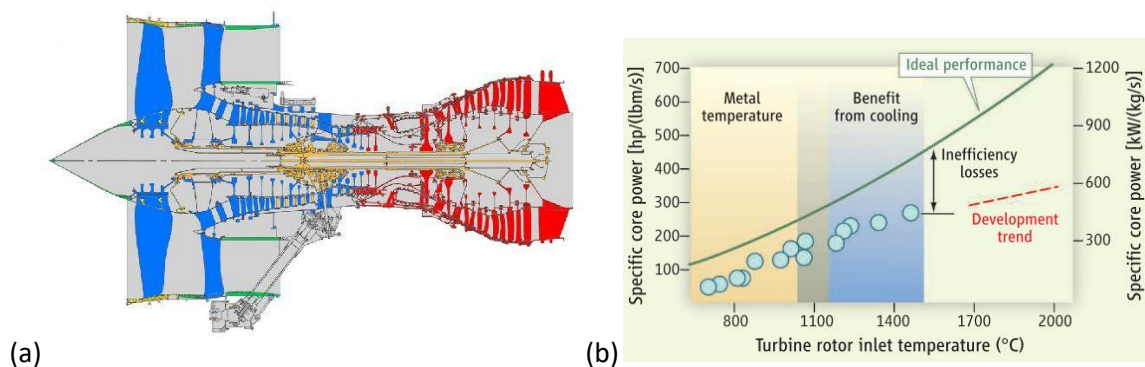


Figure 1.1. (a) Jet engine materials. Components in red are made of Ni-based superalloys where operation temperatures are the highest. (b) Specific core power versus turbine inlet temperature for gas turbine engines.

Reproduced from Ref. [1], with the permission of American Association for the Advancement of Science.

Nevertheless, the choices of alternative materials are very limited, due to the numerous demanding performance criteria that need to be met. The foremost criterion is certainly the high T_m , which is the preliminary condition for alloys to be used at HT. One particular guideline for alternative materials is

the Johnson relation, which suggests that the T_m of the materials should be above 2500°C in order to be used as turbine blades without any protection and cooling [2]. Another criterion is creep property, or the slow deformation under stress, since for example turbine blades are subjected to stress from centrifugal force. A lower creep rate, which is desirable for engine materials, can again be translated into higher maximum operating temperatures. Room temperature (RT) ductility enables alloys to be manufactured conveniently. In addition, oxidation resistance is another issue considering the working environment of alloys, especially when it comes to HT. Unfortunately, meeting one materials requirement for HT applications in many cases is at the expense of other expected merits, similar to the intrinsic ductility-strength trade-off existing in almost all metallic materials. This type of conflict is exactly behind the rather slow materials development of HT alloys. Currently, there are only a limited number of ceramics, intermetallic compounds and refractory (meaning high melting points) metals/alloys that can potentially meet the materials requirements to work at HT. Ceramic and intermetallic compounds have good oxidation resistance and low density, but they tend to suffer from severe embrittlement issues making them unacceptably prone to failure. Refractory metals and alloys, particularly Mo and Nb alloys, are considered as alternative materials to Ni-based alloys which can satisfy many of the materials requirements for engine applications [3]. Unfortunately, they still suffer from room temperature brittleness and/or insufficient oxidation resistance, with almost no success in achieving RT ductility after nearly 60 years of intensive research efforts [4]. Thereby, development and exploration of novel ultrahigh-temperature materials which would ideally operate at HT without the need for auxiliary cooling, will contribute to more efficient turbine engines and less pollution, and to the sustainable energy system worldwide.

1.2 Research goals

When it comes to the materials selection for ultrahigh temperatures applications, refractory alloys stand out due to their high T_m ensuring a high service temperature and the metallic bonding potentially sustaining the ductility at RT (when compared with directional bonding in ceramics and intermetallic compounds). However, the insufficient oxidation resistance could always be problematic and their known tendency to RT embrittlement (before and/or after strengthening) is another important concern. In this thesis work, we identify three most important material requirements (challenges) for refractory alloys to be considered for HT applications, i.e., strength at HT (Target No.1), ductility at RT (Target No.2) and oxidation resistance (Target No.3). How to balance their mechanical properties and oxidation resistance to develop novel refractory alloys for HT applications becomes a scientifically challenging research topic.

Here in this thesis work, we proposed a roadmap to tackle the three challenges and eventually to achieve the 3 set Targets. The roadmap is to tackle two out of three challenges first, and eventually to

tackle three challenges simultaneously. Both refractory high entropy alloys (RHEAs) and conventional refractory alloys (CRAs) were investigated. Conflict between strength at HT and ductility at RT was the first challenge to tackle, followed by conflict between oxidation resistance and ductility at RT, and eventually the challenge was the balance among strength at HT, ductility at RT and oxidation resistance.

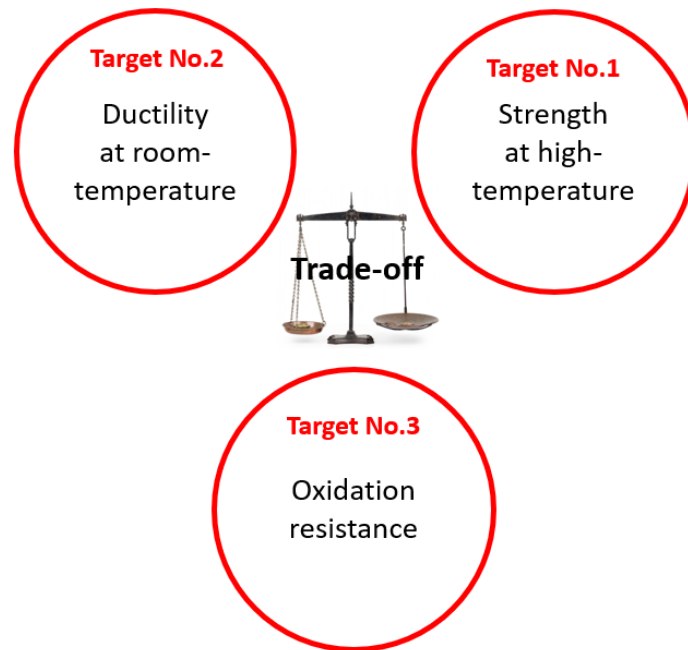


Figure 1.2. Proposed outline with the set research goals for the thesis work

2 Refractory alloys: Refractory high-entropy alloys (RHEAs) and conventional refractory alloys (CRAs)

2.1 Refractory high-entropy alloys (RHEAs)

HEAs is a paradigm-shift alloy design concept! Conventional alloys including Ni-based superalloys or steels, are typically based on one principal/major element, like Ni or Fe. The recently emerging new type of advanced metallic alloy, HEAs [5], [6], [7], however, provides a paradigm-shift in the alloy design strategy that significantly expands the scope for the exploration of new alloy systems and compositions. There are also several different terms used by researchers in the field when addressing HEAs, such as multi-principal-element alloys (MPEAs) and compositionally complex alloys (CCAs) [8], [9]. HEAs typically consist of at least four principal metallic elements in near-equiatomic ratios and therefore have a higher configuration entropy [10], [11] than that of conventional alloys (this explains why they are termed as HEAs), which can significantly decrease the Gibbs free energy, G , and hence lead to the stabilization of the solid solution phase rather than intermetallic compounds [12], especially at high temperatures, T . Thermodynamically, the role of high entropy can be readily explained by the following equation:

$$G_{mix} = H_{mix} - TS_{mix}$$

Here, G_{mix} , H_{mix} and S_{mix} are the mixing Gibbs free energy, mixing enthalpy and total mixing entropy (S_{mix} , dominated by the configuration entropy in many, if not most cases), respectively. In the literature, HEAs are claimed to differ from conventional alloys by exhibiting the following four distinct characteristics [13], which are however not all supported by experimental evidence and hence shall be taken with caution:

1) High-entropy effect:

Compared with traditional alloys with one major element such as Fe in steels, HEAs comprise of at least five major elements with equi- or near equi-atomic ratio, therefore they have high configurational entropy helping to stabilize the solid solution phase. In many cases, a single solid solution phase is formed in HEAs, which is against what the traditional Gibbs phase rule dictates. Most frequently, there are three types of solid solutions that are formed in HEAs, distinguished by their crystal structures: ① Face-centered-cubic (fcc) solid solution, made from 3d transition metals, such as the Cantor alloy CoCrFeMnNi [14]; ② Body-centered-cubic (bcc) solid solution, made from refractory metals, such as Senkov alloys MoNbTaVW [15] and HfNbTaTiZrTi [16]; ③ Hexagonal close-packed (hcp) [17] solid solution, mainly made from rare-earth elements.

2) Severe lattice distortion

In HEAs, the concepts of solutes and solvents do not apply anymore. Atomic sizes of constituent elements are different, which makes the atomic positions drifting relative to the ideal ones within a certain range, thus causing the lattice distortion. It was claimed that lattice distortions in HEAs are severe and will cause strong solid solution strengthening (SSS) effect.

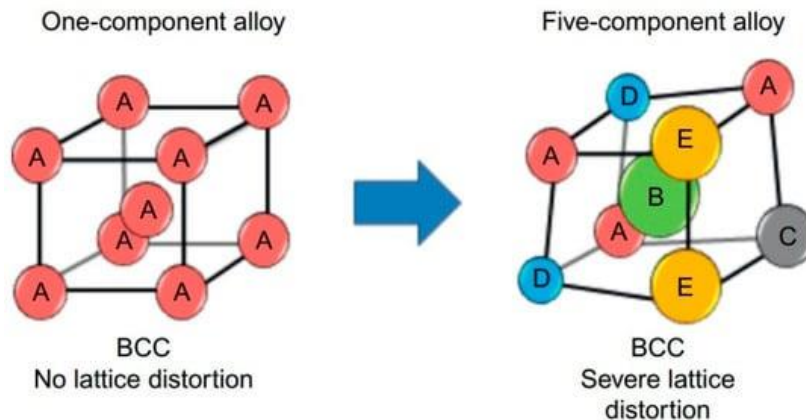


Figure 2.1. Schematic illustration of lattice distortion in BCC-type solid solution forming HEAs

3) Sluggish diffusion

If the lattice is indeed severely distorted, any crystalline defects such as vacancies, dislocations and interfaces, must experience this rough landscape with lattice friction when they want to move, resulting in a decrease in diffusional coefficient of elements thus hindering the solid-state phase transformations. This claim is however the most controversial one among the four core effects for HEAs [18].

4) Cocktail effect

Besides all the contributions from individual elements, the compositional complexity of HEAs might result in a complex outcome, even more significant than that of just a simple sum of all constituents.

Due to their unique features notably including high strength, high softening resistance at elevated temperatures and the slow diffusion kinetics, HEAs naturally possess the advantages to be considered as new types of high-temperature materials. If these unique advantages can be further combined with the high melting temperatures from refractory metals, the idea of refractory HEAs would be a highly interesting alloying concept within the context of high-temperature applications.

RHEAs, naturally, which are HEAs made from refractory metals (see Figure 2.2 below) and were first proposed in 2010 [15], [18], have indeed brought new hopes to push forward this stagnant field, promisingly leading to the development of novel ultrahigh-temperature engine materials.

Sc	Ti	V	Cr	Mn	Fe	Co	Ni	Cu	Zn
Y	Zr	Nb	Mo	Tc	Ru	Rh	Pd	Ag	Cd
*	Hf	Ta	W	Re	Os	Ir	Pt	Au	Hg
**	Rf	Db	Sg	Bh	Hs	Mt	Ds	Rg	Cn

Refractory metals
 Wider definition of refractory metals

Figure 2.2. Regular definition of refractory metals

The benefits of RHEAs: RHEAs have been paid substantial attention since their first report [15]. Indeed, the firstly developed two RHEAs in 2010, $\text{Mo}_{25}\text{Nb}_{25}\text{Ta}_{25}\text{W}_{25}$ and $\text{Mo}_{20}\text{Nb}_{20}\text{Ta}_{20}\text{V}_{20}\text{W}_{20}$ already significantly impressed the materials community in that their yield strength at temperatures above 800°C are much higher than that of some Ni-base commercial superalloys, Inconel 718 and Haynes 230. Today, research activities on RHEAs are among the most pursued ones in the HEAs community. Figure 2.3 summarizes the recent advances in the development of RHEAs, and it can be seen clearly that the compressive yield strength of most RHEAs exceeds that of Haynes 230 and some even show potential to extend the use temperature of turbine blades and disks beyond current superalloys.

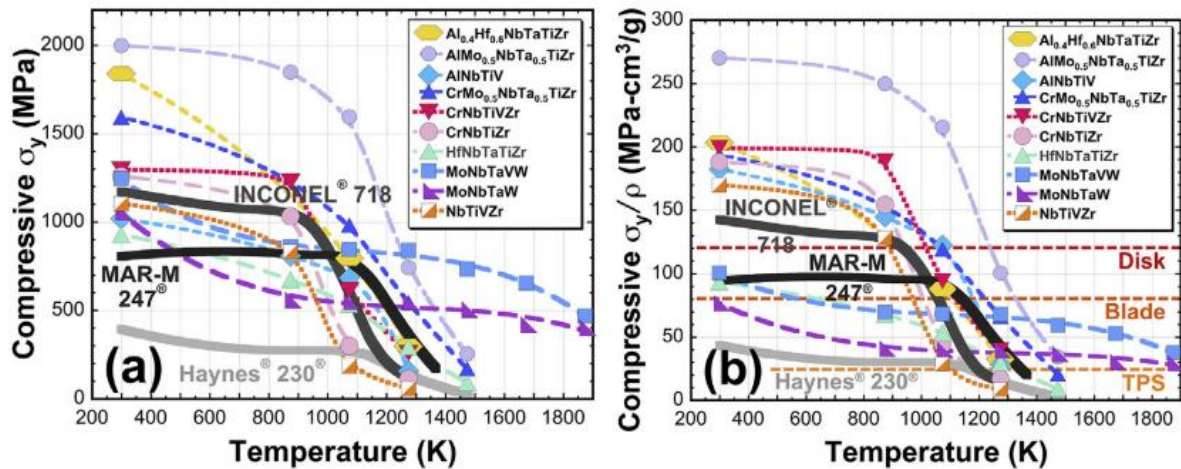


Figure 2.3. Temperature dependence of (a) compressive yield strength, σ_y and (b) σ_y normalized by alloy density, ρ , of some representative RHEAs. The performance for commercial superalloys (Haynes 230, Inconel 718 and MAR-M 247) are also shown for reference. Typical σ_y/ρ requirements for thermal protection sheet (TPS), turbine blades and disks are shown in (b). Reproduced from Ref. [19], with the permission of Elsevier.

It has been experimentally proved that a high yield strength of RHEAs at high temperatures over 1000°C is not difficult to get [20], [21], [22], [23]; due to the sluggish diffusion resulting from the severe lattice distortion, the diffusion related processes such as creep are expected to be slowed down in RHEAs which is also quite advantageous for the alloys aiming for use at elevated temperatures. Finally, RHEAs are composed of metals with metallic bonding, and supposedly they possess some degree of

ductility at different temperatures. Not surprisingly, since their discovery RHEAs have been believed to hold great potential to be the next-generation ultrahigh-temperature material.

The challenges of RHEAs: Initially, RHEAs suffer from issues like high density, brittleness, and oxidation. Density is not a big issue now, and brittleness is also solvable, but a combination of room temperature (RT) ductility, oxidation resistance and high temperature (HT) strength is quite challenging and has not been achieved yet. Even a combination of two out of the above-mentioned three aspects has proved extremely difficult. Previous efforts to address the brittleness (via VEC [24], [25] and TRIP [26], [27]) and insufficient oxidation resistance (by alloying and coating [28], [29], [30]), individually, are briefly summarized in the following sections. For structural materials used in the HT environment, they need to achieve a good balance of applicable density, RT ductility, HT strength and acceptable oxidation resistance. Unfortunately, for RHEAs, materials requirements for these various merits are often contradictory, similar to the scenario that is facing conventional refractory alloys [31], [32], [33]. Notably, one of the bottlenecks for utilizing RHEAs as structural materials has been their RT brittleness. As a matter of fact, the conflict between high strength and high ductility at RT is already a general problem for all metallic materials, not only for RHEAs. Basically, single-phase fcc structured HEAs are ductile but not strong enough; single-phased bcc structured HEAs, on the other hand, can be easily very strong but lack the ductility, particularly under tension, as exactly is the case for bcc structured RHEAs. How to solve the seemingly intrinsic conflict between strength (at RT and HT) and ductility (mainly at RT) for compositionally complex RHEAs therefore constitutes a great scientific challenge. Another challenge, and indeed a tougher challenge remains in that oxidation resistance is required for RHEAs, while keeping the balanced strength and ductility at the same time. In addition, how to efficiently design novel RHEAs with desirable properties is also quite a challenge. Trials and errors are certainly not efficient, if possible, considering the vast compositional space that is opened by the RHEA concept. Combinations with high throughput computational materials design can accelerate the discovery, exploration and development of RHEAs, based on thermodynamics calculations. Great challenges also mean great opportunities, considering the new advances that have been brought by RHEAs in recent years, and the compositional flexibility that is enabled by the RHEA alloy design strategy.

2.2 Conventional refractory alloys (CRAs)

CRAs are mainly composed of tungsten (W), molybdenum (Mo), tantalum (Ta), and niobium (Nb) which have long been noted for their high melting points (T_m) and their retentivity of strength at HT. CRAs have been extensively researched back to 50s, 60s, 70s of the last century and are widely used in HT areas such as aerospace, nuclear energy and heat-resistant applications. Figure 2.4 (a) shows ultimate tensile strength of refractory metals against temperatures up to 2000°C. The strength

decreases naturally with the increase of testing temperature. The common strengthening methods employed in the research and development of CRAs are solid solution hardening (SSH) and dispersion strengthening by secondary phases, including oxides, carbides and nitrides. Figure 2.4 (b) shows the yield stress of CRAs against temperatures up to 1200°C, benchmarked with state-of-the-art Ni-based superalloys. It can be easily seen that the strength of CRAs can hold up to higher temperatures and is affiliated with a lowered temperature-dependence as well. Noticeably, the HT strength of Nb-based WC3009 alloy has a comparable yield stress to Mo-based TZM alloy towards 1200°C, with the former having lower density and (much) higher ductility at RT.

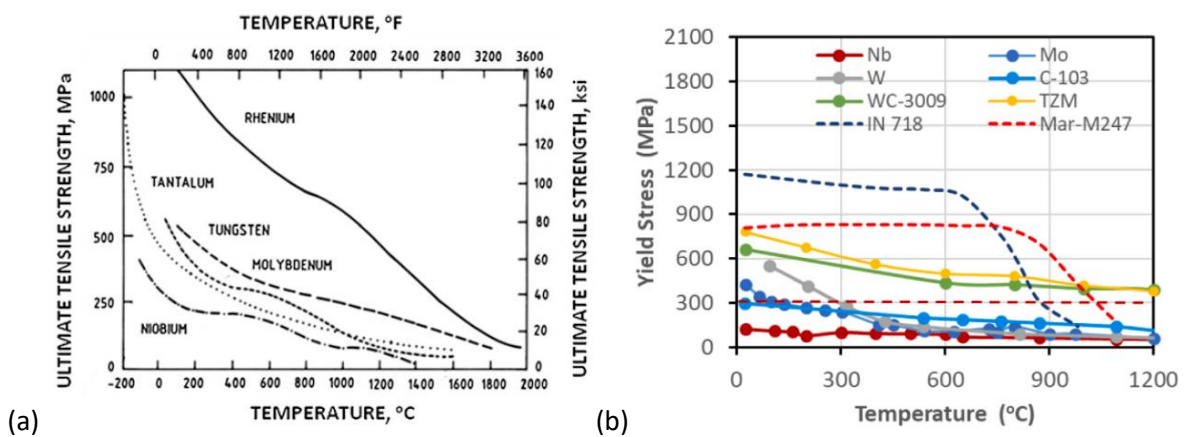


Figure 2.4. (a) Tensile strength of refractory metals versus test temperatures; (b) Temperature dependence of yield stress for CRAs, benchmarked with Ni-based superalloys. Reproduced from Ref. [34], [35], open access under Creative Commons CC-BY, and with the permission of Springer.

Among CRAs, Nb and Mo with their alloys are most developed due to their high melting points of 2468°C and 2617°C, comparable densities (to Ni-based superalloys) of 8.75 and 10.2 g/cm³, and low DBTT between -100°C to -195°C and 27°C, respectively. Mechanical properties of several commercial Nb and Mo alloys are shown in Figure 2.5. Mo-based alloys generally have an even higher strength than Nb-based alloys and can be used at even higher temperatures, but they are generally all brittle at RT.

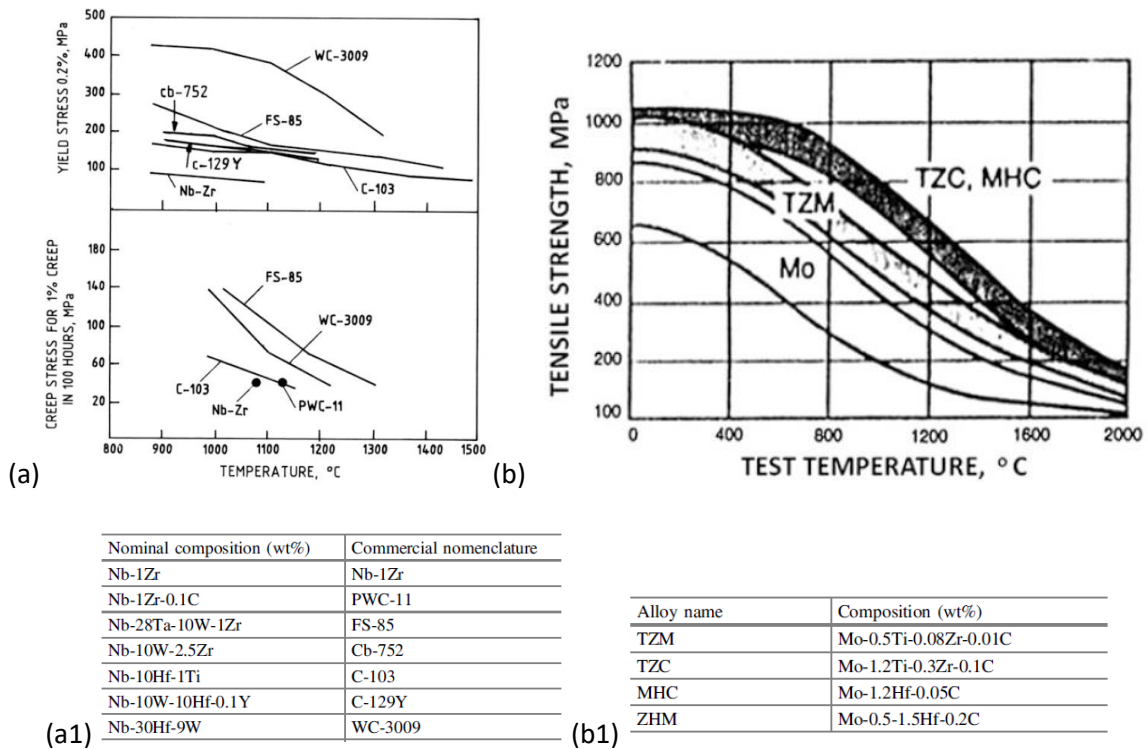


Figure 2.5. Elevated-temperature properties of some commercial (a) Nb-based alloys with nominal compositions given in (a1) and (b) Mo-based alloys with compositions given in (b1). Reproduced from Ref. [34], with the permission of Springer.

Recently, after the booming of RHEAs, intensive research on CRAs came back on the radar. Nb-based and Mo-based alloys are under the spotlight once again. Ductilizing Nb alloys with reduced density and cost were achieved by replacing Hf with Ti, Mo and W, and the resultant Nb-Mo-Ti, Nb-Mo-Zr and Nb-Ti-W systems can be used as a baseline for further development of high strength HT alloys when alloying with other elements [36], [37], [38]. For example, with 2 at. % addition of Fe into Nb-Mo-Ti alloys, the strength was noticeably increased in the temperature range of 25°C to 1200°C due to the solid solution strengthening effect, and the oxidation resistance of alloys at 1200°C in air was also improved compared to the base alloys [39]. Regarding Mo-based alloys, the strength resulted from the solid solution hardening by 11at. % addition of Hf went up to 420 MPa at 1400°C and 920 MPa at 25°C [40] (see figure 2.6 below); for Mo-based alloys strengthened by carbides dispersion, a simultaneous increase of strength and tensile ductility could be achieved with the yield strength of 483 MPa at 1200°C and 34.4 % elongation at RT [41] (see Table 2.1 below). Meanwhile, the mechanical properties of Mo-based alloys can be further modified by different thermomechanical treatments followed with heat treatments [42].

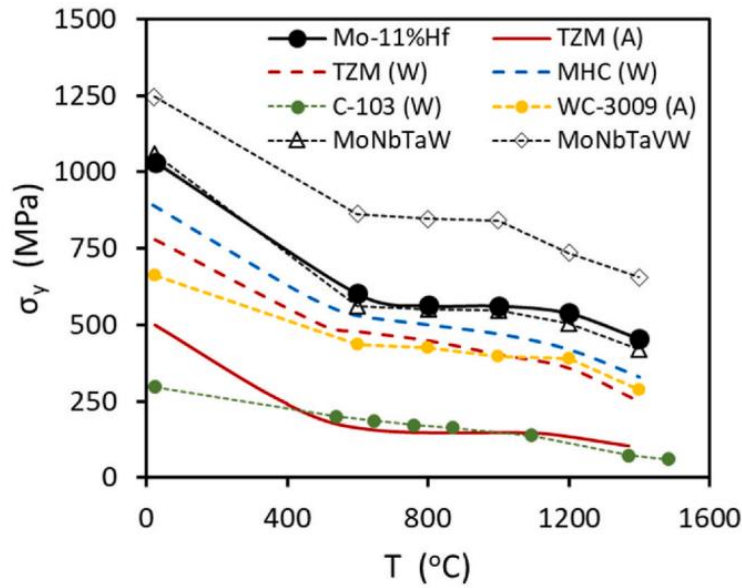


Figure 2.6 The temperature dependence of the yield stress of annealed Mo-11% Hf, commercial Mo alloys TZM and MNC in hot worked and stress relived conditions (W), TZM in hot worked and recrystallized condition (A) , Nb alloys C-103 in worked and stress relived condition (W) and WC-3009 in cast and annealed condition, and two refractory high entropy alloys, MoNbTaW and MoNbTaVW, showing outstanding high-temperature strengths in cast and annealed condition. Reproduced from Ref. [40], with the permission of Elsevier.

Table 2.1. Mechanical properties of various Mo alloys at different temperatures [41]

Materials	Tensile strength (MPa) / Total elongation (%)				
	Low temperature	Room temperature	1000 °C	1100 °C	1200 °C
Mo-ZrC	1334/14.5(-80 °C)	928 ± 11/34.4 ± 2.1	562/23.5	501/22.1	483/20.9
Pure-Mo	-	493 ± 25/33.8 ± 1.9	276/20.2	247/22.5	221/22.8
CP-Mo [29]	-	534/13	120/8.6	-	102/6.4
LCAC-Mo [36]	882/6.6(-50 °C)	653 ± 12/9.5 ± 1.3	260/3.1	-	-
TZM [36]	1041/8.1(-50 °C)	808±34/16.3 ± 3.1	524/3.6	-	414/7.0
ODS-Mo [36]	1072/9.0(-50 °C)	746±49/14.1 ± 6.5	330/5.3	-	-
ODS-Mo [29]	-	798/17.5	382/10.7	-	205/8.7
NS-Mo [29]	-	865 ± 5/37.5 ± 3.0	368/23.7	-	224/28.8
Mo-La ₂ O ₃ -ZrC [50]	-	988 ± 35/10.0 ± 0.7	578/8.2	-	420/9.4
La ₂ O ₃ -TZM [51]	-	1263/7.9	260/27.9	-	132/84.1
La-TZM [51]	-	1405/7.5	348/16.7	-	183/91.7

Although Nb-based and Mo-based CRAs show promising advantages as the next generation ultrahigh temperature materials, their poor oxidation resistance, similar to that of RHEAs, is restricting their further development and applications. The common sense of forming dense and protective oxide scales is to alloy with elements like Al, Cr and Si for HT (> 1000°C) service, which however shall be applied with caution to CRAs due to their causing embrittlement issues at RT and/or the strength losses at HT. Therefore, how to integrate oxidation resistance into the performance of CRAs without compromising their mechanical properties becomes a challenging research topic.

3 Roadmap

There is already a great body of literature reviews summarizing the alloy development and properties of refractory alloys. As stated previously, three aspects are most desired for refractory alloys, strength at HT (Target No.1), ductility at RT (Target No.2), and oxidation resistance (Target No.3). Ideally, refractory alloys shall possess a combination of all these three merits, which is however not achieved yet. Therefore, below the progress made on these three aspects is summarized separately.

3.1 Strength at high temperatures (Target No.1)

3.1.1 Solid solution hardening (SSH)

Solid solution hardening (SSH) caused by alloying, from both interstitial and substitutional additions, is accompanied by the development of HEAs and has been extensively employed for single-phase bcc-structured RHEAs and CRAs. As shown in Figure 3.1 below, hard but brittle MoNbTaW, MoNbTaVW and ductile HfNbTaTiZr are the most studied RHEA compositions, which all exhibit a single-phase bcc structure, and Mo, Nb, Ti, Zr are the most frequently used elements in RHEAs. Given the fact that almost all refractory metals possess the bcc structure or the bcc structure at high temperatures, all RHEAs have the bcc or ordered B2 structure, and in some cases several secondary phases such as Laves phase or B2 phase appear, as shown in Figure 3.2 below.

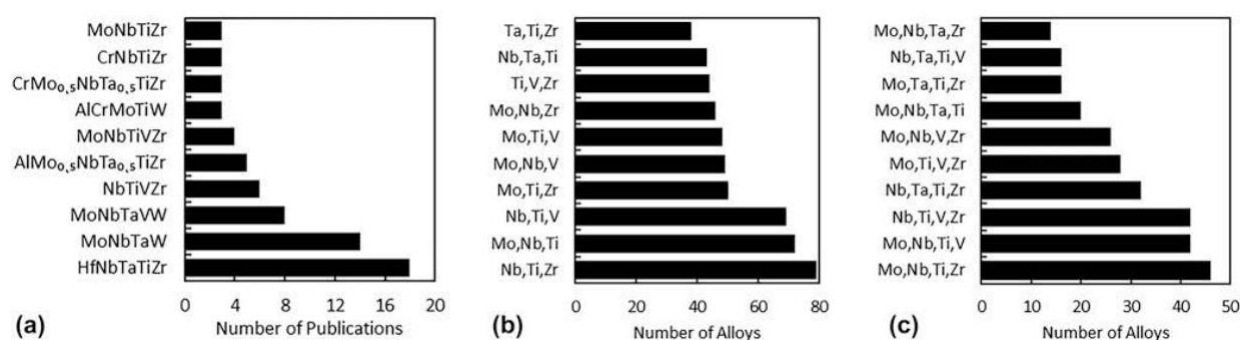


Figure 3.1. (a) Compositions of most frequently studied RHEAs and the number of publications where these compositions were studied (data published in 2018). (b and c) Most frequent combinations of (b) three elements and (c) four elements in reported RHEAs. Reproduced from Ref. [43], with the permission of Springer.

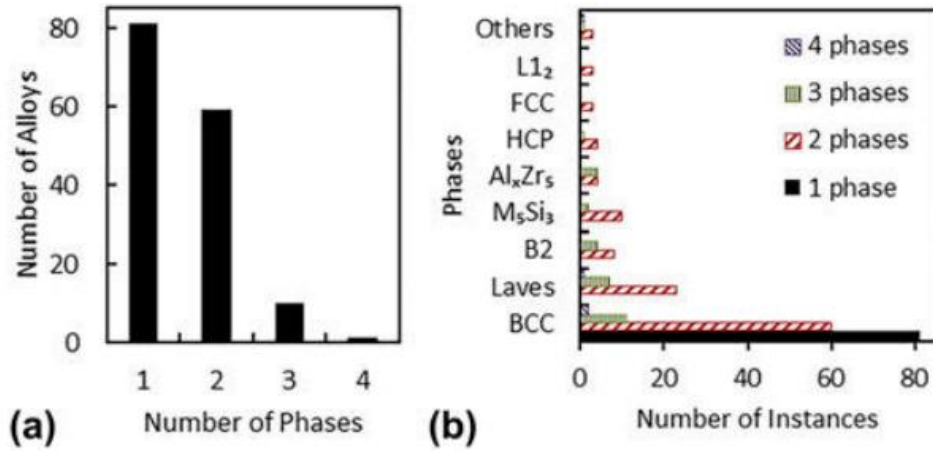


Figure 3.2. (a) Distribution of reported RHEAs by the number of phases. (b) Number of occurrences of different phases in 1-, 2-, 3-, and 4-phase RHEAs. Reproduced from Ref. [43], with the permission of Springer.

The yield strength at RT for some RHEAs is summarized in Figure 3.3, and it can be seen that single-phase RHEAs commonly have an atomic radius misfit parameter $\delta_r < 7.5\%$ (by definition, $\delta_r = 100\% \sqrt{\sum c_i \left(1 - \frac{r_i}{\bar{r}}\right)^2}$, where c_i and r_i are the mole fraction and atomic radius of an alloying element i , respectively, and $\bar{r} = \sum c_i r_i$), and there is no direct correlation between $\sigma_{0.2}^{25^\circ C}$ and δ_r for these alloys. For most cases at RT, the yield strength from multi-phase alloys is higher than that from single-phase ones, which totally makes sense due to the secondary phase strengthening effect.

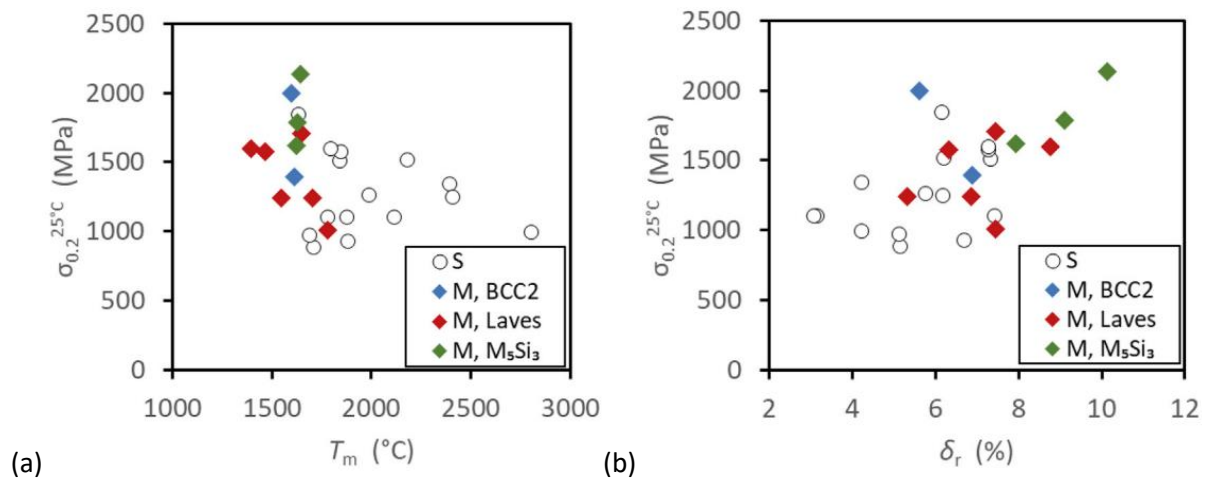


Figure 3.3. Room temperature yield strength ($\sigma_{0.2}^{25^\circ C}$) of single-phase (S) and multi-phase (M) RHEAs as a function of (a) the alloy melting temperature T_m , (b) the atomic radius misfit parameter δ_r . Reproduced from Ref. [44], with the permission of Elsevier.

Regarding the yield strength of RHEAs at HT, as shown in Figure 3.4, there is a clear trend observed in that the single-phase alloys with a higher melting point have a higher yield strength at $1000^\circ C$. Furthermore, $\sigma_{0.2}^{1000^\circ C} / \sigma_{0.2}^{25^\circ C}$ is proportional to the melting points of these single-phase bcc

structured alloys that are listed here. As for the alloys with multi-phases, their HT strengths are randomly distributed and tend to degrade over 1000°C possibly due to the dissolving of strengthening phases at HT [44].

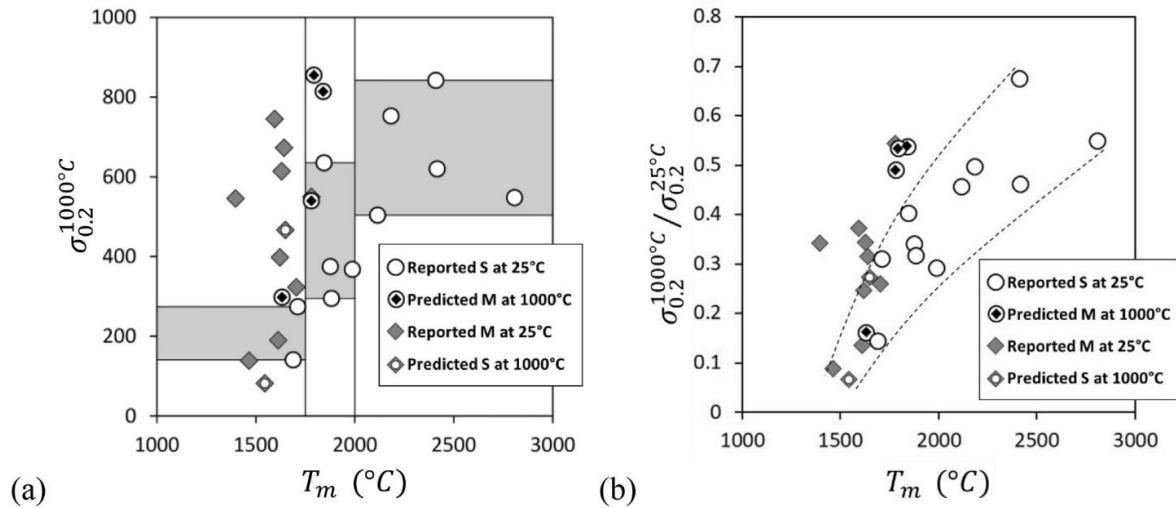


Figure 3.4. (a) Yield strength at 1000°C ($\sigma_{0.2}^{1000^{\circ}\text{C}}$) and (b) yield strength ratio ($\sigma_{0.2}^{1000^{\circ}\text{C}} / \sigma_{0.2}^{25^{\circ}\text{C}}$) of single-phase (S) and multi-phase (M) RHEAs as a function of the melting temperature T_m . Reproduced from Ref. [44], with the permission of Elsevier.

SSH is also commonly used in single-phase bcc-structured CRAs. Investigations on binary refractory alloy systems have shown a positive dependence of strength on the atomic size and valence difference between the solvent and solute elements. Alloying elements should comply with one of the following criteria: 1) presence of a wide solubility range even at high temperatures; 2) an increase of intra-atomic bonds that is sufficiently reflected in increased melting points of the alloy; 3) a great difference of atomic sizes as compared to solvent element which relates to the considerable elastic distortions in the crystal lattice impeding the movement of dislocations; 4) the workability of the alloys should not be radically decreased; 5) alloys should not become considerably heavier and more expensive [45].

In light of the literature reviewed, as high yield strength at HT is desired, single-phase refractory alloys are preferable choices over alloys with multi-phases. As for the solid solution strengthening in bcc-structured metallic materials, it is widely accepted that plasticity is mainly controlled by the motions of screw dislocations [46], [47]. Recently, however, several findings discovered that at intermediate or higher temperatures the movement of edge dislocations plays a non-negligible role [48], [49]. Conventionally, the deformation behavior of bcc material is far more complex than that of fcc materials. The flow stress, which is temperature and strain rate dependent, can simply be divided into three stages as a function of temperature: at the low temperature range (< 0.25 homologous temperature), the flow stress is strongly temperature and strain rate dependent. The motion of the

non-planar core of $1/2\langle 111 \rangle$ screw dislocation is thermally activated by double-kink nucleation and can then propagate laterally along the long screw dislocation line when an external shear stress is applied [50]; at the intermediate temperature range (≤ 0.5 homologous temperature), the flow stress is insensitive to the temperature or strain rate. Plasticity is mediated by either the motion of screw, edge dislocations or mixed dislocations passing by the rough landscape resulted from the lattice distortion; at the high temperature range (> 0.6 homologous temperature), the flow stress drops quickly due to the increasing impact of thermally activated diffusional processes and is mainly controlled by dislocations climbing. However, in case of concentrated solid solutions, some additional effects have to be taken into consideration, like the pinning mechanism due to fluctuations of local chemical environment, or the formation of super-jogs, as well as the transition from screw- to edge-dislocation dominated yielding [50], [51], [52], [53].

The solid solution strengthening results from the interaction of elastic stress field between the dislocations and solute atoms [54], [55]. The interaction force, F , increases with both the atomic size misfit parameter, $\delta_a = (1/a) da/dc$, and the modulus misfit parameter, $\delta_\mu = (1/\mu) d\mu/dc$, of the solute and solvent elements [43]:

$$F = \mu b^2 \delta = \mu b^2 (\delta_\mu + \beta \delta_a)$$

Here μ is the shear modulus of the alloy, b is the magnitude of the Burgers vector, a is the lattice parameter, c is the solute atom fraction, and β is a constant, which is in the range from 2 to 4 for screw dislocations and ≥ 16 for edge dislocations [54]. For a concentrated solid solution, the solute-induced stress increase $\Delta\sigma$ can be expressed as [54], [56]:

$$\Delta\sigma = A \mu \delta^{4/3} c^{2/3}$$

Here A is a dimensionless constant which is of order of 0.1. This equation was initially developed by Labusch [56] for binary solid solutions in which the concentration of the solvent exceeds 60–70% and modified by Senkov et al. [57] later to apply as the first solid solution strengthening model for RHEAs and tried on the HfNbTaTiZr alloy. The misfit parameters δ_a and δ_μ were calculated by averaging nearest-neighbor atom interactions under the assumptions that local concentrations are equal to the average concentration of the alloy. Then, the modified parameters of δ_{ai} and $\delta_{\mu i}$ in the vicinity of an element i can be calculated as [57]:

$$\delta_{ai} = \frac{9}{8} \sum_j c_j \delta_{aj}$$

$$\delta_{\mu i} = \frac{9}{8} \sum_j c_j \delta_{\mu ij}$$

Here c_j is the atomic fraction of an element j in the alloy, 9 is the number of atoms in the i -centered polyhedron in the bcc lattice, 8 is the number of atoms neighboring with the center atom i , $\delta_{aij}=2(r_i-r_j)/(r_i+r_j)$, and $\delta_{uij}=2(u_i-u_j)/(u_i+u_j)$ [43].

Based on the equations listed above, a direct correlation between the yield stress increase and atomic size plus modulus misfit parameters can be established, but still, it falls into the single-phase bcc structured alloys category. One potential issue with solid solution strengthening is this large misfit between either atomic or modulus will increase the risk of decomposition of phase and lower the thermal stability of the alloy in particular at HT. An example of superior high strength of RHEAs at 1000°C designed using this strategy to maximize the misfit parameters is given in Figure 3.6. It was noted that a higher yield strength from the same CrMoNbV alloy could be achieved, when being prepared by powder metallurgy, over the traditional cast counterpart. Therefore, different material fabrication methods are worthwhile exploring, like additively manufacturing for instance. Despite high yield stress is always a priority, a good balance of ductility at RT and yield stress at HT is the ultimate goal.

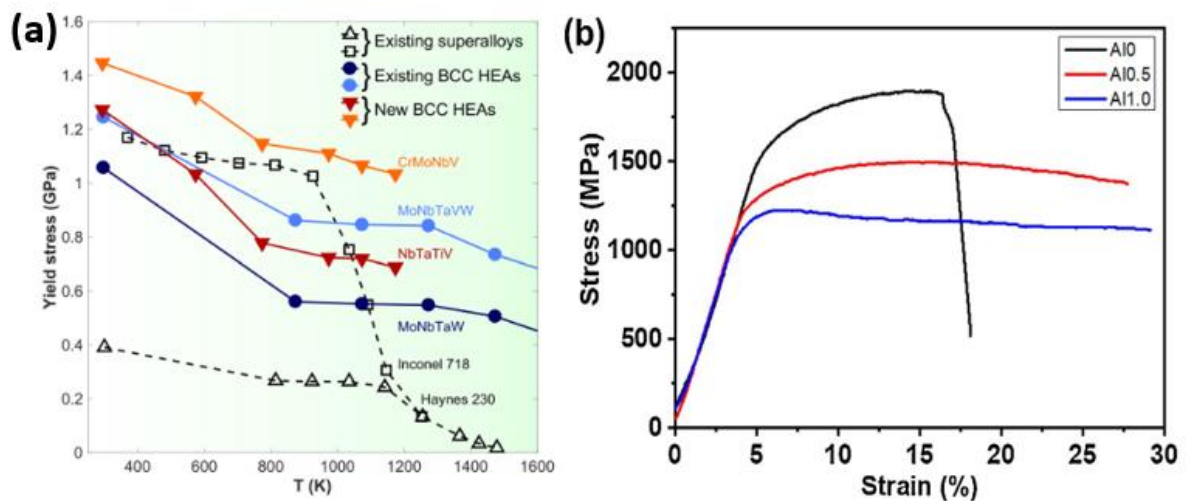


Figure 3.6. (a) The compressive yield stress vs temperature of several high-strength RHEAs, including CrMoNbV which shows the highest yield stress over a wide temperature range. Reproduced from Ref. [48], Open Access (Nature Communications); (b) compressive engineering stress and strain curves of Al_xCrMoNbV alloys fabricated by the powder metallurgy route. Reproduced from Ref. [23], with the permission of Elsevier Science & Technology Journals.

Another aspect in terms of strengthening is the short-range-ordering (SRO), on atomic pairs mainly associated with the large negative enthalpies, such as Ti group metals associated with interstitial elements like oxygen [58], [59], [60]. SRO, which is system-dependent, can make a difference not only to the strength but also the deformation behaviors. Therefore, it can be an effective way to overcome the commonly seen trade-off between strength and ductility. How to engineer an SRO configuration

with various degrees is challenging. Nevertheless, the concept of HEAs significantly expands the alloy compositions and naturally HEAs become a hotbed for nurturing SROs. These atomic pairings can act as pinning points to affect the dislocation behaviors [61], [62] and alter stacking fault energy [63], therefore can eventually result in different material performance.

3.1.2 Secondary phase strengthening

bcc/B2 strengthening in RHEAs: From previous reports on multi-phases RHEAs with different secondary phases such as B2, Laves phase and silicide [64], [65], [66], one combination simulating the typical γ/γ' microstructure in Ni-based superalloys, i.e., the bcc/B2 structural configuration with coherent precipitates sticks out and is showing some promise [67], [68], [69], [70], [71]. From the very beginning [72], Al was introduced to lower the density, increase HT strength and specific strength, and improve oxidation resistance simultaneously. Another purpose is to see if the Al addition can stimulate or suppress the formation of intermetallic phases in the Ti-Zr-V-Nb-Ta-Mo system. Three example compositions, $\text{AlMo}_{0.5}\text{NbTa}_{0.5}\text{TiZr}$, $\text{Al}_{0.3}\text{NbTaTi}_{1.4}\text{Zr}_{1.3}$ and $\text{Al}_{0.5}\text{NbTa}_{0.8}\text{Ti}_{1.5}\text{V}_{0.2}\text{Zr}$ with low density all showed basket-weave-like, coherent nanolamellar structures inside the grains. The bcc structure and the ordered B2 structure were confirmed by TEM (Figure 3.7 b). $\text{AlMo}_{0.5}\text{NbTa}_{0.5}\text{TiZr}$, had the highest yield strength of 745 MPa at 1000°C among the three tested alloys making it very competitive, and it got substantial attention since its discovery.

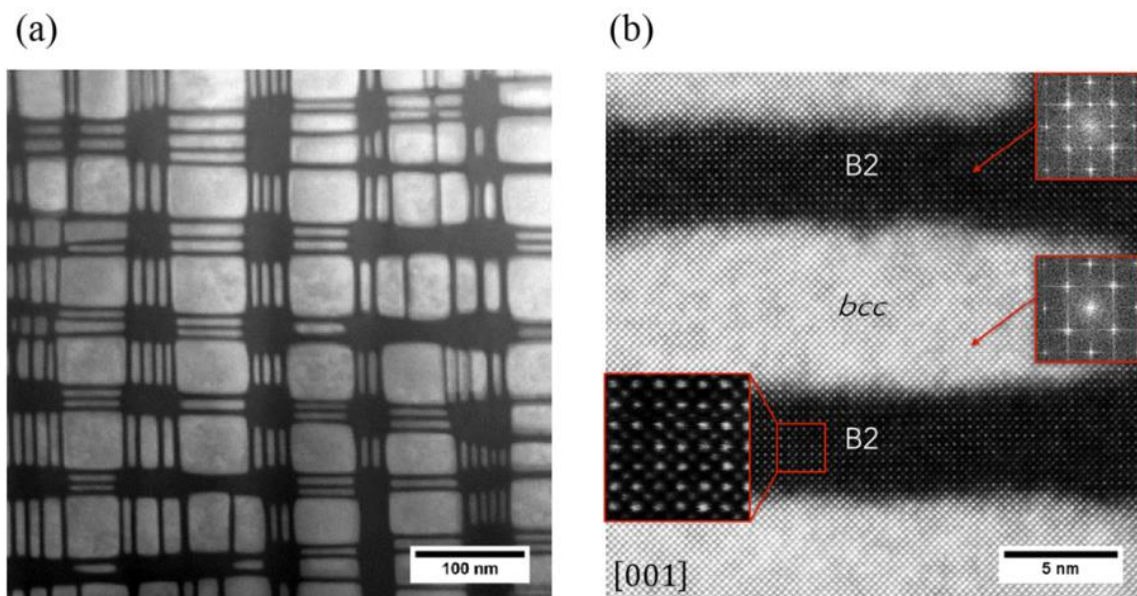


Figure 3.7. STEM-HAADF images of nanostructure present inside the grains of $\text{AlMo}_{0.5}\text{NbTa}_{0.5}\text{TiZr}$. (a) Cuboidal precipitate of disordered bcc phase and continuous ordered B2 phase. (b) Fast Fourier transforms reveal an ordered B2 and disordered bcc phase. Reproduced from Ref. [73], with the permission of Springer.

Afterwards, tremendous efforts have been put along this line of research, hoping that this is maybe a potential way to solve the brittleness issue extensively existing in the single-phase bcc structured

RHEAs at RT and to retain their high strength at HT at the same time [70]. Again, the popular composition $\text{AlMo}_{0.5}\text{NbTa}_{0.5}\text{TiZr}$ was systematically characterized [68]. The phases were found to exhibit a continuous channeled B2 phase enriched with Al and Zr plus a coherent precipitates of discontinuous bcc phase enriched mainly with Nb, Ta (Figure 3.8) and an orientation relationship was given by $\langle 100 \rangle_{\text{bcc}} // \langle 100 \rangle_{\text{B2}}, \{001\}_{\text{bcc}} // \{001\}_{\text{B2}}$.

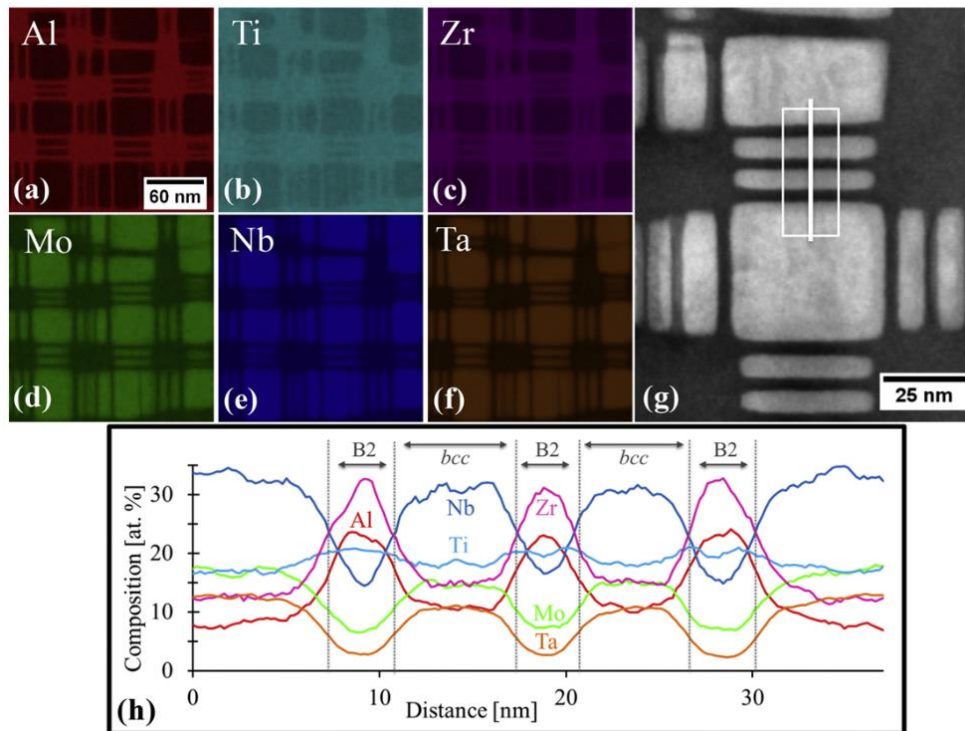


Figure 3.8. (a-f) XEDS elements maps of the $\text{AlMo}_{0.5}\text{NbTa}_{0.5}\text{TiZr}$ alloy. (g) A STEM-HAADF image with a white line identifying the location of the quantified XEDS line-scan shown in (h). Reproduced from Ref. [68], with the permission of Elsevier Science & Technology Journals.

Although the microstructure is analogous to Ni-based γ/γ' superalloys and the specific strength is exceptionally high in the whole temperature range, the alloy is still quite brittle especially at RT. It is noted here that the matrix is the brittle B2 channel and the ductile bcc phase acts as precipitates, which is exactly the opposite component configuration of traditional Ni-based superalloys with a ductile fcc matrix and $\text{L}_{12}\text{Ni}_3\text{Al}$ as the precipitate. Thus, efforts were made on microstructural design to improve the ductility of the initially brittle RHEA. As an example, the microstructure of $\text{Al}_{0.5}\text{NbTa}_{0.8}\text{Ti}_{1.5}\text{V}_{0.2}\text{Zr}$ was successfully adjusted by using different heat treatments [69]. Under the as-cast condition (1) the alloy originally showed a basket weave-like continuous B2 as the matrix with discrete bcc phase as precipitates; after quenching from 1400°C followed by 20 minutes of homogenizing treatment, the alloy showed a bcc matrix with nano-scaled B2 precipitates, referred as condition (2); the alloy in condition (2) was further annealed at 600°C for 120 hours and water-quenched to produce a continuous bcc matrix with discrete B2 precipitates around 50 nm in size

(condition (3)). Across all three conditions, the chemical composition of the bcc phase is enriched with Nb and Ta and the B2 phase is enriched with Zr and Al (Figure 3.9).

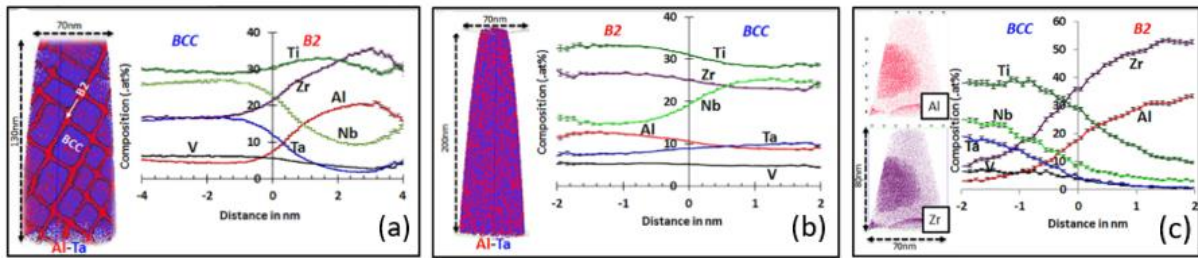


Figure 3.9. APT re-construction of Al-(red) and Ta-(blue) rich regions (left) and compositional changes across a bcc-B2 interface (right) of $\text{Al}_{0.5}\text{NbTa}_{0.8}\text{Ti}_{1.5}\text{V}_{0.2}\text{Zr}$ under condition (1) (a); condition (2) (b); condition (3) (c).

Reproduced from Ref. [69], Open Access (Scientific Reports).

Accordingly, the mechanical properties were changed because of this microstructural reversion. The alloy under condition (1) showed a clear high strength at 25°C and 600°C; condition (2) provided the highest compressive strain; while condition (3) gave a good combination of strength and compressive strain (Figure 3.10). This attempt validated again that the superalloy-like RHEAs are supposed to equip a structure with soft bcc phase as the matrix and hard B2 phase as coherent precipitates.

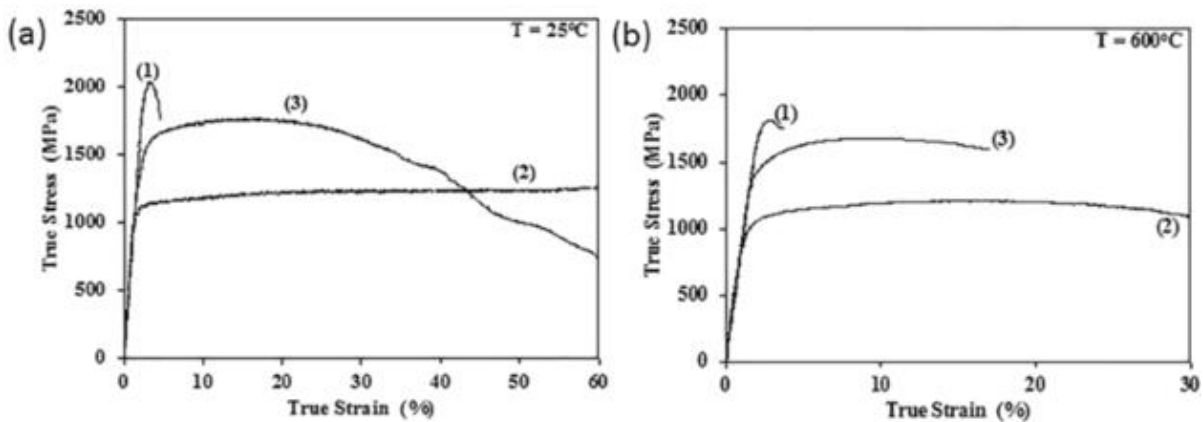


Figure 3.10. Compressive true strain-stress curves of $\text{Al}_{0.5}\text{NbTa}_{0.8}\text{Ti}_{1.5}\text{V}_{0.2}\text{Zr}$ under different conditions (1) cast plus HIP followed by annealing at 1200 °C for 24 h and slow cooling; (2) Condition (1) plus additional annealing at 1400 °C for 20 min and water quenching; (3) Condition (2) plus additional annealing at 600 °C for 120 hrs and water quenching. The testing temperatures are (a) $T = 25\text{ °C}$, (b) $T = 600\text{ °C}$. Reproduced from Ref. [69],

Open Access (Scientific Reports).

Since the matrix and precipitates can be easily reversed by using heat treatments, two points are worth thinking about when considering putting bcc/B2 refractory high entropy alloys into potential high temperature applications: phase inversion transformation [74], [75] and thermal stability of phases [76], [77].

Consequently, again the $\text{Al}_{0.5}\text{NbTa}_{0.8}\text{Ti}_{1.5}\text{V}_{0.2}\text{Zr}$ alloy was used for isothermal heat treatments over different time spans [74]. The alloy was first homogenized at 1200°C for 2 hours followed by water quenched and then annealed at 600°C for 0.5, 5, 12, 24, 120 h. Figure 3.11 shows the distribution of Al ions as a traceable element for the transformation of ordered B2 phase during this process. It can be clearly seen that from the start Al is mainly enriched along the B2 channels and then it gradually grows and gets widened after 5h of exposure. Meanwhile, the bulge starts to form at the intersections of the B2 channel which is visible in Figure 3.11 (c). These bulges grow and lead to thinning at the centers as can be observed after 24h in Figure 3.11 (e) with thinned channels connecting them together. After annealing for 120h, the structure is coarse and only portions of B2 (Al) and bcc (Nb) regions are shown in Figure 3.11 (f). This inversion of bcc and B2 phases stems from the spinodal decomposition mechanism which can be achieved by different heat treatments. There is a strong miscibility gap presented between Ta and Zr, and between Nb and Zr seen from their binary phase diagrams [78], [79]. At high temperatures the bcc phase spinodally decomposes into two bcc phases with different compositional partitions with Nb (Ta) and Zr, and the Zr enriched bcc phase subsequently undergoes chemical ordering transforming into the B2 phase with Al addition due to their big electronegativity difference [74].

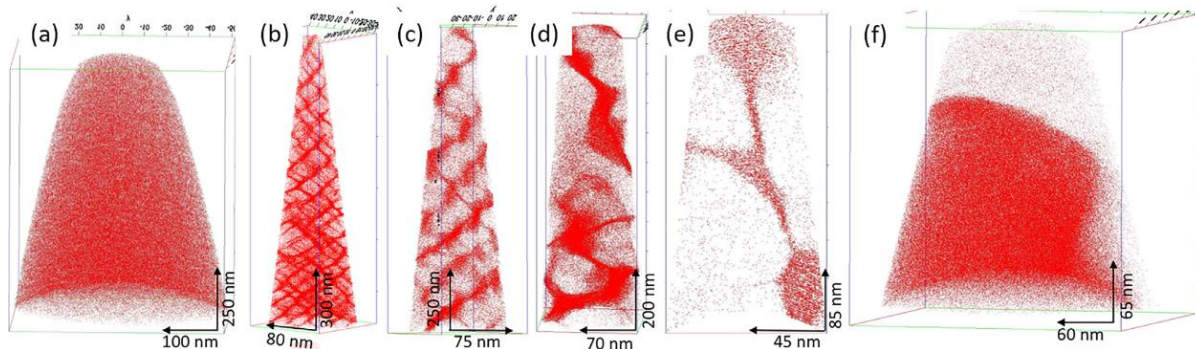


Figure 3.11. APT Al ion maps from the isothermal annealed samples of $\text{Al}_{0.5}\text{NbTa}_{0.8}\text{Ti}_{1.5}\text{V}_{0.2}\text{Zr}$ at $600^\circ\text{C}/x$ h. $x=(a)$ 0, (b) 0.5, (c) 5, (d) 12, (e) 24 and (f) 120. Reproduced from Ref. [74], with the permission of Elsevier.

Next concern is the thermal stability, which is equally important to microstructural arrangement since the alloys are expected to retain their mechanical properties throughout their lifetime. Homogenized alloys of $\text{AlNbTa}_{0.5}\text{TiZr}_{0.5}$ and $\text{AlMo}_{0.5}\text{NbTa}_{0.5}\text{TiZr}_{0.5}$, both derived from the AlMoNbTaTiZr system, were chosen to put under 1200°C , 1000°C , and 800°C for 1000h [76]. Results have showed that $\text{AlNbTa}_{0.5}\text{TiZr}_{0.5}$ exposed at 1200°C , 1000°C and 800°C resulted in further intragranular precipitate of the hexagonal Al-Zr intermetallic compound, the formation of an Al-Nb rich orthorhombic phase and hexagonal Al-Nb-Ti phase in different levels; while the $\text{AlMo}_{0.5}\text{NbTa}_{0.5}\text{TiZr}_{0.5}$ alloy resulted in Al-Zr rich hexagonal intermetallic phase when being exposed at 1200°C and 1000°C , and a desirable fine scale B2-bcc microstructure at 800°C (Figure 3.12). Comparing these two alloys, a clear beneficial impact

from the addition of Mo on the microstructural stability is found below 1000°C, after a long duration of annealing. However, the intragranular precipitation of Al-Zr intermetallic phase remains a great concern as it is likely to be detrimental to alloy properties [76]. Furthermore, the recent work on the effect of Al on the formation and stability of bcc-B2 microstructure from Ti-Ta-Zr-Al_x system was carried out by Whitfield et al. [77] which again is based on the thinking that Al is fundamentally important to the ordering of Zr-rich bcc phase to B2 phase at high temperatures. The results further extended and reinforced the previous findings in that an Al content > 5 at% in bulk is needed for the ordering of Zr-rich bcc phase into B2 phase, which happens after the spinodal decomposition; the B2 phase is only stable to relatively moderate temperatures lower than 900°C; and the deleterious intragranular Al-Zr-rich intermetallics were observed following long duration of thermal exposures [77].

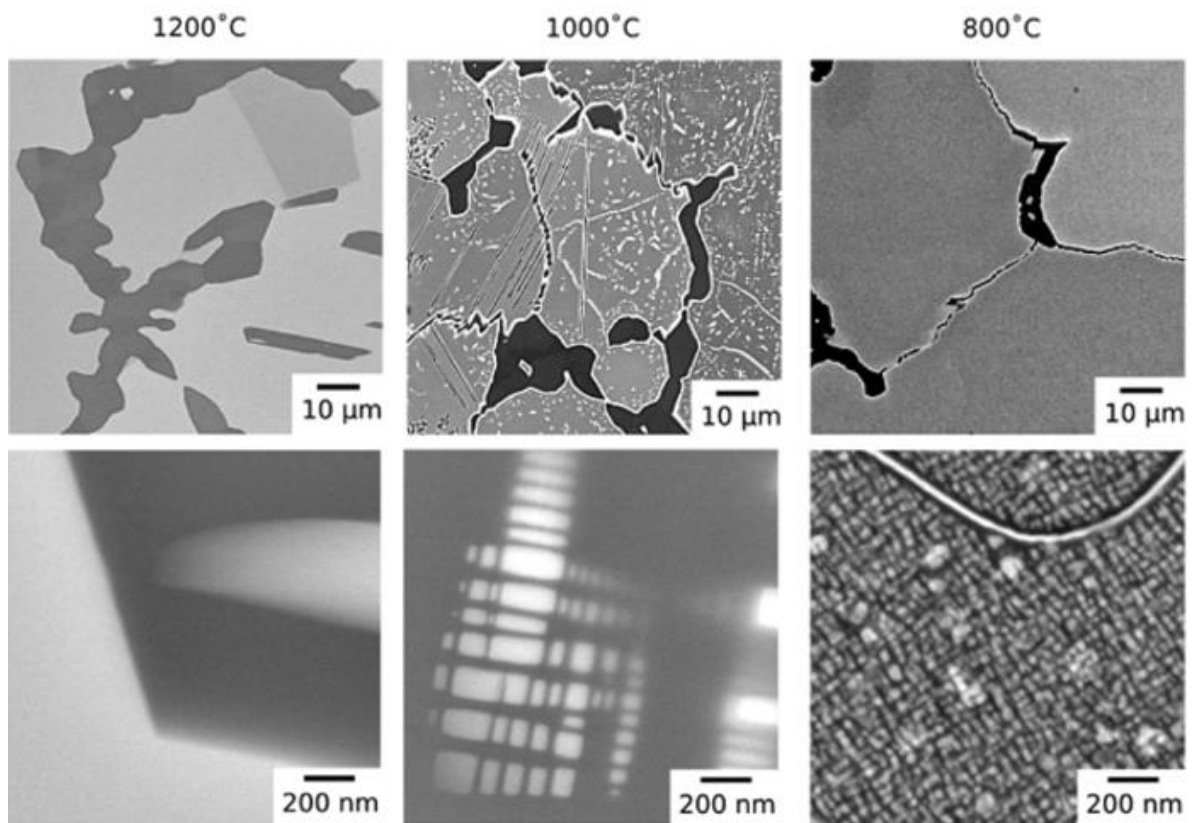


Figure 3.12. BSE images of AlMo_{0.5}NbTa_{0.5}TiZr_{0.5} following 1000h of thermal exposure at 1200°C, 1000°C and 800°C. The magnification of the images increases from top to bottom. Reproduced from Ref. [76], with the permission of Elsevier Science & Technology Journals.

This phases inversion reflects the thermal instability at high temperatures, which is one fatal negative side of this alloy design concept based on spinodal decomposition. Another negative side is about the lattice misfit between these two phases. Lattice misfit parameter is calculated by $\varepsilon = 2 \frac{a_{b2} - a_{bcc}}{a_{b2} + a_{bcc}}$, ~0.1% for spherical precipitation and ~0.5% for cuboidal precipitation are needed to lower the coarsening

rate [80]. Misfit of 0.6% was reported for the $\text{Al}_{0.5}\text{NbTa}_{0.8}\text{Ti}_{1.5}\text{V}_{0.2}\text{Zr}$ alloy in the homogenized condition [72], which is already larger than normal Ni-based superalloys presenting the rafting or coarsening of the γ' precipitate [81], [82]. A misfit parameter of 0.3% between γ -matrix and γ' -precipitates for example will expect a lattice misfit stress of 375.9 MPa within the interfaces [83]. The same goes for the modulus misfit between two phases. Commonly an elastically softer phase forms the network and wraps the harder particles. As is well accepted, the coarsening of microstructures strongly depends on the interplay between the interfacial and elastic energies [74]. A minimization of the elastic strain energy requires that the elastically hard phase deforms less than the soft one. Thus, the elastic energy is less for discrete hard precipitates in a continuous soft matrix than for discrete soft precipitates in a continuous hard matrix [74]. Last but not least, heterointerfaces with complete compositional difference and large misfit will also easily act as the oxygen absorption and transportation path which will further compromise the comprehensive properties of alloys. Exploration and development of stable and coherent precipitates with low misfit for refractory high entropy alloys at temperatures higher than what conventional Ni-based superalloys achieve, is a rather important and promising scientific topic.

Secondary phase strengthening in CRAs: Oxides, nitrides and carbides are commonly used to contribute to strengthening in the Re-Me_{IV}-X (Re=Nb, Mo; Me=Ti, Zr, Hf; X=O, N, C) systems, and simultaneously to modify ductility of alloys depending on their size and dispersion degree. Meanwhile, different ways for synthesizing and processing alloys, such as melting with oxygen contamination, casting followed by thermomechanical treatments, and powder metallurgy could also result in different mechanical properties [84], [45], [85]. Again, they verify the prime importance of the dispersion degree of these dispersoids. The strengthening phase should meet the following requirements: 1) higher mechanical strength as compared with that of the matrix; 2) particles must be of sufficient size to be non-shearable to dislocation motion; 3) sufficient volume percentage; 4) stability of particles size at operating temperatures [45].

Take Mo-based alloys as an example, like the commercial TZM (Mo-0.5Ti-0.08Zr-0.01C, in wt%) and TZC (Mo-1.2Ti-0.32Zr-0.1C, in wt%) alloys. Strength increased with the increasing number of carbides and stabilized gradually. Hf contained carbide has a more profound effect on the strength than that of carbides with Zr and Ti, see from Figure 3.13 below. It is noted that strength at 1315°C for Mo-based alloys with carbide dispersion can go beyond 400 MPa (for reference: 10 KSI = 69 MPa), which shows their promising applications at ultrahigh-temperature environments like in aerospace.

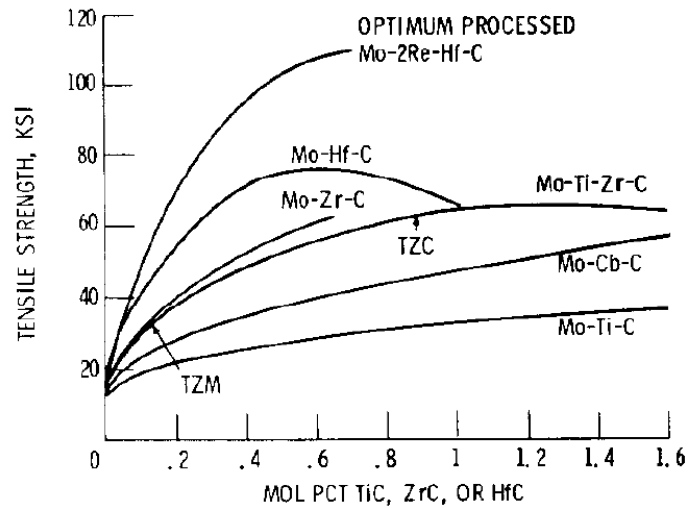


Figure 3.13. Tensile strength of swaged, carbide-strengthened molybdenum alloys at 1315°C. Reproduced from Ref.[86], with the permission of Elsevier.

3.2 Ductility at room temperature (Target No.2)

Due to the high cost of raw metals and related processing procedures, refractory alloys should primarily be considered for application areas with stringent performance demands like aerospace or nuclear reactors for example. Although a high yield strength at HT is always a priority for these alloys, a non-zero tensile ductility at RT is also a prerequisite for materials to be conveniently processed. Three ductility criteria for single-phase bcc structured RHEAs (Figure 3.13) are summarized here [87]: the *Pettifor and Pugh criterion* [88], [89] predicts that materials with non-directional metallic bonds are intrinsically ductile, with a positive Cauchy pressure $C_{12}-C_{44}>0$ and $G/B<0.42$ (G is shear modulus, and B is bulk modulus) [90], [91]; the *valence electron concentration (VEC) criterion* proposed by Sheikh et al.[92] predicts that RHEAs made from elements of transition groups 4, 5 and 6 are ductile with a VEC value lower than 4.5; this was suggested to revise by Senkov et al. [87] who recently proposed that the ductile-to-brittle transition instead covers a range of VEC values (not a clearly defined threshold VEC value) and RHEAs with a tensile σ_y of ≤ 1200 MPa and compressive σ_y of ≤ 1500 MPa could be ductile. In addition, there exists the *Rice and Thomson criterion* [93] which predicts that crystals whose dislocations have wide cores and small values of the parameter Gb/γ ($<7.5-10$) are ductile. Currently, there exist quite a few RHEAs with tensile ductility at RT, but the problem is that those alloys with decent yield stress at HT rarely have any tensile elongation at RT; at most they exhibit some plasticity under compression. The defect tolerance capacity of alloys under compression is much higher than that under tension, rendering the compression test less defect sensitive. However, the material is very sensitive to defects in reality, which will cause premature failure resulting in catastrophic outcomes. Requiring non-zero tensile elongation for RHEAs will benefit their future

applications. Below, several potential means to cope with this ductility issue, which the RHEAs are facing now, are described.

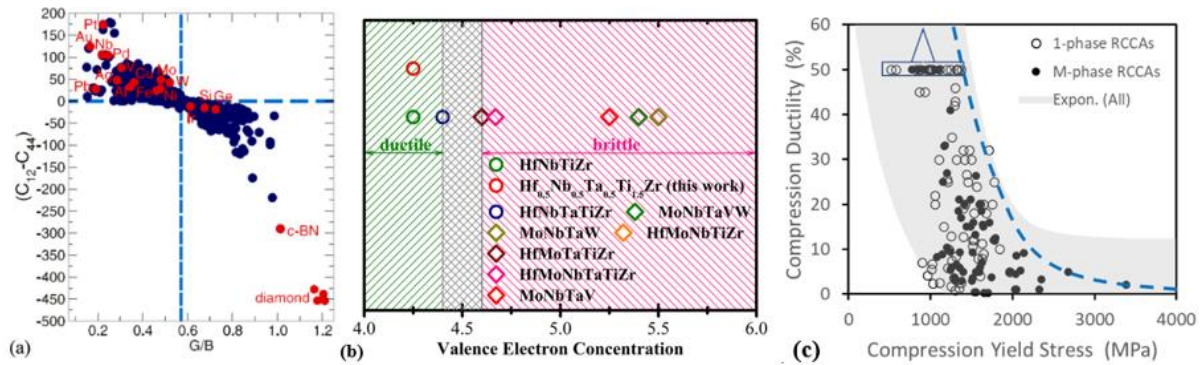


Figure 3.13. Ductility criteria for single-phase bcc structured RHEAs. (a) Correlation between $(C_{12}-C_{44})$ and G/B .

The top left corner with $(C_{12}-C_{44}) > 0$ and $G/B < 0.42$ are ductile. Reproduced from Ref. [69], Open Access (Scientific Reports); (b) alloys with VEC lower than 4.5 are ductile. Reproduced from Ref. [24] with the permission of American Institute of Physics; (c) alloys with compressive yield stress lower than 1500 MPa are ductile. Reproduced from Ref. [87], with the permission of Elsevier Science & Technology Journals.

3.2.1 Valence electron concentration (VEC) engineering

According to the Hume-Rothery rule for solid solution formation, electron concentration is decisive to form different crystal structures [94]. There are basically two definitions of electron concentration: average number of itinerant electrons per atom, e/a , and the number of total electrons including the d -electrons accommodated in the valence band, known as valence electron concentration or VEC [95], [96]. VEC for a multi-component alloy can be defined as the weighted average from VEC of the constituent components: $\sum_{i=1}^n C_i(VEC)_i$. C_i is mole fraction and VEC_i is the VEC for the individual element. Based on the observations from Ref.[25], the fcc phase is found to be stable at higher VEC (≥ 8) and the bcc phase is stable at lower VEC (≤ 6.87) instead. Further, from 9 RHEAs made from groups 4, 5, 6, Sheikh et al. found that ductile alloys have a $VEC \leq 4.4$ and they designed one alloy composition Hf_{0.5}Nb_{0.5}Ta_{0.5}Ti_{1.5}Zr to successfully prove the concept with a fracture stress of close to 1 GPa and an elongation of near 20% [92]. This is generally one effective way to design ductile RHEAs within groups 4, 5 and 6 [97]. Senkov et al.[87] recently gathered more alloy compositions with different processing conditions, and they stated that tensile ductility can vary from marginally ductile (1.7%, after severe plastic deformation + annealing) to ductile (20%, after cold rolling + annealing) for the same alloy, HfNbTaTiZr ($VEC = 4.4$). Furthermore, alloys such as MoNbTi ($VEC = 5.0$) and NbTaTi ($VEC = 4.67$) are reported to have tensile elongations of 4% and 18.5% (Figure 3.13), even though their VEC is larger than 4.5. Elements with the same VEC could contribute differently to the ductility and this is reasonable since the ductile-to-brittle transition temperature of elements within the same group will gradually increase from top to down, meaning a relatively less tendency for ductility in the lower part

of the periodic table. Therefore, alloying with W rather than Mo, both having the same VEC, will result in different ductility. In general, alloying with refractory elements to the left side of the periodic table such as Ti, Zr, Hf is more easily to ductilize material, while alloying with those to the right side such as Cr, Mo, W is more easily to strengthen the materials but with a decreasing ductility.

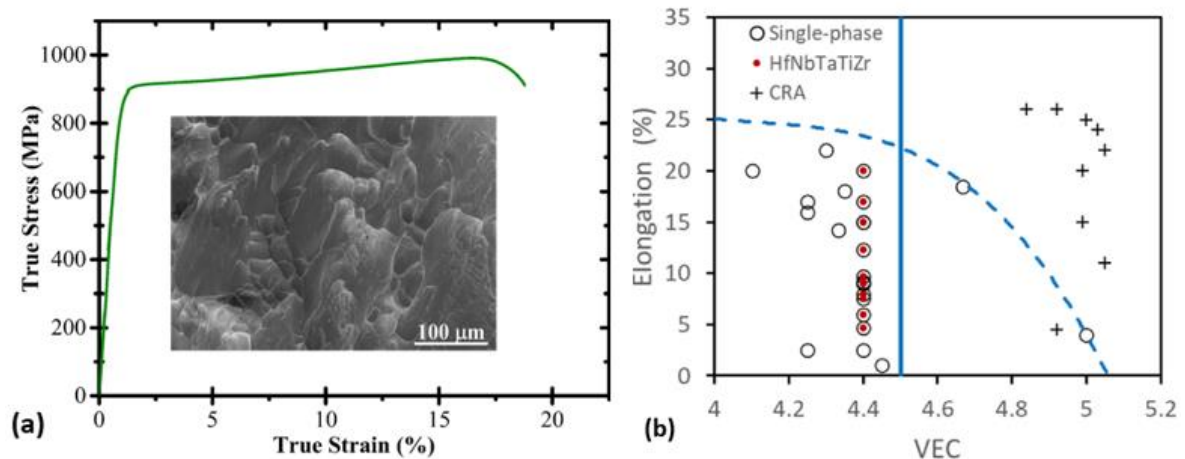


Figure 3.14. (a) True tensile stress-strain curve for as-cast $\text{Hf}_{0.5}\text{Nb}_{0.5}\text{Ta}_{0.5}\text{Ti}_{1.5}\text{Zr}$ as a proof of the VEC concept reproduced from Ref. [24] with the permission of American Institute of Physics; (b) VEC vs elongation of RHEAs, in comparison with conventional single-phase bcc refractory alloys (CRA). Reproduced from Ref. [87], with the permission of Elsevier Science & Technology Journals.

3.2.2 Transformation induced plasticity (TRIP)

The change of stacking fault energy can lead to transformation induced twinning or martensitic transformation, improving the strain hardening rate with a further increase of ductility, which is widely used in alloys designed for RT applications such as high strength steels, fcc alloys and titanium alloys. This is also called metastability-engineering to destabilize the master phase during deformation. Employing this strategy to RHEAs, ductile $\text{HfNb}_{0.18}\text{Ta}_{0.18}\text{Ti}_{1.27}\text{Zr}$ alloy [27] and Ta_xHfZrTi ($x=1, 0.6, 0.5,$ and 0.4) alloys [26] were developed. For the former case, the Ti-enriched alloy, martensitic phase transformation could be triggered by referring to the Bo-Md diagram. For the latter case, the Ta_xHfZrTi alloys, Ti group metals naturally exist in hcp structure in lower temperatures and bcc structure in high temperatures. Lowering the content of Ta, which is of bcc structure, will increase the tendency for Ti group metals to dominate the phase structure which are naturally of hcp structure at RT. Because Zr and Hf share similar physical and chemical properties with Ti, both metals can be considered as Ti equivalents to some point, which cannot keep the hcp structure to high temperatures. Obviously, such a combination is not strong enough as well ideal for high temperature applications.

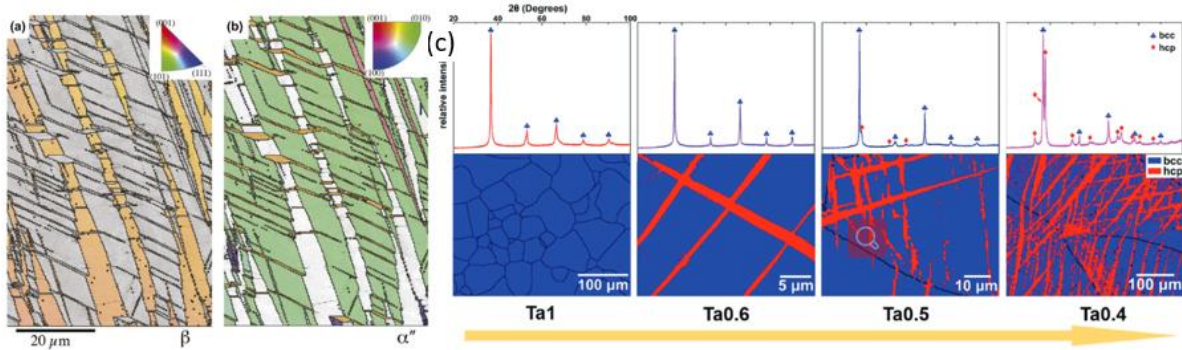


Figure 3.15. (a) Strain-induced martensitic transformation in $\text{HfNb}_{0.18}\text{Ta}_{0.18}\text{Ti}_{1.27}\text{Zr}$, reproduced from Ref. [27], Open Access (Materials Research Letters); (b) Stress-induced martensitic transformation in $\text{Ta}_{0.4}\text{HfZrTi}$. Reproduced from Ref. [26], with the permission of John Wiley & Sons – Books.

3.2.3 Solid solution softening (SSS)

While SSH is a common and effective way to strengthen bcc metals and alloys especially at low temperatures, solid solution softening (SSS) can be a unique way to soften alloys to induce ductility at RT. SSS is a well-established phenomenon [98], [99], [100], [101], [102] starting from the research on iron-based substitutional alloys [103]. It is generally observed in bcc metals at low temperatures as a result of addition of either substitutional or interstitial elements. The content of interstitial solutes required to produce maximum softening normally ranges from 0.02-0.05 at% [104], much lower than the usual 2-10 at% substitutional solutes required to produce softening under similar test conditions [103].

Before going to details, let us first revisit the deformation mechanism of bcc structured materials. As mentioned earlier, the deformation of bcc materials is temperature and strain rate dependent and mainly controlled by the motion of non-planar core of $1/2 \langle 111 \rangle$ screw dislocation. The flow stress is composed of two components: a thermal component called effective stress τ^* and an athermal one, τ_u [105]. The barriers which give rise to the thermal component are of a short-range nature and conversely the barriers which give rise to the athermal component are of a long-range nature. Hence, two of them will have different interaction between dislocations and solute additions [105]. The athermal part, τ_u , as shown below in Figure 3.16 is solely existing at the intermediate temperature range and is almost constant, which makes it basically only affected by the roughness of lattice landscape for dislocations to move across. Only the thermal part τ^* is altered by SSS, with a reduced temperature and strain rate dependence with increasing temperature and strain rate. SSS was once an important research topic with the following distinct features [99]:

- 1). Softening predominately affects the thermal part τ^* at the low temperature range, generally below $0.15 T_m$ [105], [106];

- 2). The temperature dependence of the yield stress is relatively high at low temperatures;
- 3). Both interstitial and substitutional solutes can trigger the softening effect;
- 4). Both SSH and SSS could be found in the same alloy system at different temperature ranges: for example, softening at low temperatures while hardening at high temperatures [107].

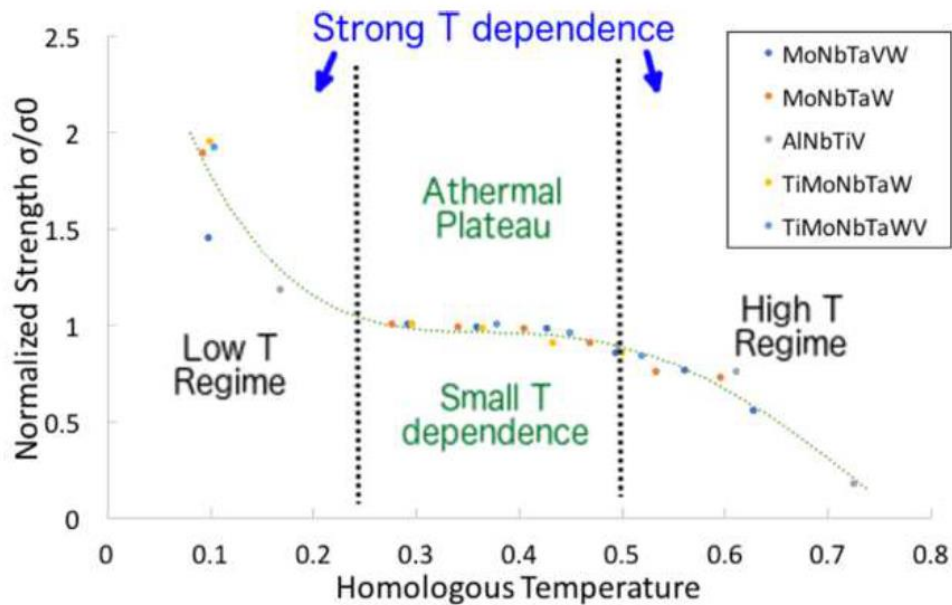


Figure 3.16. Yield stress normalized by the athermal plateau stress and plotted against the respective homologous temperature. Reproduced from Ref. [69], PhD thesis, with the permission of author, F.G. Coury.

There are basically three types of softening mechanism proposed so far, relating to different types of metals, with either intrinsic or extrinsic mechanisms associated with $1/2 \langle 111 \rangle$ screw dislocations mobility controlled by double-kink nucleation and kink migration processes: lowering the Peierls (lattice friction) stress to promote cross slip; controlling the electron concentration to below a critical number of s and d electrons; scavenging of interstitial impurities at very low solute concentration. Kink pairs along a relaxed screw dislocation line commonly exist in bcc structured materials due to their lowest Gibbs free energy. Under applied external shear stress, the lateral migration of double kink will be activated. With the help of asymmetrical $1/2 \langle 111 \rangle$ screw dislocation core, kinks are also easily formed along intersections of different glide planes which will result in cross-kink glide. When the motions of cross-kink crush into each other, they will finally lead to the formation of jogs to prohibit the further motion of dislocations, thus leading to strengthening. When it comes to the complex multi-element alloys such as RHEAs, the scenario will become even more complicated. In most cases alloys are strengthened without any trace of softening, as the added solutes are already saturated for the double-kink to form, and extra solutes restrain the further movement of screw

dislocations. Therefore, a competition between double kink nucleation and kink migration (Figure 3.17) needs to be deliberately configured to tailor the plasticity behavior of bcc materials.

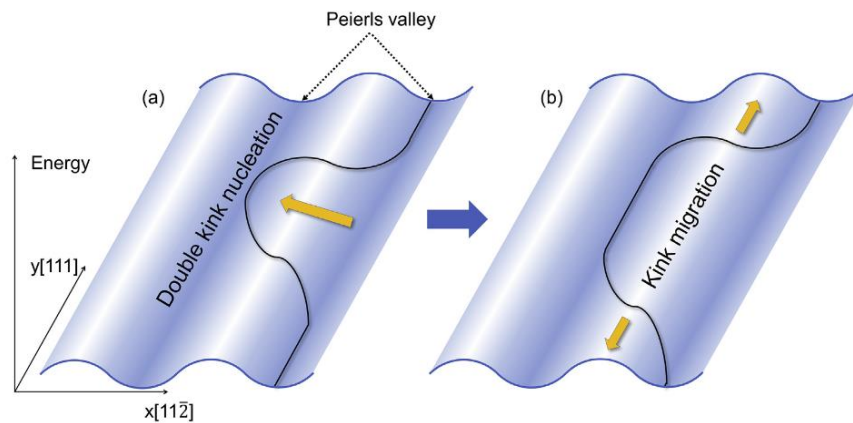


Figure 3.17. Schematic illustration of dislocation motion under the double-kink nucleation and kink migration mechanism in bcc W. (a) Double-kink nucleation: due to the thermal activation, a section of a straight dislocation could bow towards to the adjacent lattice sites to form a double-kink configuration. (b) Kink migration: under the applied stress, the kinks migrate apart along the direction of the dislocation line, which results in the whole dislocation moving to the left adjacent site. Reproduced from Ref. [108], with the permission of Elsevier.

The three types of softening phenomena mentioned above can be exemplified by three different types of alloys. Firstly, in binary iron alloys [103], the hardness values decrease in most cases with solute concentrations lower than 4 at% at 188 K and 77 K (Figure 3.18a), and the hardness values increase with the decrease of temperature (Figure 3.18b). Only in binary iron alloys with the addition of Zr and Hf, the hardness always increases which is independent of the change of temperature and solute concentration. With the addition of Nb and Ta less than 0.20 at%, the hardness values in these binary iron alloys are always lower than that of the pure iron when the test temperatures are lower than 411 K (Figure 3.18b). Based on the atomic size difference limit for favorable solid solution formation as suggested by Hume-Rothery [109], alloying elements can be divided into three groups here [103]: first category including Zr and Hf with an atomic size difference to Fe larger than 15 %, which does not generate any softening effect; second category including Nb and Ta with an atomic size difference just around 15 % which generates softening at very dilute concentrations followed by rapid hardening; the last category including all the remaining elements with an atomic size difference notably lower than 15% which are all capable of inducing softening at 77 K over solute concentrations up to 8 at% and a reduction of temperature dependence of hardness. In light of these analysis, the atomic size difference between iron and solute seems to play a dominating role in whether softening or hardening will happen. Basically, the softening and hardening of most alloys agree well with the atomic size difference rule.

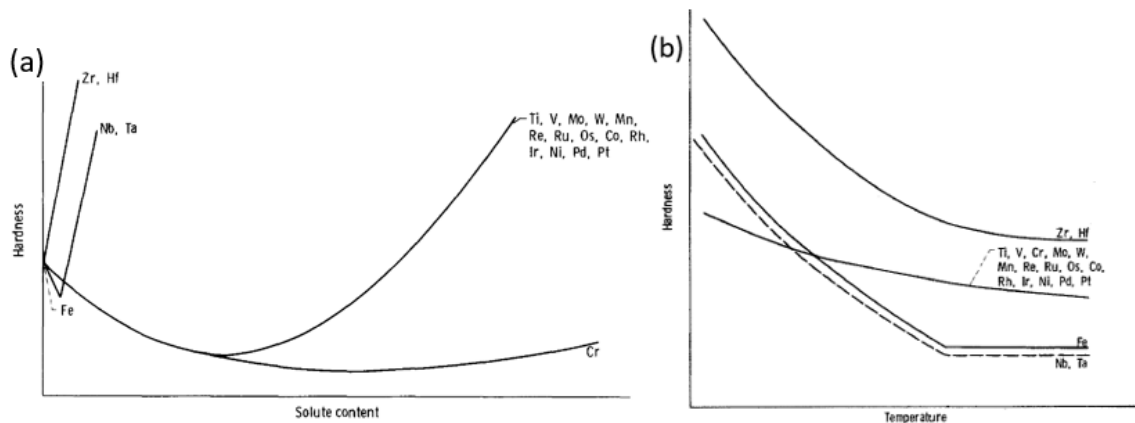


Figure 3.18. (a) Schematic representation of solute effects in binary iron alloys at 77K; (b) temperature dependence of hardness of unalloyed iron and binary iron alloys. Reproduced from Ref. [103], with the permission of Elsevier Science & Technology Journals.

Secondly, softening can be caused by the electron concentration variation, typically in Mo and W. For Mo and W alloys, Pt, Ir, Os and Re solutes lead to softening and the initial softening does not necessarily correlate with atomic radii. Instead, the solute-dislocation interactions, which change the asymmetrical dislocation core structure and elastic stress field around it, are essentially due to the electron concentration variation [101], [107], [108], [110], [111], [112]. The softening occurs within the solid solution range, which means this phenomenon can be partially or fully explained by the solid solution model. The model is developed based on thermally activated motion of screw dislocations by double-kink nucleation and kink migration processes when it comes to bcc structured materials. Both processes are rate-limited and one of them dominates at different temperatures. The stress, σ , experimentally measured against applied strain, ϵ , correlates to these two processes at a constant strain rate $\dot{\epsilon}$ [113]:

$$\dot{\epsilon} = 0.94b^2\rho_m * [(\text{nucleation rate})^{-1} + (\text{migration rate})^{-1}]^{-1}$$

where b is the Burgers vector length, ρ_m is the mobile dislocation density per area. Both rates are thermally activated and can be further elaborated by the Arrhenius equation as (attempt frequency) * $\exp[-(\text{enthalpy barrier})/(k_B T)]$, where k_B is Boltzmann's constant and T is temperature. The enthalpy barrier has a stress scale and an energy scale, and both can be affected by the addition of solutes [113]. The energy scale is connected to the direct solute-dislocation core interaction energy, while the stress scale is correlated to the Peierls misfit (the ability to change stiffness) for moving a single atomic row in the screw dislocation core. We take the softening effect in Mo alloys here as an example. Re shows a weak, short-range interaction with Mo, but it has a larger Peierls misfit associated with the stress scales than Pt does in this case (Figure 3.19 a1, b1). The weaker interaction and larger Peierls misfit of

Re produce a small softening effect; but these effects enhance at high concentrations where multiple solutes interact with dislocations. The stronger attractive interaction of Pt produces a substantial change in the energy scale and strong initial softening but quickly leads to hardening at higher concentrations [113]. The predicted strength for Mo-Re and Mo-Pt with changing solute concentration for several temperatures compared with experimental results is shown in Figure 3.19 a2, b2 [113]. The attractive interaction of Re to Mo leads to softening for low solutes because of the increased double-kink nucleation. As the concentration increases, there is a crossover to kink migration dominated flow stress which hardens with additional solutes. The crossover happens at lower concentration for higher temperatures because kink migration becomes more dominated than double-kink nucleation at higher temperatures. The same trend goes for the Mo-Pt case.

The direct solute-induced changes to energy and stress scales of double-kink nucleation and kink migration are sufficient when coupled with correct interaction parameters, to quantitatively interpret experimental observations [113]. The same calculation method has been used for W [108] and other bcc metals [107]. Al and Mn were proposed to be promising substitutes for Re as these two elements could introduce similar softening effects as what Re does in bcc W from simulations [108].

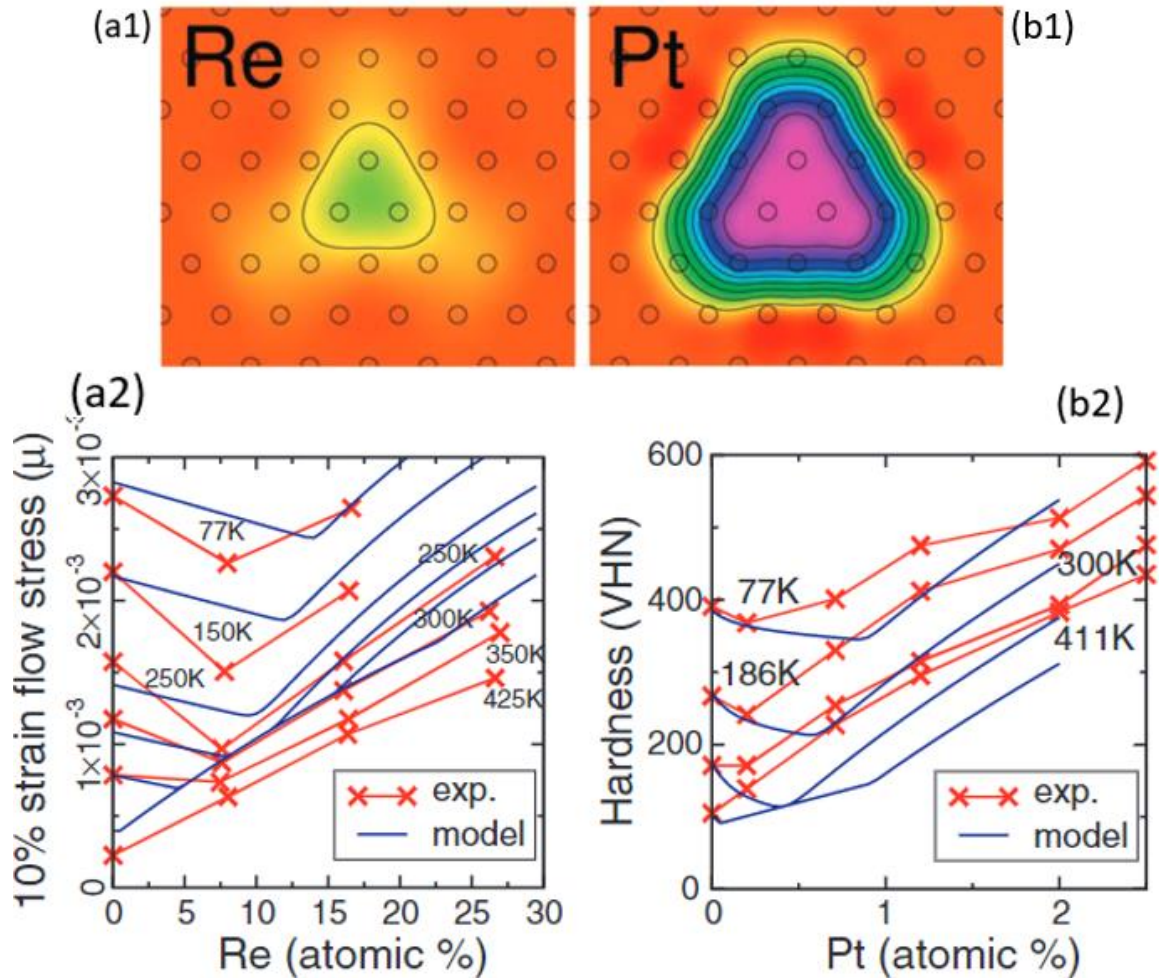


Figure 3.19. Solute-dislocation interaction-energy profile for Re (left) (a1) and Pt (right) (b1) in Mo. The contours are at 0.1-eV intervals, and the interaction is attractive for all sites. Each circle is a possible lattice site for a solute atom in an atomic row; the dislocation is located in the center of the profile. The Pt dislocation interaction is stronger and has a longer range than Re. The interaction energy E_{int} is the maximum value in the profile. Predicted strength for Mo-Re and Mo-Pt are shown as a function of solute concentration for different temperatures, compared with experiments. (a2) Flow stress at 10% strain for Mo-Re and experiments. The flow stress is normalized by the shear modulus ($\mu=139$ GPa). (b2) Vickers hardness number (VHN) for Mo-Pt and experiments. Reproduced from Ref.[113], with the permission of American Association for the Advancement of Science.

Thirdly, softening can be caused by scavenging of interstitial impurities at very low solute concentrations, typically in Nb and Ta. There are studies revealing that the softening effects in Nb and Ta alloys can be eliminated by using high-purity raw metals, which suggest that softening is related to the interstitial impurity [106], [114], [115].

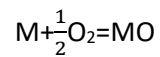
In addition, softening also happens in some iron-based alloys with precipitates [101]. Quenching and micro- and macro-deformation can reduce or prevent softening. The mechanisms involved in these

observations are still not clear and they might be different with different materials. In general, SSS is not common in metallic materials, and efforts are desperately needed to dedicate into this research field in the future.

3.3 Oxidation resistance (Target No.3)

3.3.1 Thermodynamics of oxidation

The oxidation of materials working at high temperatures can cause degradation and lead to premature failure, which could be a disaster for materials. Thus, research on the high temperature oxidation of metals and alloys is important. Materials will react with oxygen differently depending on the chemical reaction environment and conditions. For regular oxidation of metallic materials, the major reaction taking place is as follows:



Under different temperatures and pressures, the reaction direction and stability of a system are determined by the Gibbs free energy, G , which is:

$$G = H - TS$$

Where H is the enthalpy, T is absolute temperature, and S is entropy. The reaction with the direction of lowering G will be prioritized. Figure 3.20 is the Ellingham diagram displaying the standard free energy G for the formation of different oxides under different partial oxygen pressures and temperatures at the equilibrium state. In general, negative ΔG values indicate spontaneous reactions, while the position and intersection of the Gibbs free energy curves help predict the reduction behavior of metal oxides at different temperatures. An obvious tendency is that oxidation reactions will get severe with an increase in temperatures. In terms of the three groups (IV, V and VI) of refractory metals, the oxidation under identical conditions follows this sequence: Zr (Hf), Ti, V (Nb, Ta), Cr, Mo (W). It is worth noting that most refractory oxides are unfortunately non-protective thus strategies are desperately needed to improve their intrinsic oxidation resistance.

Ellingham Diagrams

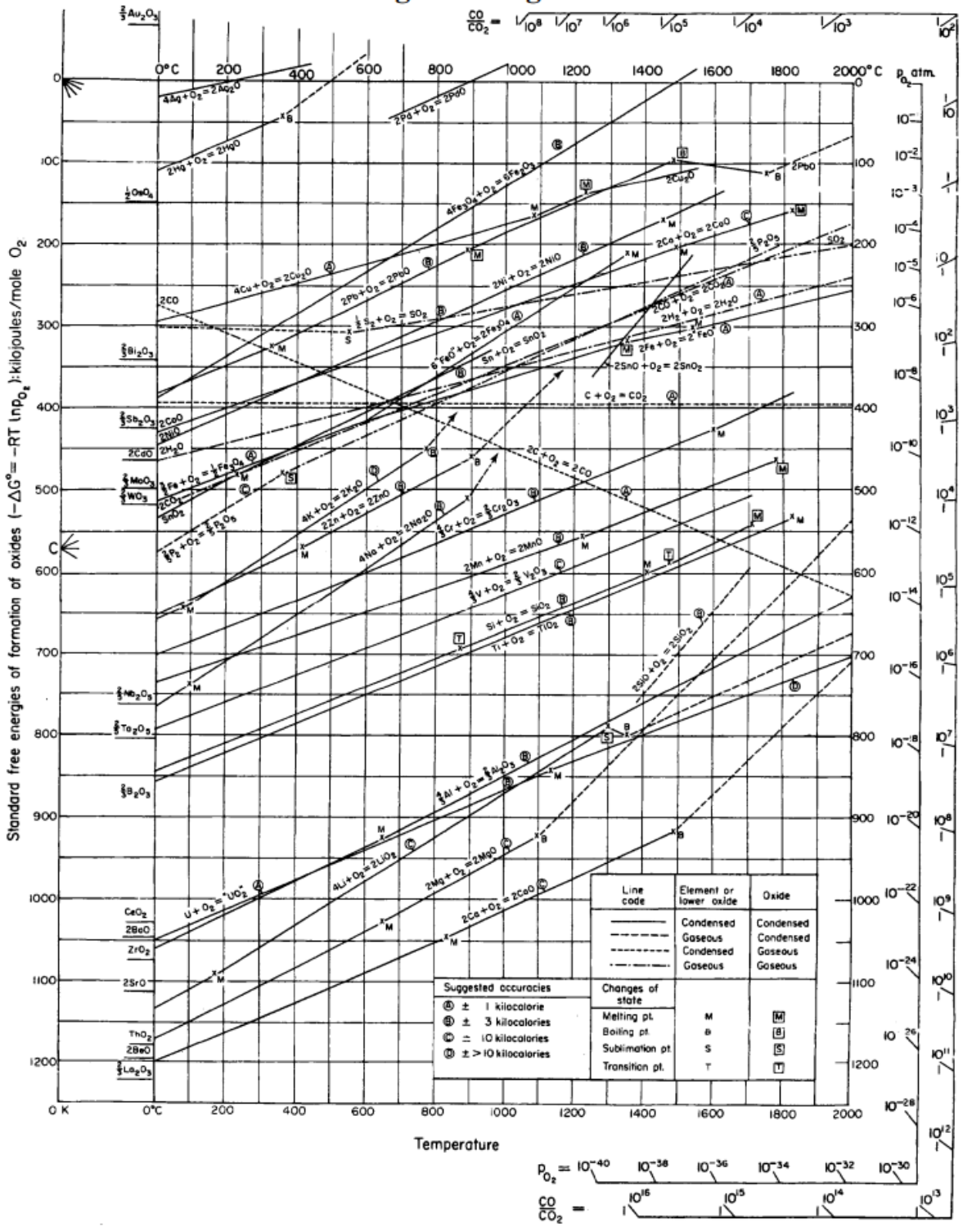


Figure 3.20. Ellingham diagram for several metals giving the free energy of formation of metal oxides and the corresponding oxygen partial pressure at equilibrium (reproduced from Ref. [116], with permission From Academic.edu, open access).

3.3.2 Kinetics of oxidation

Oxidation kinetics studies the rate at which oxidation reaction occurs to characterize the oxidation behavior of materials. It depends on factors such as the alloys composition, temperature, pressure, and sometimes catalysts. The experimental oxidation data can be fitted into the classical oxidation rate equation listed below [117]:

$$\frac{\Delta m}{SA} = k_p * t^n$$

Here, Δm and SA are the mass change in mg and the initial sample surface area in cm^2 , $\frac{\Delta m}{SA}$ is the specific mass change with unit of mg/cm^2 , respectively. k is the oxidation rate constant; t is the oxidation exposure time and n is the time exponent. Several typical types of oxidation behavior are listed here according to their oxidation time exponent: linear oxidation with $n = 1$, typical for metals with porous or cracked oxide scales, e.g. Nb, Ta; parabolic oxidation with $n = 0.5$, typical for metals with oxides controlled by diffusion; logarithmic oxidation with $n < 0.5$, typical for metals with fast oxidation at the start then decrease to a very low value, e.g. Al; catastrophic at HT, rapid exothermal reactions, and oxides are volatile, e.g. Mo, W, V.

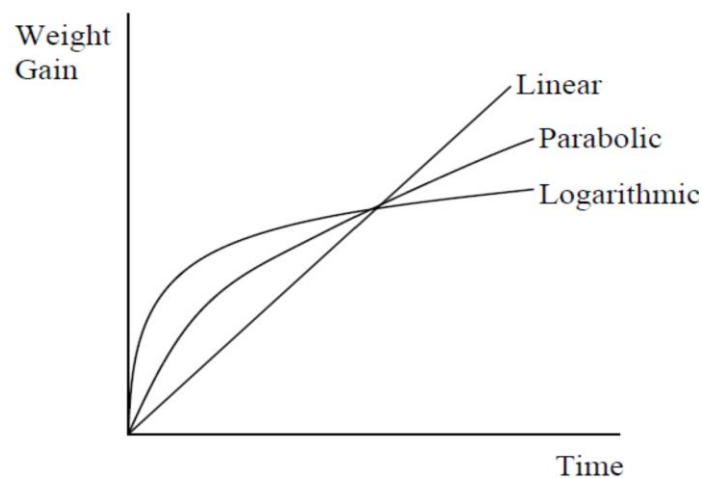


Figure 3.21. Common oxidation kinetics laws describing the rate of growth of an oxide layer

Meanwhile, the Pilling–Bedworth ratio [118], defining as the ratio of the volume of a metal oxide to the volume of the corresponding metal, for different oxides can be decisive.

$$PBR_{metal} = \frac{Volume\ of\ oxide}{Volume\ of\ metal}$$

This ratio is also directly related to the growth stress of the oxides due to the volume mismatch which affects the formation of oxide scales. For instance, ZrO_2 and TiO_2 with a high Pilling–Bedworth ratio of

1.56 and 1.73 seen in Table 3.1 below, facilitate the formation of passive and protective scales. As for the stable oxides of V_2O_5 , MoO_3 , WO_3 , they are easy to get evaporated due to their low melting points and boiling points. For the oxides of Nb_2O_5 , Ta_2O_5 , they have an even larger Pilling–Bedworth ratio over 2 which will be easily spalled off with a larger volume compared to the substrate metals. Thus, there is a consensus that refractory alloys cannot be directly used for high temperatures unless some intrinsic oxidation resistance is provided by themselves. Protective coating is an option but still, there is a high risk if the coating fails. The research on the oxidation resistance of refractory materials is of course important.

Table 3.1 Valence, ionic size, and oxide characteristics of alloying elements added to niobium [119].

Element	Valence	Goldschmidt Ionic Radius, Å	-ΔF at 1300 K, kcal per g atom of oxygen	Oxide Properties			Oxide- Metal Volume Ratio
				Melting Point, C	Boiling Point, C	Conductivity at 20 C, ohm ⁻¹ cm ⁻¹	
Mn	2	0.80	69.3	1790	--	1 × 10 ⁻⁸	1.79
Zr	4	0.79	101.4	2715	--	<10 ⁻⁸	1.56
Co	2	0.72	33.3	1810	--	1 × 10 ⁻²	1.86
Ni	2	0.69	28.6	1960	--	8 × 10 ⁻⁴	1.65
Nb	5	0.69	63.9	1460	--	1.2 × 10 ¹	2.69
Ta	5	0.68	70.8	>1900	--	1 × 10 ⁻⁵	2.54
Ti	4	0.68	84.8	1860	--	4 × 10 ⁰	1.73
Fe	3	0.64	39.0	--	--	2.1 × 10 ¹	2.14
Cr	3	0.63	63.6	2440	--	1.2 × 10 ⁻⁴	2.07
Mo	6	0.62	35.5	795	1460	1.3 × 10 ⁻⁷	3.24
W	6	0.62	41.3	1470	1750	5 × 10 ⁻²	3.35
V	5	0.59	49.6	660	--	3 × 10 ⁰	3.19
Re	7	0.56	21.6	266	363	<10 ⁻⁸	1.67
Al	3	0.50	100.3	2020	--	<10 ⁻⁸	1.49
Si	4	0.41	77.2	1713	--	<10 ⁻⁸	2.21
Be	2	0.35	112.8	1283	--	<10 ⁻⁸	1.68
B	3	0.23	76.5	450	--	<10 ⁻⁸	2.02

Next important parameter is the coefficient of thermal expansion (CTE) which is linearly associated with thermal stress of oxides. CTE describes the fraction of the change in length (or volume) caused by a change in temperature per unit. The coefficient of linear thermal expansion (α) can be calculated using the equation below [120]:

$$\alpha = \frac{1}{L} \frac{dL}{dT}$$

where L is the initial length and $\frac{dL}{dT}$ is the rate of change of length with temperature. The unit is K⁻¹. Metals and alloys generally have CTE values ranging from 10×10^{-6} to 30×10^{-6} K⁻¹, while ceramics exhibit lower values. CTE is temperature-dependent and usually increases continuously with temperature. The coefficient of linear thermal expansion of some refractory metals as a function of testing temperature is shown in Figure 3.22. Here, Nb shows the highest linear coefficient of thermal expansion and continues to rise with temperature, approaching 9×10^{-6} K⁻¹ at 1400°C, followed by Ta, Mo, and W. When working in high-temperature environments, selecting materials with low coefficient

of thermal expansion can reduce the generation of thermal stress and help to prevent structural damage.

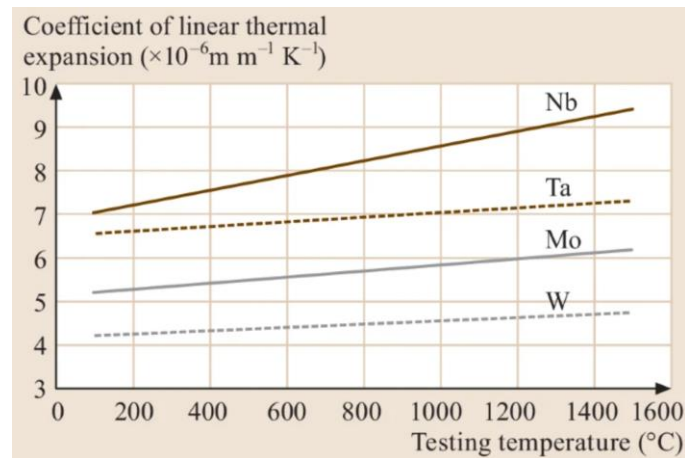


Figure 3.22. The coefficient of linear thermal expansion of some refractory metals as a function of temperature. Reproduced from Ref. [121], with the permission of Springer Nature.

3.3.3 Complex oxides

Based on the previous knowledge gained from traditional alloys, one typical way to improve the oxidation resistance of metallic materials is seeking the formation of protective oxide scales by alloying elements such as Cr, Al, and Si. Furthermore, the Gibbs free energy of formation of these oxides (Cr_2O_3 , Al_2O_3 , and SiO_2) is lower than that of other refractory oxides, which will facilitate their selective oxidation prior to the formation of refractory oxides. These oxides are oxidation resistant and can work in certain ranges of temperatures. Especially, the addition of Cr can have a potent positive effect on the accelerated formation of the Al_2O_3 oxide, and these two elements, i.e., Cr and Al, are commonly used together to improve the oxidation resistance of alloys. The Al_2O_3 scale has high thermal stability and can work along a high temperature range up to about 1400°C , which is an ideal choice for almost all anti-oxidation scenarios. Cr_2O_3 is stable working under 1050°C , and higher temperatures would lead to the formation of volatile CrO_3 [122]. The Al_2O_3 scale exhibits parabolic growth behavior, with its rate constant being an order of magnitude lower than that of the Cr_2O_3 scale [123], [124], and also has relatively low rates of diffusion for both oxygen and metal ions. SiO_2 is normally used in Nb and Mo alloys, and it is usually combined with B to increase the fluidity of the self-healing SiO_2 protective scale. SiO_2 can work at high temperatures up to 1700°C [125]. However, a complicating factor for both Cr_2O_3 and SiO_2 scales is volatility, especially in the presence of water vapor and/or in environments with the flow, which can significantly reduce the maximum-use temperature by several hundred degrees. There are already some trials and errors pursuing the formation of Al- or Cr- related oxides scales in RHEAs [126], [127], [128], [129], [130], [131], [132], [133], [134]. Particularly, the (Ti)AlCrMo-(Ta, Nb) system was extensively researched [135], [136]. Regarding the research on oxidation of RHEAs, the

content of added Cr, Al and Si, usually less than 25 at% in commercial anti-oxidation alloys, also needs to be carefully studied. On the one hand, the alloying elements need to be sufficient to ensure the formation of protective oxide scales; on the other hand, their content needs to be controlled to prevent the formation of undesirable intermetallic phases, so as not to jeopardize the mechanical performance. Same as the synergistic effect of adding Cr and Al into traditional alloys, the content of Cr and Al simultaneously added into RHEAs should be controlled [137]. Due to the larger atomic size and electronegativity difference between refractory elements and Al, Cr and Si, the balance of forming protective scales and forming intermetallic phases needs to be considered. There is always the presence of intermetallic phases such as C14-type Laves phase ($\text{Cr}_2\text{Ta}/\text{Cr}_2\text{Nb}$), A15 phase ($\text{AlMo}_3/\text{Al}(\text{Mo}, \text{Nb})_3$), and the ordering of A2 to B2. Meanwhile, complex and protective rutile type oxides (like CrTaO_4 , CrNbO_4) can be formed. Here, the addition of Ti plays a crucial role in that their (CrTaO_4 and CrNbO_4) formation simultaneously decreases the amount of less favorable oxides (Nb_2O_5 , Ta_2O_5) and can suppress the formation of A15 phase to some degree [137]. The discovery of the protective scale CrTaO_4 is highly meaningful [135], [138]. This new strategy to intrinsically protect RHEAs at ultra-high temperatures was applied to the equiatomic TaMoCrTiAl RHEA [139]. What one can see from Figure 3.23 below is that the alloy has quite good oxidation resistance at high temperatures and the oxidation kinetics curves show the parabolic rate rather than the linear rate.

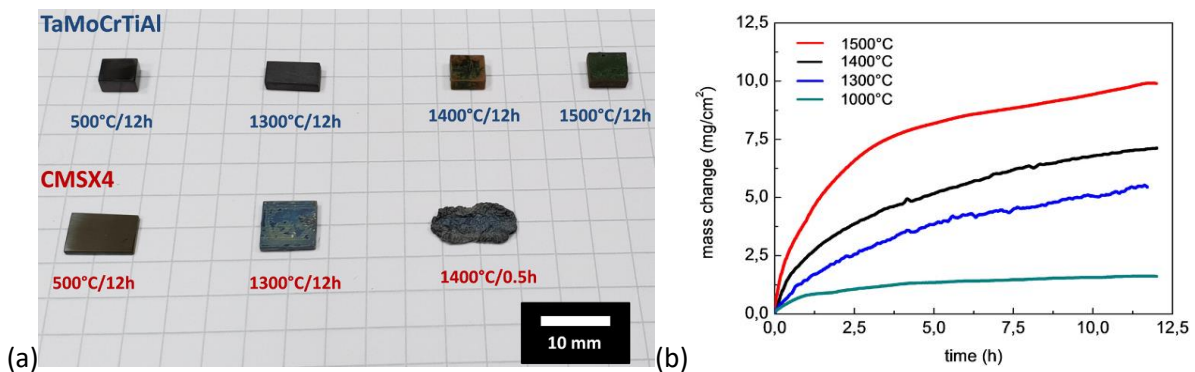


Figure 3.23. (a) Macroscopic micrographs of the TaMoCrTiAl RHEA and the CMSX4 alloy after being oxidized at 500 °C, 1300 °C, 1400 °C and 1500 °C for 12h. (b) The oxidation curves of the TaMoCrTiAl RHEA at 1000 °C, 1300 °C, 1400 °C and 1500 °C. Reproduced from Ref. [139], with the permission of Elsevier Science & Technology Journals.

The EDX analysis results from Figure 3.24a [139] on the cross-section of the TaMoCrTiAl RHEA confirmed the formation of a stable CrTaO_4 layer. Additional elements such as Ti and Al are also involved in the formation of this protective oxide. This CrTaO_4 layer seems to be highly adhesive to the substrate RHEA and to suppress the formation of Cr-related intermetallics.

Figure 3.24b [139] compares the determined parabolic growth rate constant of CrTaO_4 to that of the well-known and widely applied protective oxides such as Al_2O_3 , Cr_2O_3 , SiO_2 . Cr_2O_3 -forming alloys are often used, and their thermal stability is limited to temperatures below 1050°C since at higher temperatures the volatile CrO_3 will form and evaporate leading to a continuous mass loss and unacceptable oxidation rate [140]. Al_2O_3 is stable in a quite wide temperature range and is preferential. For example, Ni-based superalloys are protected by Al_2O_3 scale. While SiO_2 exhibits even lower growth rates at very high temperatures, protective scale only forms above 800°C . At lower temperatures, due to the sluggish diffusion the slow growth rate of SiO_2 prevents the development of a continuous layer resulting in the formation of mixed non-protective oxides [141]. Finally, the growth rate of CrTaO_4 is only marginally higher than that of Al_2O_3 and lower than that of Cr_2O_3 , which makes this type of protective scale competitive along a wide range of temperatures from 500°C to 1500°C . Apparently, the formation of CrTaO_4 is beneficial and is showing some promise for the intrinsic oxidation resistance of RHEAs. There are some other trials as well, for example, the addition of Al to form the AlNbO_4 complex oxides [142], [143], [144] although its protection efficacy is not as good as that of CrTaO_4 in that AlNbO_4 is not continuous and adherent, leading to relatively poor oxidation resistance.

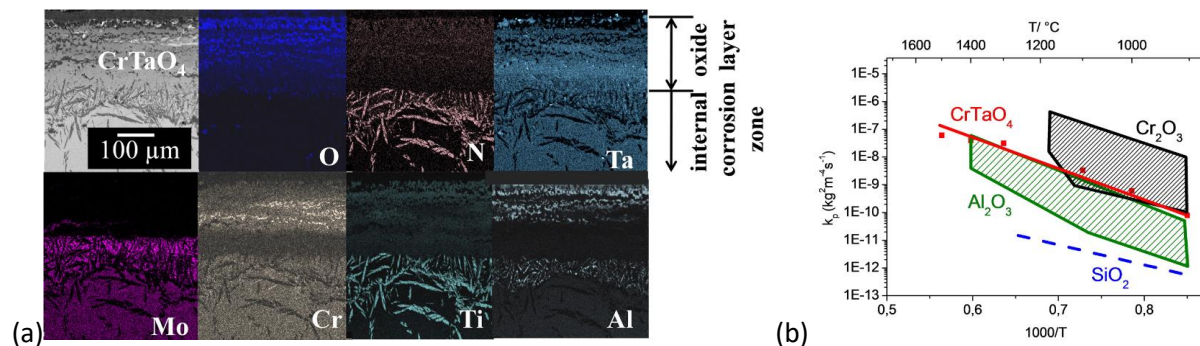


Figure 3.24. (a) Cross-section microstructure and EDX analysis of the equiatomic TaMoCrTiAl RHEA after oxidation at 1500°C for 12h; (b) comparison of the parabolic oxidation constants of CrTaO_4 with those of approved protective oxides Cr_2O_3 , SiO_2 and Al_2O_3 . Reproduced from Ref. [139], with the permission of Elsevier Science & Technology Journals.

3.3.4 Surface coating

The alloying way to form protective scales of Cr_2O_3 , Al_2O_3 and SiO_2 is challenging, since the required amount of added Cr, Al and Si to preferably form Cr_2O_3 , Al_2O_3 and SiO_2 would highly probably trigger the formation of detrimental intermetallic compounds. Alternatively, surface coating could be employed to enable oxidation resistance without affecting much the base alloy. As an example, surface coating by aluminizing [145], [146], [147] was applied to ductile RHEAs, aiming for the formation of stable, continuous and adherent Al_2O_3 scale, with a lower growth rate than Cr_2O_3 [148] and non-volatile nature. The base alloy, a $\text{Hf}_{0.5}\text{Nb}_{0.5}\text{Ta}_{0.5}\text{Ti}_{1.5}\text{Zr}$ (S1) RHEA prepared by arc melting

followed by drop-casting, was aluminized via the pack cementation method. The pack cementation aluminizing was conducted on a vacuum furnace after Ar purging at 900°C for 2h and 5h, respectively [149]. Noticeably, the specimen S1-Al,Cr-5h-O (with the aluminizing time of 5h, and the pack composition is provided in the figure caption in Figure 3.25) shows no indication of peeling after oxidation in air in a box furnace at 800 °C for 5h in comparison to that of the specimen S1-Al,Cr-2h-O (with the aluminizing time of 2h, instead of 5h), see Figure 3.25 below. Both conditions are significantly improved on oxidation resistance with the protection of a thin layer of continuous and adherent Al₂O₃ scale, see Figure 3.26.

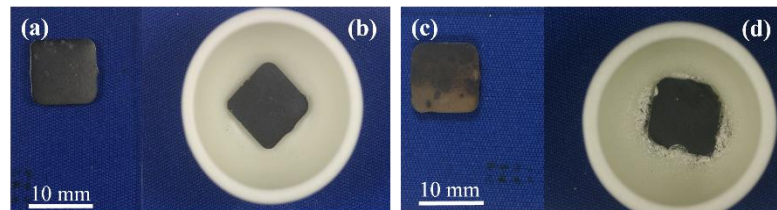


Figure 3.25. (a) and (b) show the as-aluminized specimen S1-Al,Cr-5h-A and the oxidized specimen S1-Al,Cr-5h-O; (c) and (d) show the as-aluminized specimen S1-Al,Cr-2h-A and the oxidized specimen S1-Al,Cr-2h-O. (pack composition of S1-Al,Cr: 24.5 wt.% Al +24.5 wt.% Cr+ 49.0 wt.% Al₂O₃+2.0% wt.% NH₄Cl). Reproduced from Ref. [149], with the permission of Elsevier.

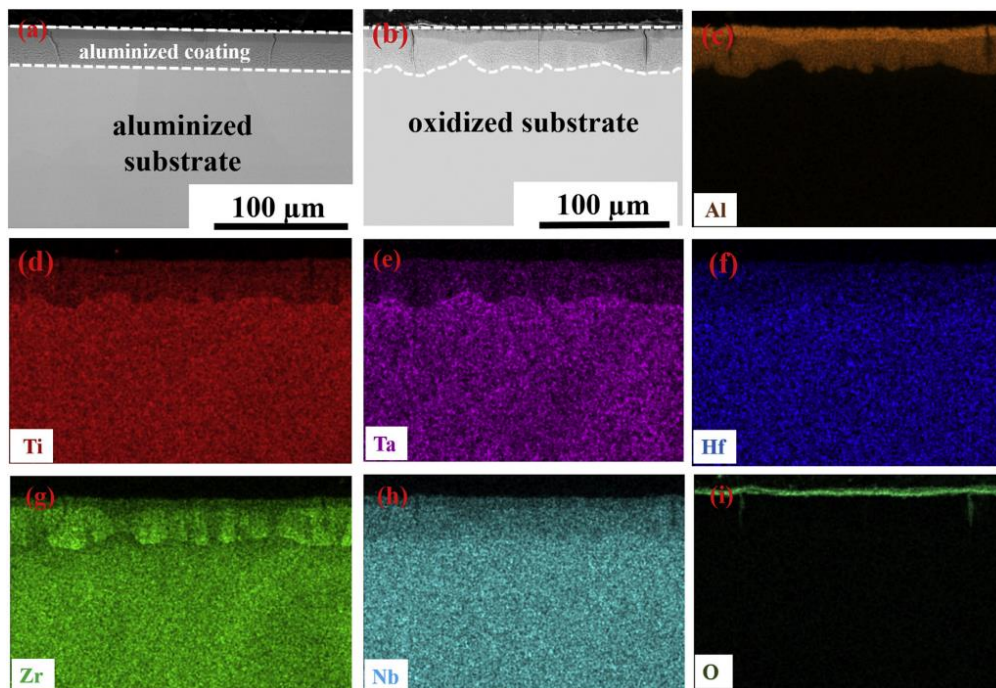


Figure 3.26. (a) and (b) Cross-sectional microstructure of the specimens S1-Al,Cr-5h-A and S1-Al,Cr-5h-O. SEM-EDS elemental maps for the S1-Al,Cr-5h-O specimen are given shown in (c)–(i), with cracks shown. Reproduced from Ref. [149], with the permission of Elsevier.

The pack cementation aluminizing processing was further optimized and a two-step aluminizing was applied to another ductile $\text{Al}_{0.5}\text{Cr}_{0.25}\text{Nb}_{0.5}\text{Ta}_{0.5}\text{Ti}_{1.5}$ RHEA [150]. The drop-cast $\text{Al}_{0.5}\text{Cr}_{0.25}\text{Nb}_{0.5}\text{Ta}_{0.5}\text{Ti}_{1.5}$ RHEA with dimensions of $5 \times 10 \times 10 \text{ mm}^3$ were covered in a powder mixture with the composition 24.0wt% Al + 24.0wt% Cr + 51.0wt% Al_2O_3 + 1.0%wt. % NH_4Cl , and placed in an alumina crucible. This crucible was later put into a vacuum furnace to be heated at 1050°C for 2h and subsequently heated at 800°C for 6h followed by furnace cooling. After finishing the two-step aluminizing, the $\text{Al}_{0.5}\text{Cr}_{0.25}\text{Nb}_{0.5}\text{Ta}_{0.5}\text{Ti}_{1.5}$ RHEA was subjected to a total of 20 cycles of oxidation experiments under static air in an automated thermal cycling furnace, and in each cycle the alloy was heated up to 1100°C , kept for 1h, cooled down to room temperature and kept for 20mins, with the heating/cooling rate being $15^\circ\text{C}/\text{min}$. The two-step aluminized $\text{Al}_{0.5}\text{Cr}_{0.25}\text{Nb}_{0.5}\text{Ta}_{0.5}\text{Ti}_{1.5}$ RHEA showed a significant low weight gain compared to the as-cast counterpart alloy, with no indication of spallation shown in the optical images, see Figure 3.27(a). Seen from the cross-section microstructure shown in Figure 3.27(b), a dense, continuous, adherent and crack-free Al_2O_3 scale was formed on the base RHEA.

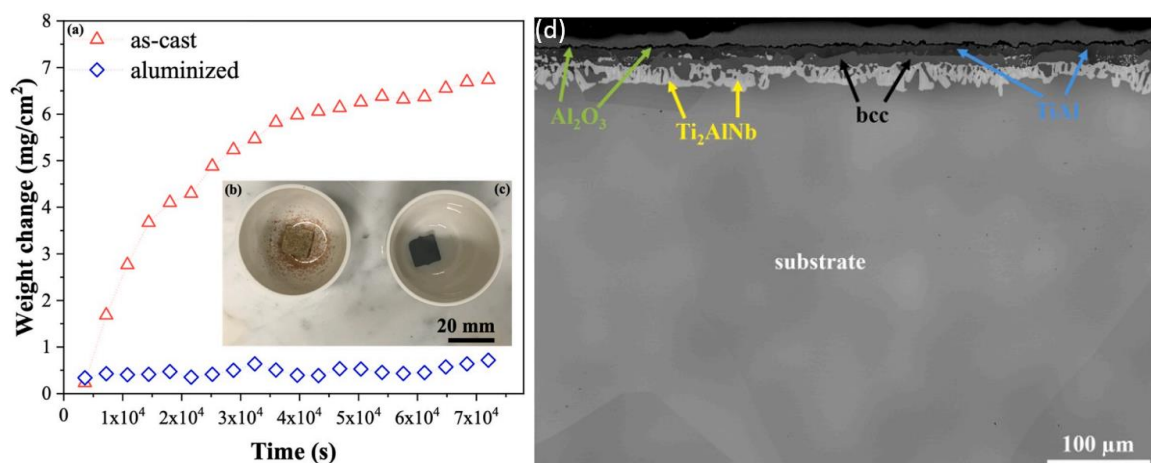


Figure 3.27. (a) Weight change per unit area vs. time plot for the $\text{Al}_{0.5}\text{Cr}_{0.25}\text{Nb}_{0.5}\text{Ta}_{0.5}\text{Ti}_{1.5}$ RHEA after a total of 20 cycles of oxidation tests; appearance of (b) as-cast and (c) aluminized RHEAs, after 20 cycles of oxidation tests. (d) a low-magnification SEM micrograph with a large field of view showing the formation of continuous, dense and uniform Al_2O_3 scale on the cross-section of the RHEA specimen after 20 cycles of oxidation tests.

Reproduced from Ref. [150], with the permission of Elsevier.

In summary, research on how to improve the oxidation resistance of refractory alloys [151], [152] is of crucial importance to widen their applications, and more work surely needs to be done in the future, adopting both alloying and/or surface coating approaches.

4 Experimental method

4.1 Arc-melting

All the alloys studied were prepared by the arc-melting equipment supplied by Edmund Bühler GmbH. Melting was carried out through vacuum arc-melting a mixture of different constituent elements with purity higher than 99.9 wt.% in a Ti-gettered high purity argon atmosphere. Different metals were arranged in a way with decreasing melting points from the top to the bottom to minimize the possible evaporation of low melting point elements. The melting and flipping of button ingots by mechanical manipulator were repeated at least five times to insure the chemical homogeneity of the alloy. The arc melter employs a non-consumable tungsten electrode to generate electric arc that heats up the gas and creates plasma. High vacuum is obtained by two-step pumping, firstly using the rotary pump to evacuate the whole system to lower pressure better than $3.0 \cdot 10^{-3}$ mbar, then using a diffusion pump to further evacuate the system to a pressure level better than $5.0 \cdot 10^{-5}$ mbar. The casting mold, melting plate and crucible are all made from copper and water-cooled by an external chiller to conduct heat quickly and prevent the overheating of the equipment.



Figure 4.1. Arc melter from Edmund Bühler GmbH

4.2 Vickers hardness measurement

Hardness quantifies a material's ability to resist plastic deformation from a standard source, normally diamond. Vickers hardness is commonly denoted as HV. With a given load, F , in kilogram-force, an

indentation imprint in square millimeters can be generated. The Vickers hardness can be calculated by the following equation [153], with d being the mean length of diagonals of the indentation imprint.

$$HV \approx 0.1891 \frac{F}{d^2} [\text{N/mm}^2]$$

4.3 Oxidation test

Oxidation tests of the target alloys were carried out in a ceramic tube furnace pre-heated to 800°C, 1000°C and 1200°C for 1h, 8h and 24h in static laboratory air. The specimens were in the form of cubic blocks with approximate dimensions of 4 × 4 × 4 mm³. Before oxidation tests, the surfaces of each specimen were ground to 800-grit finish, ultrasonically cleaned in the ethanol followed by air drying. The surface area (including all six faces) was accurately calculated by carefully measuring the dimensions of each specimen. The specimen was loaded in a crucible with dimensions of 20 × 20 × 20 mm³, and the crucible with the specimen inside was weighed before and after the oxidation tests, using a highly sensitive balance (to the precision of 10⁻⁶ g) to evaluate the weight change. To prevent any loss of oxidation products during the oxidation tests and/or cooling in the air, an alumina lid was placed to cover the crucible throughout the oxidation and weighing process. Finally, the specific mass change was determined, dividing the measured mass change by the initial surface area of the specimen.

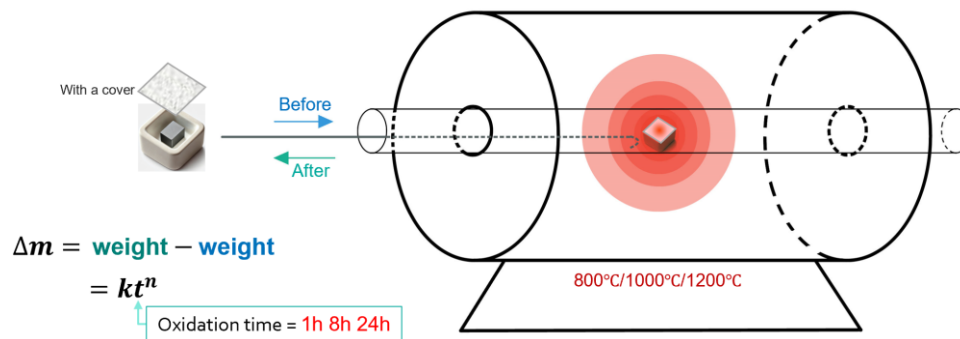


Figure 4.2. Illustration of the oxidation tests

4.4 High temperature hardness test

Hardness from RT to 1000°C was tested by a high temperature Vickers hardness tester (Intesco-HTM 1400) under high-vacuum, with a load of 1.0 kgf and a dwell time of 10 s. The hardness value was averaged from around 5 indentations at each temperature.

4.5 Universal compression test at room temperature

Cylindrical specimens with a diameter of 6 mm and height of 9 mm were used for all compressive tests. A Zwick Roll Z050 equipment (for (HfNbTi)₈₅Mo₁₅ alloys) and an Instron 5500R (for Nb-Hf-Ti-W series alloys) were employed to measure the RT compressive yield stress in laboratory air with an initial strain rate of 0.001/s and a maximum engineering strain of around 25% (Zwick Roll Z050) and 60%

(Instron 5500R), respectively, due to the load cell capacity. For each composition, at least two tests were repeated, and the results were highly reproducible.

4.6 Gleeble compression test at high temperatures

HT compressive yield stress was measured by Gleeble 3180 (for (HfNbTi)₈₅Mo₁₅ alloys) and 3800 (for Nb-Hf-Ti-W series alloys) under vacuum (<5.3*10⁻¹ mbar for 3180 and 3.0*10⁻³ mbar for 3800) with an initial strain rate of 0.001/s and a target engineering strain of 60% (for 3180) and 30% (for 3800), respectively. Each composition was tested 3 times per temperature.

4.7 X-ray diffraction

X-ray diffraction was used to determine the crystalline structure. The atoms or molecules of the crystal cause a beam of incident X-rays to diffract along various specific directions, producing secondary waves spreading from electrons. These waves cancel each other in most directions through destructive interference and they only interfere constructively in some directions, determined by the Bragg's law given below, where n is the diffraction order, λ is wavelength of the X-ray source, d is the interplanar distance and 2θ is the diffracted angle [154]. The diffracted planes were then matched to those in standard crystallography databases. In this work, a Bruker AXS D8 X-ray diffractometer (XRD) equipped with Cu-K α radiation was used. The generator was set to 40 kV acceleration voltage and 40mA current.

$$n\lambda = 2d\sin\theta$$

4.8 Microstructural investigation

Prior to investigating the microstructure using any electron microscope, the as-cast alloys were cut by precision saw and then mounted with polyfast by the hot mounting method using a Citopress 20 equipment. Mounted samples were then ground by SiC sandpapers attached to a rotating disk. Fine polishing was done using different clothes with suspension of 9, 3, 1, 0.05 μ m grit size subsequently.

For the focused electron beam of SEM, electrons are generated either by field emission gun (FEG) or a source of tungsten or LaB₆. Generated electrons are accelerated through various apertures at a rather high voltage (keV). The beam is then focused by means of various electromagnetic lenses; and scanning coils are used to move the electron beam over the samples surface [155]. Incoming electrons interact with the sample surface, and they are captured by the detector, and later amplified, finally displayed on a TV-screen. The microstructures of refractory alloys were studied on the 0.05 μ m alumina suspension polished surface using the back-scattering electrons (BSE) mode on a LEO FEG-SEM 1550 and GeminiSEM 450 equipped with energy dispersive spectrometer (EDS) and electron backscatter diffractometer (EBSD).

5 Summary of key results

5.1 Trade-off of ductility at RT and strength at HT: Solid solution softening (SSS) and/or solid solution hardening (SSH)

5.1.1 Minor substitutional additions into originally ductile RHEAs: A case for $\text{Hf}_{20}\text{Nb}_{29.75}\text{Ta}_{29.75}\text{Ti}_{18}\text{-X}_{2.5\text{ at}\%}$ (X=Mn, Al, Cu, Fe)

RHEAs with nominal compositions of $\text{Hf}_{20}\text{Nb}_{31}\text{Ta}_{31}\text{Ti}_{18}$ (in at. %, denoted as HNTT) and $\text{Hf}_{20}\text{Nb}_{29.75}\text{Ta}_{29.75}\text{Ti}_{18}\text{-X}_{2.5}$ (X=Mn, Al, Cu, Fe, denoted as HNTT-Mn, HNTT-Al, HNTT-Cu, HNTT-Fe, respectively) were arc-melted using high purity (>99.95%) elements at least 5 times to ensure chemical homogeneity followed by furnace cooling. The nominal content of doped alloying elements was fixed to be 2.5 at.%, to separate the effect of the micro-alloying level on SSH or SSS. Regarding the choice of alloying elements, Mn and Al were selected based on the first-principles calculation results [95], while others were added mainly for the comparison purpose. Directly melted HEAs showed dendritic microstructure enriched with Ta and inter-dendritic microstructure enriched with Ti and Al, from SEM-BSE and EDS results. All tested alloys were identified to be of the single bcc phase which was intended for the purpose of studying SSH or SSS in this work. Vickers hardness for all tested alloys, at temperatures ranging from RT to 1000°C, are given in Table 5.1 and plotted in Figure 5.1. Essentially, all alloys showed a three-stage pattern, reminiscent of how the flow stress varies as a function of temperature in RHEAs and other bcc structured materials [50], [156], [157]. Firstly, at low temperatures below 300°C (400°C for HNTT-Fe), the hardness was strongly influenced by the temperature and different substitutional solutes. Normally, the lower the temperature, the higher the hardness, which was also the scenario seen in this case. With 2.5 at. % nominal addition of Mn, Al, Cu, the HNTT base alloy was softened by 20 %, 18.1 %, 13.3 %, respectively, while 2.5 at. % nominal addition of Fe instead hardened HNTT by 5.2 %. Secondly, at intermediate temperatures ranging from 300°C (400°C for HNTT-Fe) to 800°C, the hardness was almost stabilized, and a plateau was seen. Finally, at high temperatures over 800°C, the hardness of all alloys dropped quickly, presumably due to the increasing impact of thermal diffusion-controlled processes. It is noted that at 1000°C the hardness of the HNTT-Fe alloy, with hardness higher than HNTT up to 800°C, was lower than that of HNTT, indicating the loss of SSH at this temperature.

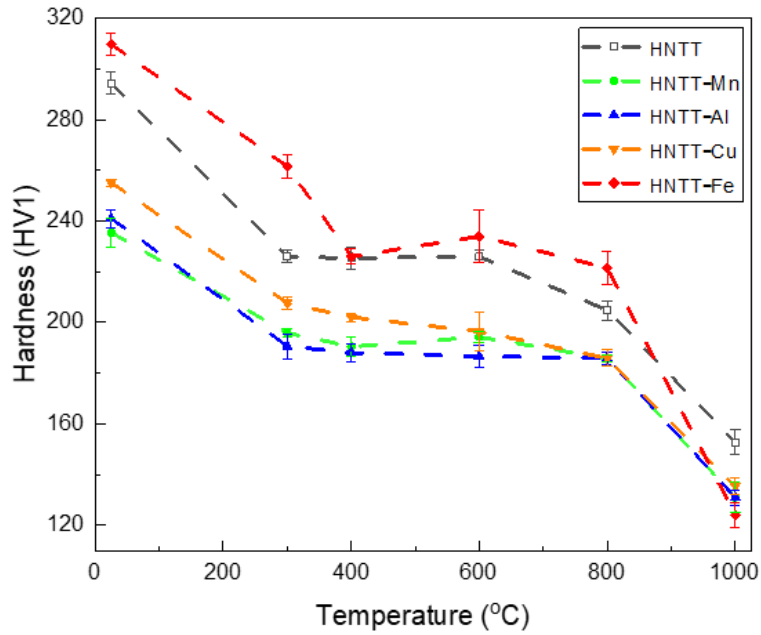


Figure 5.1. Temperature-dependent Vickers hardness for HNTT, HNTT-Mn, HNTT-Al, HNTT-Cu, HNTT-Fe alloys

Table 5.1. Vickers hardness of HNTT, HNTT-Mn, HNTT-Al, HNTT-Cu, HNTT-Fe alloys at various temperatures (in °C)

Alloy ID/Temperature	RT	300	400	600	800	1000
HNTT	294.4±4.5	226.0±2.4	225.4±4.3	226.0±2.5	204.9±3.8	152.7±4.8
HNTT-Mn	235.5±5.8	195.9±1.8	190.5±3.8	194.3±2.2	185.9±1.6	131.0±6.1
HNTT-Al	241.1±3.5	190.7±4.9	188.1±3.7	186.7±4.2	186.0±2.5	130.9±2.9
HNTT-Cu	255.2±1.4	207.7±2.6	202.1±1.7	196.5±7.9	185.9±3.2	135.5±3.3
HNTT-Fe	309.8±4.1	261.6±4.8	226.0±3.1	234.0±10.3	221.6±6.4	124.1±4.9

In summary, minor additions of substitutional elements could cause either solid solution hardening or softening in a $\text{Hf}_{20}\text{Nb}_{31}\text{Ta}_{31}\text{Ti}_{18}$ RHEA, in a wide temperature range. 2.5 at. % nominal addition of Fe led to solid solution hardening due to a kink migration dominated plastic deformation mechanism, while the same nominal content of additions of Mn, Al and Cu caused solid solution softening due to a double-kink nucleation dominated plastic deformation mechanism. A crossover of dominating plastic deformation mechanism from double-kink nucleation to kink migration could be varied by the type and content of solute additions, and the temperature range. On the other hand, for all studied alloys, regardless of the occurrence of solid solution hardening or softening, the hardness variation with temperature showed the same three-stage pattern: a temperature dependent hardness reduction from room temperature to 300°C/400°C, followed by an athermal plateau from 300°C/400°C to 800°C,

influenced mainly by misfits in atomic size and modulus, and finally a quick drop in hardness above 800°C due to the enhanced diffusion-controlled processes.

5.1.2 Minor Mn addition into originally brittle RHEAs: A case for $(\text{TiHfNb})_{85}\text{Mo}_{15}\text{Mn}_{(0.03-2 \text{ at}\%)}$
 Based on experimental results obtained from paper #1, Mn, Al and Cu were identified as effective SSS enabling elements at RT in single-phase bcc structured RHEAs. With an increasing solute concentration of Mn, Al and Cu, the change of Vickers hardness (HV5) of an RT brittle $(\text{TiHfNb})_{85}\text{Mo}_{15}$ alloy was plotted in Figure 5.2. A clear tendency of significant drop of hardness was observed with the minor addition of solutes less than 0.4 at %, particular with Mn. The seemingly slight increase of hardness of the alloy with a nominal 0.1 at % addition of Mn was within the uncertainty range. In this case, Mn as the most promising SSS enabling element was chosen to apply to this RT brittle base alloy, to demonstrate the strategy employing solid solution softening (SSS) at RT and solid solution hardening (SSH) at elevated temperatures, in order to reduce the temperature dependence of yield stress and to achieve a better balance of strength and ductility in single-phase bcc-structured alloys in a wide temperature range.

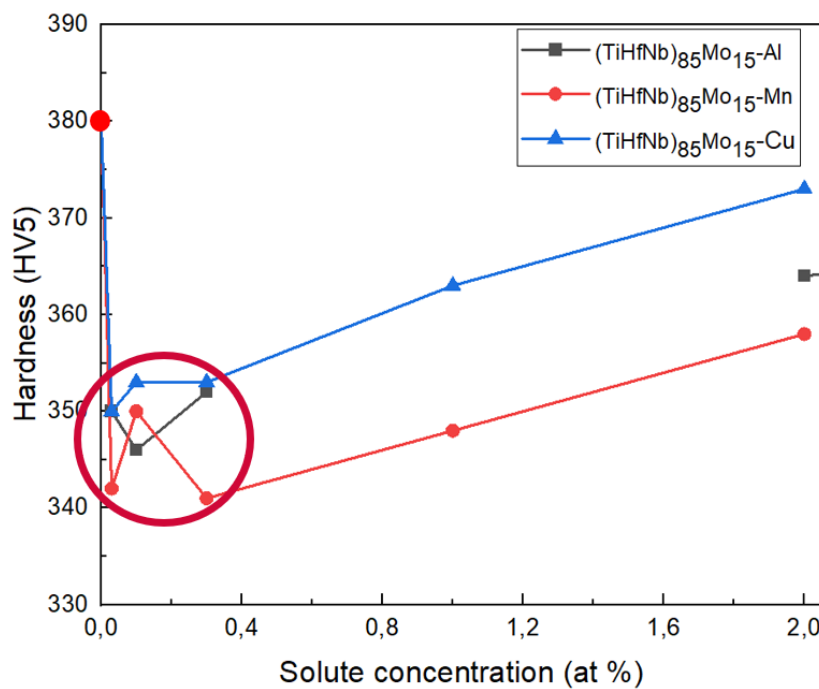


Figure 5.2. Vickers hardness for $(\text{TiHfNb})_{85}\text{Mo}_{15}$ alloys with increasing solute concentrations of Mn, Al and Cu at room temperature

RHEAs with nominal compositions of $(\text{TiHfNb})_{85-x}\text{Mo}_{15}\text{Mn}_x$ ($x=2, 1, 0.3, 0.1, 0.03, 0$, in at%, with alloys denoted as Mn2, Mn1, Mn0.3, Mn0.1, Mn0.03, the base alloy, respectively) were produced by arc melting of high purity (>99.95%) elements at least 5 times to ensure chemical homogeneity followed by drop casting. Dendritic microstructure enriched with Mo and Nb, and inter-dendritic microstructure

enriched with Hf and Ti, were seen in directly cast RHEAs by SEM-BSE and EDS. All tested alloys were identified to be of the single bcc phase. Compressive yield stress from RT to 1000°C for base, Mn2, Mn1, Mn0.3, Mn0.1 and Mn0.03 alloys are summarized in Table 5.2. The temperature dependence of compressive yield stress from RT to 1000°C for all tested alloys are plotted in Figure 5.3.

The yield stress of the base alloy was higher than those alloys with minor Mn additions, thus showing a SSS effect at RT. To be specific, nominal additions of 2%, 1%, 0.3%, 0.1%, 0.03% of Mn softened the base alloy by 2.0%, 4.4%, 9.5%, 6.8%, 6.7%, respectively, in terms of yield stress, which was 5.8%, 8.4%, 10.3%, 7.9%, 10.0% respectively, in terms of Vickers hardness. The softening was most significant at nominal addition of 0.3% Mn. Seen from Figure 5.3 below, at the temperature range from RT to 400°C, the yield stress showed a strong temperature dependence. At the intermediate temperature range, from 400°C to 800°C in this case, the yield stress was almost stabilized. Also, the yield stress of the base alloy was lower than those with minor Mn additions, thus displaying a SSH effect. Taking the yield stresses measured at 600°C as an example, the nominal addition of 2%, 1%, 0.3%, 0.1%, 0.03% of Mn hardened the base alloy by 7.4%, 6.1%, 3.8%, 3.2%, 0.9%, respectively. The hardening level decreased with decreasing Mn content. At high temperatures, 1000°C in this case, the yield stress experienced a quick drop regardless of the amount of Mn additions, due to a typical softening mechanism associated with the activation of thermal diffusional processes and the low melting point of Mn thus its fast diffusion. The plastic deformation at this high temperature range is more studied for time-dependent mechanical properties such as creep and fatigue, which is beyond the scope of the current work.

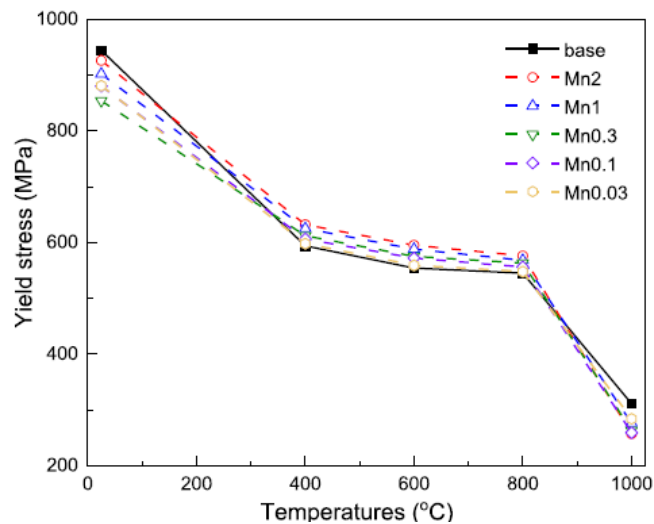


Figure 5.3. Temperature dependence of compressive yield stress across all studied alloys from RT to 1000°C

Table 5.2. Compression yield stress (σ_y), and peak stress (σ_p) of the studied alloys given in the form of σ_y/σ_p , at the temperature range from RT to 1000°C.

Alloys /Temperatures(°C)	Base	Mn2	Mn1	Mn0.3	Mn0.1	Mn0.03
RT ¹	944/-	926/-	902/-	854/-	880/-	881/-
400°C ²	594/1101	632/1117	625/1099	612/1087	606/1095	598/1099
600°C ²	554/1015	595/1060	588/1076	575/1032	572/1047	559/1032
800°C ²	545/745	576/767	568/770	563/776	556/779	548/749
1000°C ²	311/328	257/288	276/305	263/303	259/296	254/295

1: tested using the universal compressive machine; 2: tested using the Gleeble system.

In summary, better balanced strength from low temperatures to intermediate temperatures in a (TiHfNb)₈₅Mo₁₅ RHEA was experimentally achieved here by less than 2 at. % nominal substitutional additions of Mn, combining strategies of SSS at low temperatures and SSH at intermediate temperatures. The yield stress of all studied alloys showed a three-stage pattern: a temperature dependent state at low temperatures governed by SSS, an athermal stage at intermediate temperatures controlled by SSH, and another temperature dependent stage at high temperatures influenced by enhanced thermal diffusional processes. The alloy with 0.3 at. % Mn addition showed the largest softening effect by 9.5% at RT. The same alloy also exhibited the lowest temperature dependence descriptor $\lambda_{\sigma-T}$ among all studied alloys, indicating the lowest temperature dependence of yield stress before reaching the high temperature range. Overall, SSS at low temperatures holds the potential to induce non-zero tensile ductility for those RHEAs with decent HT strength, which would alleviate the manufacturing and processing concerns, while a simultaneous improvement of yield stress at intermediate temperatures by SSH is important for their applications at elevated temperatures.

5.2 Trade-off between oxidation resistance and ductility at RT: Alloying Nb alloys with Al

Oxidation resistance enabling alloys' performance at HT was commonly jeopardized by the priorities given to the strength at HT and ductility at RT during the development of ultrahigh temperature refractory alloys. Here, the effect of Al addition on the oxidation behavior of Nb-based refractory alloys was investigated. Nb-based alloys with nominal compositions of Nb-20Hf-5.5W and Nb_{79.5-x}Hf₁₅W_{5.5}Al_x (x=4, 8, 12, all in at %, with alloys denoted as WC3009, 4Al, 8Al, 12Al afterwards) were produced by arc melting of high purity (>99.95%) elements at least 5 times to ensure chemical homogeneity followed by drop casting. Dendritic and inter-dendritic features, with segregation of Nb and W having high T_m in the dendritic region, while Hf and Al having relatively low T_m in the inter-dendritic region were observed. WC3009 has the lowest RT hardness value of 278 (HV5), and the hardness increases with the increasing of Al content, up to 423 (HV5) in the 12Al alloy. WC3009, 4Al

and 8Al were identified to be of the single bcc phase while ordered b2 phase was detected in the 12Al alloy. Discontinuous oxidation experiments of the produced alloys were carried out in a ceramic tube furnace pre-heated to 800°C, 1000°C and 1200°C for 1h, 8h and 24h in static laboratory air. The specimens were in the form of cubic blocks with approximate dimensions of 4 × 4 × 4 mm³ with dimensions of crucible 20 × 20 × 20 mm³. Pesting phenomenon with different degrees appeared in most cases except for the specimens oxidized at 800 °C for 1 h, see Figure 5.5 below.

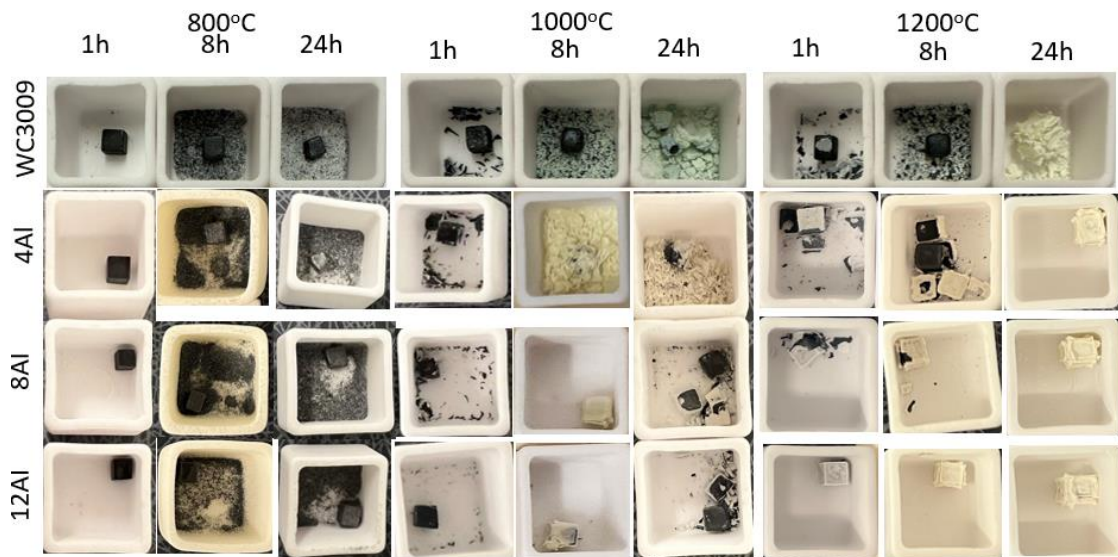


Figure 5.5. Optical graphs of the oxidized specimens at 800°C, 1000°C and 1200°C after 1h, 8h and 24h of oxidation exposure individually, with the crucible dimensions of 20 × 20 × 20 mm³.

The oxidation kinetics was also quantified, following the growth rate law as given below, with results shown in Figure 5.6.

$$\frac{\Delta m}{SA} = k_p * t^n$$

Where Δm is the mass change in mg, SA is the initial sample surface area and $\frac{\Delta m}{SA}$ is the specific mass change normalized by the initial surface area with the unit of mg/cm², k is the rate constant, t is the oxidation time, n is the time exponent. The oxidation behavior of the alloys experienced a transition from linear mode at 800°C, to semi-parabolic at 1000°C, and to parabolic at 1200°C. At 800°C, the interfacial reaction controlled the oxidation process, while the oxidation was controlled by the diffusion mechanism partially at 1000°C and fully at 1200°C. This transition of oxidation behavior indicates the beneficial effect of Al alloying to protect the alloys from quick failure.

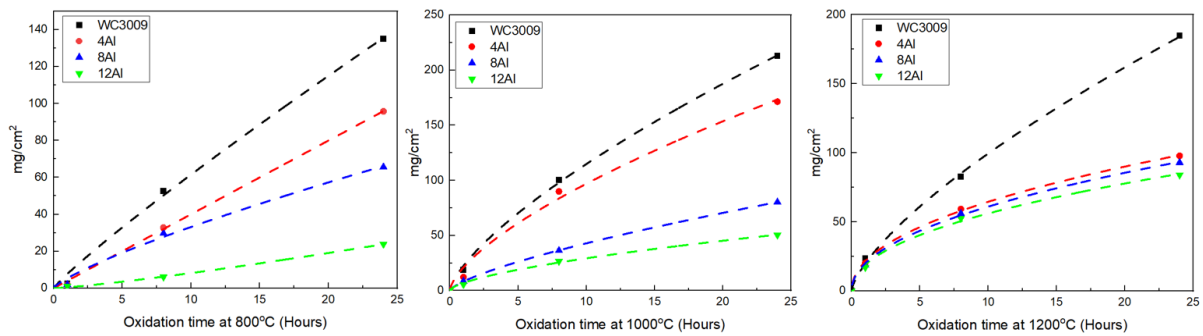


Figure 5.6. Oxidation kinetics curves of the Nb-based refractory alloys at 800°C, 1000°C, and 1200 °C

In summary, the oxidation resistance of RT ductile Nb-based alloys was greatly improved by Al alloying. A transition of oxidation behavior from linear at 800°C to semi-parabolic at 1000°C to parabolic at 1200°C was characterized, indicating a controlling mechanism from interfacial reaction to diffusion. Although dense and protective Al_2O_3 layers did not form, Al alloying was confirmed to be an effective way to contribute to the operation of Nb-based refractory alloys at HT.

5.3 Trade-off among ductility at RT, strength at HT, and oxidation resistance: Alloying Nb alloys with Hf, W and Ti

When it comes to alloys aiming for use at HT as structural materials, meeting the property requirements such as ductility at RT, strength at HT, and oxidation resistance is always needed. However, the almost intrinsic conflict on the material requirements to achieve these three properties commonly stands in the way for the materials development. Thus, how to settle the trade-off and enable these three properties in one material has been a long-standing challenge. Given the fact that the melting point of Ni-based superalloys has limited their applications and driven by the need to close the efficiency gap of turbine engines working above 1200°C due to auxiliary cooling, refractory alloys with high melting points have received much attention over the years. Particularly, Nb-based alloys stand out from existing refractory metals, with merits like low density of 8.57 g/cm^3 , high melting point of 2477°C and low ductile-brittle transition temperature (DBTT) between -100°C to -195°C [45],[158]. Therefore, Nb-based refractory alloys were intensively studied and other refractory elements like Hf and W were widely used to enhance their mechanical properties. Here, two commercial Nb-based alloys, ductile C103 (Nb-5.5Hf-2Ti) and high-strength WC3009 (Nb-20Hf-5.5W) were modified by alloying with Hf, W and Ti, hoping to achieve a better balance between mechanical properties and oxidation resistance in Nb-based refractory alloys. Four novel Nb-based alloys, Nb-15Hf-5.5Ti, Nb-12.75Hf-1Ti-2.75W, Nb-15Hf-10Ti-6.5W, Nb-20Hf-15Ti-9.5W (compositions all given in at. % unless indicated otherwise) were developed and produced by arc melting followed with drop casting into bars with dimensions of $10 \times 10 \times 40 \text{ mm}^3$. Elemental mappings of these alloys showed typical dendritic and inter dendritic features, with segregation of Nb and W having high T_m in the

dendritic region, while Hf and Ti having relatively low T_m in the inter-dendritic region. XRD results confirmed the single-phase bcc crystal structure in all alloys studied here. Vickers hardness (HV5) in general increased with total solute concentrations. Compressive test results at RT were consistent with the Vickers hardness results in that the yield stress at RT was generally proportional to the total solute concentrations, reflecting the solid solution hardening effect. Compressive test results at 1200°C showed a general softening after yielding, suggesting that dynamic recovery and recrystallization dominated over work hardening at this temperature. Considering the ratio of yield stress at 1200°C over that at RT, which indicates the retainability of strength at elevated temperatures, the strength at HT gradually degraded with the increasing of Ti content, which was mainly employed to improve the oxidation resistance.

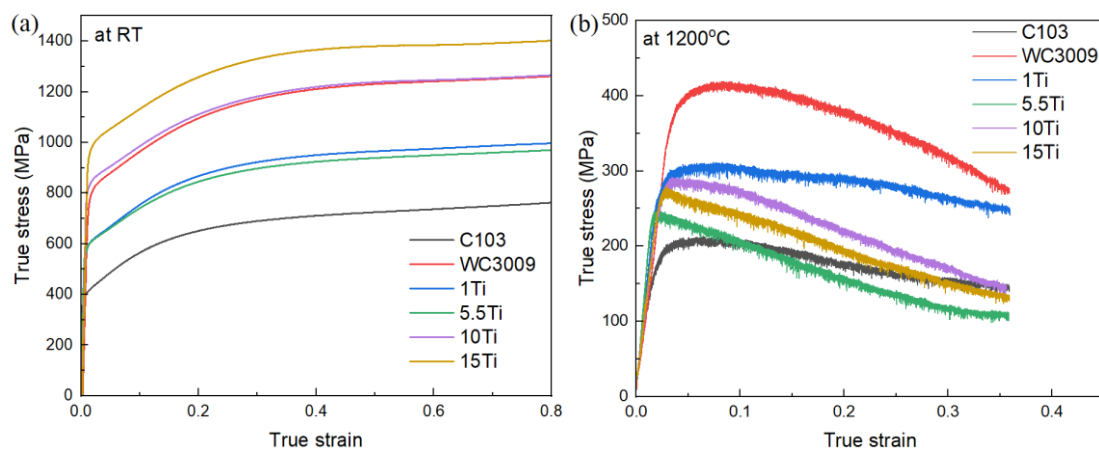


Figure 5.7. Compressive strain-stress curves for the Nb-based refractory alloys at (a) RT and (b) 1200°C

Table 5.3. Yield strength at RT and 1200°C and the ratio between these two, for the Nb-based refractory alloys

Alloy ID	C103	WC3009	1Ti	5.5Ti	10Ti	15Ti
σ_y^{RT}	367	762	566	566	811	949
$\sigma_y^{1200^\circ C}$	170 ± 9	343 ± 11	262 ± 5	228 ± 6	259 ± 9	254 ± 17
$\sigma_y^{1200^\circ C}/\sigma_y^{RT}$	0.46	0.45	0.46	0.40	0.32	0.27

Discontinuous oxidation experiments of the newly developed Nb-based alloys were carried out in a high temperature ceramic tube furnace pre-heated to 800°C, 1000°C and 1200°C for 1h, 8h and 24h in static laboratory air. Optical images of alloys studied after oxidation at 800°C, 1000°C and 1200°C for 1h, 8h and 24h are shown in Figure 5.8 below. It is clear to notice a varying degree of pesting phenomenon with spalling-off appearing in most cases, and pesting generally gets worse with increased exposure time and temperatures. Meanwhile, the beneficial effect from high Ti addition on the improved oxidation resistance is obvious, seen in the 10Ti and 15Ti alloys.

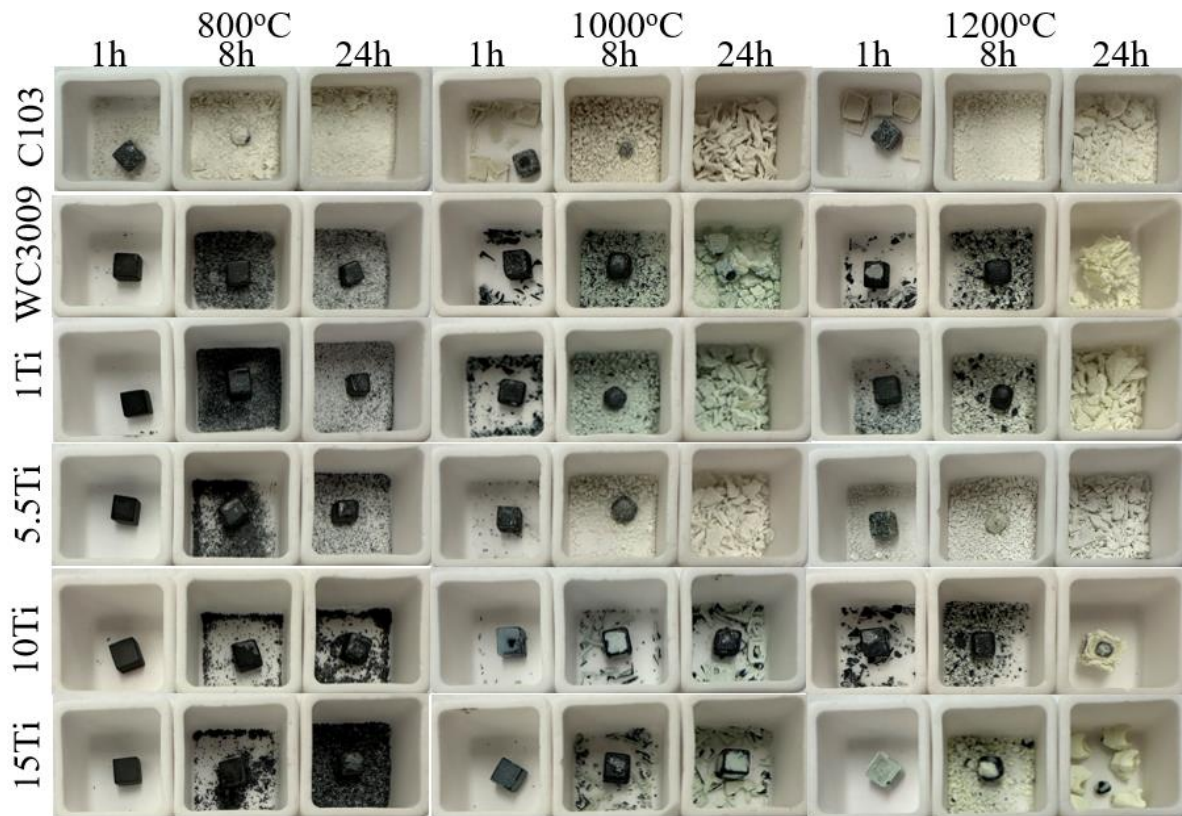


Figure 5.8. Optical images of the specimens of the Nb-based refractory alloys at 800°C, 1000°C and 1200°C after 1h, 8h and 24h oxidation exposure, with the crucible dimensions of 20 × 20 × 20 mm³

The oxidation kinetics curves of specimens oxidized at 800°C, 1000°C and 1000°C are shown in Figure 5.9 below. Basically, C103 has the highest weight gain, 10Ti and 15Ti have the lowest weight gain, while 1Ti, 5.5Ti and WC3009 have the intermediate weight gain, which is consistent with the observation from the optical images shown in Figure 5.8. With the increasing Ti addition up to 10 at% and 15 at%, the efficient reduction on the oxidation weight gain is observed, and the 10 at% addition is optimal.

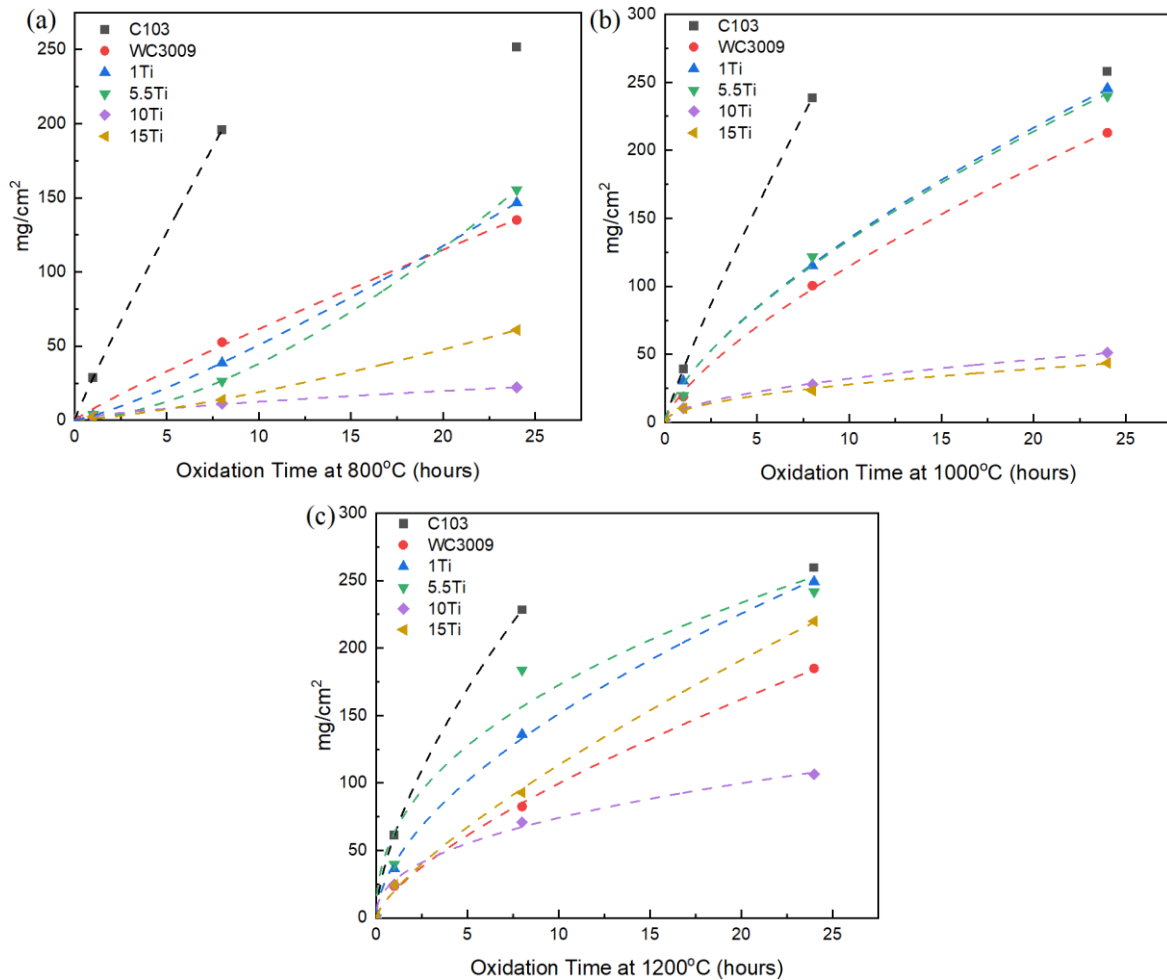


Figure 5.9. Oxidation kinetics curves of the Nb-based refractory alloys at (a) 800°C, (b) 1000°C and (c) 1200°C

In summary, microstructures, mechanical properties and oxidation behavior of four newly developed Nb-based alloys, benchmarked to the commercial C103 and WC3009 alloys, were reported. Dendrite and inter-dendrite features with single bcc structure were observed in all alloys studied here. Compressive test results at RT are consistent with the Vickers hardness results, showing the positive correlation between the solute concentrations and the compressive yield stress/hardness. Yield stresses at 1200°C reveal a significant weakening effect from heavy Ti additions, which cannot be compensated by intentional W addition. Alloys with less Ti additions normally have a high retainability of yield stress to elevated temperatures. Nevertheless, the beneficial effect of Ti addition to effectively reducing the oxidation weight gain with enhancing the oxidation resistance performance was confirmed.

Overall, although 10-15at.% of Ti addition lowers the high-temperature strength at 1200°C, a reasonably high yield strength of 259MPa and 254MPa, respectively, are achieved in the 10Ti and 15Ti alloys. Meanwhile, the oxidation resistance of the 10Ti and 15Ti alloys is much improved compared to that of C103 and WC3009. Therefore, it seems rather promising to achieve balanced mechanical

properties and oxidation resistance in Nb-based refractory alloys by fine-tuning the type and content of alloying elements, for example Hf, W and Ti as studied in this work.

5.4 Trade-off between ductility and strength at RT: An unexpected effect of oxygen

In this thesis work, we mainly dealt with the trade-off between RT ductility and HT strength. Indeed, the trade-off also exists for strength and ductility at RT, as is commonly seen in other metallic materials. Particularly, when our target materials are single-phase bcc-structured RHEAs, where the lattice distortion is generally high leading to significant solid solution strengthening, the trade-off between strength and ductility at RT is commonly seen. In section 3.2, strategies to balance strength and ductility at RT including VEC engineering, TRIP, and solid solution softening were introduced. We also identified another unexpected way to improve ductility of otherwise brittle RHEAs, by intentionally introducing oxygen during the arc melting and casting process. This observation is against the common knowledge that oxygen contamination is detrimental to ductility in refractory metals and alloys. We showed this strategy in a $(\text{VNb})_{70}\text{Ti}_{15}\text{Mo}_{10}\text{Hf}_5$ RHEA, where importantly 5 at% addition of reactive element Hf, as an oxygen absorber, was added into the otherwise Hf-free Vb-Nb-Ti-Mo RHEA. RHEAs with nominal compositions of $(\text{VNb})_{70}\text{Ti}_{15}\text{Mo}_{10}\text{Hf}_5$ (all in at %) were produced by arc melting of high purity (>99.95%) elements at least 5 times to ensure chemical homogeneity followed by drop casting into bars with dimensions of $10 \times 10 \times 40 \text{ mm}^3$. The alloy melted under high vacuum condition of $4.0 \times 10^{-5} \text{ mbar}$ is referred to as HV, and the alloy arc melted under an intentional low vacuum condition ($6.0 \times 10^{-3} \text{ mbar}$) is referred as LV. Dendrites enriched with Nb and Mo and inter-dendrites enriched with V, Ti and Hf structures were observed, due to their different melting points. Single-phase bcc structure was confirmed by XRD in all tested alloys. While there is not much difference between HV and LV on the microstructure, RT hardness and crystal structure, the LV alloy surprisingly showed non-zero tensile ductility when the HV alloy failed before yielding and showed a typical brittle behavior (Figure 5.10).

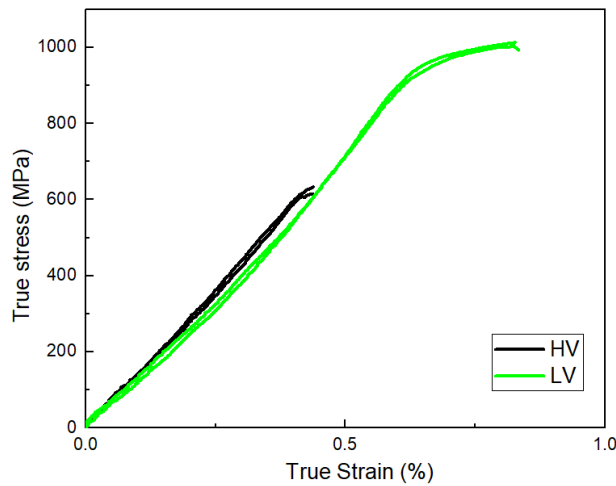


Figure 5.10. RT True strain-stress curves of HV and LV (VNi)₇₀Ti₁₅Mo₁₀Hf₅ alloys

Comparing the fractography between the LV and HV alloys, the former specimen exhibited more adhesive grain boundaries and seemingly interrupted cleavage fracture, see Figure 5.11 below. We have not been able to identify the exact mechanism behind this interesting and unexpected observation, but we did show this phenomenon is reproducible in some other RHEA systems, including the (TiHfNb)₈₅Mo₁₅ RHEA, with RT Vickers hardness (HV5) lowered to 350±3.5 from 380±4 after melting under low vacuum condition (6.0*10⁻³ mbar). We suspect that the improved ductility, even marginal, was enabled by the existence of ultrafine and loosely distributed oxides (possibly HfO₂ in the case of (VNi)₇₀Ti₁₅Mo₁₀Hf₅) that slow down the crack propagation. We did not include a manuscript on this observation in this thesis, since a mechanistic interpretation is not available yet, but we expect that this study demonstrates a new way to improve the ductility of brittle RHEAs via deliberately introducing oxygen during melting and casting.

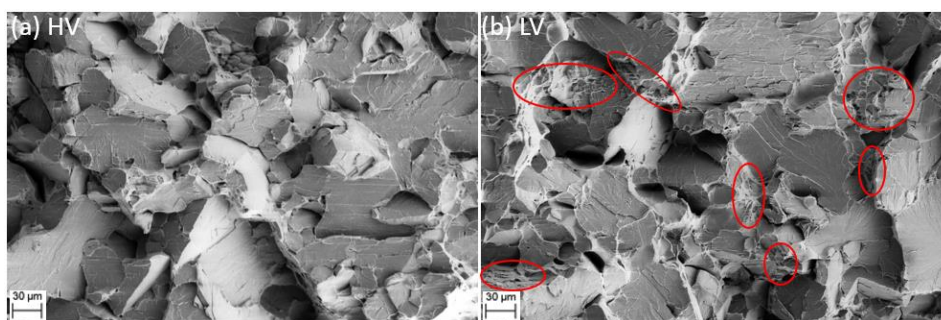


Figure 5.11. SEM images of fractography from tensile specimens of (a) HV and (b) LV alloys

6 Conclusions and future prospects

The core idea of this thesis is to develop strategies to address trade-offs among three targets, strength at high temperatures (Target No.1), ductility at room temperature (Target No.2) and oxidation resistance (Target No.3), aiming to achieve single-phase bcc-structured refractory alloys with balanced mechanical properties and oxidation resistance. Our results showed some promises to develop high-performance refractory alloys, and the main conclusions are summarized as follows:

a) Trade-off of ductility at RT and strength at HT: Solid solution softening (SSS) and/or solid solution hardening (SSH)

- The Vicker hardness (HV1) for $\text{Hf}_{20}\text{Nb}_{29.75}\text{Ta}_{29.75}\text{Ti}_{18}\text{-X}_{2.5}$ (in at%, X=Mn, Al, Cu, Fe) alloys showed a three-stage pattern in the temperature range of from 25°C to 1000°C: from 25°C to 400°C, a temperature dependent hardness reduction; from 400°C to 800°C, an athermal plateau; above 800°C, the hardness dropped quickly.
- The 2.5 at% nominal addition of Mn, Al and Cu softened the RT ductile base alloy $\text{Hf}_{20}\text{Nb}_{31}\text{Ta}_{31}\text{Ti}_{18}$, while the same amount of Fe hardened the base alloy, from RT to 800°C.
- The compressive yield stress of $(\text{TiHfNb})_{85-x}\text{Mo}_{15}\text{Mn}_x$ (in at%, $x=0.03\sim 2$) alloys also showed a three-stage pattern from 25°C to 1000°C: from 25°C to 400°C, a temperature dependent stresses; from 400°C to 800°C, an athermal plateau; above 800°C, a quick drop of compressive stress.
- The addition of less than 2at. % nominal Mn rendered the base alloy $(\text{HfNbTi})_{85}\text{Mo}_{15}$ a reduced yield stress at RT, displaying the softening effect, together with a slightly increased yield stress from 400°C to 800°C, thus showing the hardening effect, achieving a simultaneous softening at RT and hardening at HT.

b) Trade-off between oxidation resistance and ductility at RT: Alloying Nb alloys with Al

- The RT Vickers hardness of the benchmark WC3009 and $\text{Nb}_{79.5-x}\text{Hf}_{15}\text{W}_{5.5}\text{Al}_x$ ($x=4, 8, 12$, at%) alloys increase with the increasing Al content, from 278 (HV5) of WC3009 up to 423 (HV5) of the 12Al alloy.
- Oxidation resistance of these RT ductile Nb-based alloys was greatly improved by Al alloying.
- A transition of oxidation behavior from linear at 800°C to semi-parabolic at 1000°C to parabolic at 1200°C was characterized, indicating a controlling mechanism from interfacial reaction to diffusion.
- Although dense and protective Al_2O_3 layers did not form, the formation of Al containing complex oxides was beneficial to protect the alloys from quick failure.

c) Trade-off among ductility at RT, strength at HT, and oxidation resistance: Alloying Nb alloys with Hf, W and Ti

- Compressive test results at RT are consistent with the Vickers hardness results, showing the positive correlation between the solute concentrations (Hf, Ti and W) and the compressive yield stress/hardness.
- Heavy Ti additions lead to a significant weakening effect on the yield strength at 1200°C, which cannot be compensated by intentional W addition. Nevertheless, a reasonably high yield strength of 259MPa and 254MPa, respectively, are achieved in the 10Ti and 15Ti alloys, compared to 343MPa for the benchmark WC3009 alloy.
- A beneficial effect of Ti addition to effectively reducing the oxidation weight gain with enhancing the oxidation resistance performance was confirmed.
- It seems rather promising to achieve balanced mechanical properties and oxidation resistance in Nb-based refractory alloys by fine-tuning the type and content of alloying elements, for example Hf, W and Ti as studied in this work.

d) Trade-off between ductility and strength at RT: An unexpected effect of oxygen

- Non-zero tensile ductility was surprisingly achieved in the $(\text{VNb})_{70}\text{Ti}_{15}\text{Mo}_{10}\text{Hf}_5$ RHEA melted under low vacuum condition (6.0×10^{-3} mbar), in comparison to the same alloy melted under high vacuum condition (4.0×10^{-5} mbar), which however showed a brittle behavior.
- Improved ductility, even marginal, was possibly enabled by the existence of ultrafine and loosely distributed oxides (possibly HfO_2) that slow down the crack propagation.
- This observation was not concluded in this thesis with a mechanistic interpretation, but it demonstrates a possible new way to improve the ductility of brittle RHEAs via deliberately introducing oxygen during melting and casting.

Apparently, there is still a long way to go before refractory alloys can be applied as high-temperature structural materials in practice. Resolving their RT brittleness without compromising the strength at HT and how to integrate oxidation resistance into these alloys, are still challenging topics for the research community. Future efforts shall be dedicated to these following aspects:

- Mechanisms behind the SSS effect existing in refractory alloys at RT need to be revealed at both theoretical and experimental level, and consequently ways shall be established to induce non-zero tensile ductility for those refractory alloys with decent HT strength, utilizing the SSS effect.

- Powder metallurgy route could be a better option than casting to introduce Mn to refractory alloys, due to its boiling point being close to or even lower than the melting points of those refractory elements; also, the powder metallurgy route could be used to engineer the size and dispersion of the secondary phases (for example, carbides or nitrides), to strengthen refractory alloys without compromising their ductility.
- A quantitative relationship between the oxygen content and the mechanical behavior, particularly the RT ductility, of Ti group elements (Ti, Zr, Hf) containing refractory alloys needs to be established.
- A better understanding of the oxidation behavior for Nb-based refractory alloys is needed, and information on the oxidation sequence and the distribution of oxidation products relative to the base RHEA is still lacking.
- Surface coating could be an alternative way to bypass the trade-off between mechanical properties and oxidation resistance of refractory alloys. The formation of, for example, protective silicides, on the surface of those RHEAs with proven RT ductility and decent HT strength, deserves to be tested.

7 Acknowledgements

The work presented in this thesis was carried out under the financial support from the Swedish Research Council (grant number 2019-03559), which is greatly acknowledged. I would like also thank the financial support from the Axel Hultgrens Fund, and the JSPS (Japan Society for the Promotion of Science) Summer Program.

The major gratitude goes to my supervisor Sheng Guo, who has been supporting my research throughout the work. I also would like to express my gratitude to my assistant supervisor, Dr. Huahai Mao, who helped us with thermodynamics calculations whenever we needed him. Great thanks to my examiner Uta Klement as well, for her long-term support.

I am so grateful for the help I got from Yiming Yao. She guided me and assisted me so professionally for using various metallography and characterization equipment, step by step, including but certainly not limited to microscopy. Sincere appreciation also goes to Eric Tam and Fang Liu.

Thanks to my friends and colleagues at the Department of Industrial and Materials Science, Chalmers, for their support and creating a friendly working environment.

In addition to collaborators that are acknowledged in the published papers and manuscripts, I would also like to thank Prof. Yoko-Yamabe-Mitarai at University of Tokyo and Prof. Nobuhiro Tsuji at Kyoto University for the useful suggestions and discussions.

Deepest gratitude to my parents, my elder sister for their endless love and unwavering support.

Xiaolong Li

Gothenburg, 2025

8 References

- [1] P. John H, 'The hotter the engine, the better', Nov. 20, 2009. doi: 10.1126/science.1179117.
- [2] R. L. Fleischer, 'High-Temperature, High-Strength Materials - An Overview', *JOM*, vol. 37, no. 12, pp. 16–20, Dec. 1985, doi: 10.1007/BF03259961.
- [3] J. A. Lemberg and R. O. Ritchie, 'Mo-Si-B alloys for ultrahigh-temperature structural applications', *Advanced Materials*, vol. 24, no. 26, pp. 3445–3480, Jul. 2012, doi: 10.1002/adma.201200764.
- [4] R. A. Perkins and G. H. Meier, 'The oxidation behavior and protection of niobium', *JOM*, vol. 42, no. 8, pp. 17–21, 1990, doi: 10.1007/BF03221046.
- [5] M. C. Gao, J.-W. Yeh, P. K. Liaw, and Y. Zhang, 'High-Entropy Alloys: *fundamentals and applications*', Springer, 2016.
- [6] Y. F. Ye, Q. Wang, J. Lu, C. T. Liu, and Y. Yang, 'High-entropy alloy: challenges and prospects', *Materials Today*, vol. 19, no. 6, pp. 349–362, Jul. 2016, doi: 10.1016/j.mattod.2015.11.026.
- [7] J. W. Yeh *et al.*, 'Nanostructured High-Entropy Alloys with Multiple Principal Elements: Novel Alloy Design Concepts and Outcomes', *Adv Eng Mater*, vol. 6, no. 5, pp. 299–303, May 2004, doi: 10.1002/adem.200300567.
- [8] Y. Zhang *et al.*, 'Microstructures and properties of high-entropy alloys', *Prog Mater Sci*, vol. 61, pp. 1–93, Apr. 2014, doi: 10.1016/j.pmatsci.2013.10.001.
- [9] D. B. Miracle and O. N. Senkov, 'A critical review of high entropy alloys and related concepts', *Acta Mater*, vol. 122, pp. 448–511, Jan. 2017, doi: 10.1016/j.actamat.2016.08.081.
- [10] C. Ng, S. Guo, J. Luan, S. Shi, and C. T. Liu, 'Entropy-driven phase stability and slow diffusion kinetics in an Al_{0.5}CoCrCuFeNi high entropy alloy', *Intermetallics*, vol. 31, pp. 165–172, Dec. 2012, doi: 10.1016/j.intermet.2012.07.001.
- [11] S. Guo and C. T. Liu, 'Phase stability in high entropy alloys: Formation of solid-solution phase or amorphous phase', *Progress in Natural Science: Materials International*, vol. 21, no. 6, pp. 433–446, Dec. 2011, doi: 10.1016/S1002-0071(12)60080-X.
- [12] S. Guo, Q. Hu, C. Ng, and C. T. Liu, 'More than entropy in high-entropy alloys: Forming solid solutions or amorphous phase', *Intermetallics*, vol. 41, pp. 96–103, 2013, doi: 10.1016/j.intermet.2013.05.002.
- [13] Y. Zhang *et al.*, 'Microstructures and properties of high-entropy alloys', *Prog Mater Sci*, vol. 61, pp. 1–93, Apr. 2014, doi: 10.1016/j.pmatsci.2013.10.001.
- [14] B. Cantor, I. T. H. Chang, P. Knight, and A. J. B. Vincent, 'Microstructural development in equiatomic multicomponent alloys', *Materials Science and Engineering: A*, vol. 375–377, no. 1-2 SPEC. ISS., pp. 213–218, Jul. 2004, doi: 10.1016/j.msea.2003.10.257.
- [15] O. N. Senkov, G. B. Wilks, J. M. Scott, and D. B. Miracle, 'Mechanical properties of Nb₂₅Mo₂₅Ta₂₅W₂₅ and V₂₀Nb₂₀Mo₂₀Ta₂₀W₂₀ refractory high entropy alloys',

- Intermetallics*, vol. 19, no. 5, pp. 698–706, May 2011, doi: 10.1016/j.intermet.2011.01.004.
- [16] O. N. Senkov, J. M. Scott, S. V. Senkova, D. B. Miracle, and C. F. Woodward, 'Microstructure and room temperature properties of a high-entropy TaNbHfZrTi alloy', *J Alloys Compd*, vol. 509, no. 20, pp. 6043–6048, May 2011, doi: 10.1016/j.jallcom.2011.02.171.
- [17] M. C. Gao, B. Zhang, S. M. Guo, J. W. Qiao, and J. A. Hawk, 'High-Entropy Alloys in Hexagonal Close-Packed Structure', *Metall Mater Trans A Phys Metall Mater Sci*, vol. 47, no. 7, pp. 3322–3332, Jul. 2016, doi: 10.1007/s11661-015-3091-1.
- [18] O. N. Senkov, G. B. Wilks, D. B. Miracle, C. P. Chuang, and P. K. Liaw, 'Refractory high-entropy alloys', *Intermetallics*, vol. 18, no. 9, pp. 1758–1765, Sep. 2010, doi: 10.1016/j.intermet.2010.05.014.
- [19] D. B. Miracle and O. N. Senkov, 'A critical review of high entropy alloys and related concepts', *Acta Mater*, vol. 122, pp. 448–511, Jan. 2017, doi: 10.1016/j.actamat.2016.08.081.
- [20] F. G. Coury, M. Kaufman, and A. J. Clarke, 'Solid-solution strengthening in refractory high entropy alloys', *Acta Mater*, vol. 175, pp. 66–81, Aug. 2019, doi: 10.1016/j.actamat.2019.06.006.
- [21] R. Feng *et al.*, 'Superior High-Temperature Strength in a Supersaturated Refractory High-Entropy Alloy', *Advanced Materials*, 2021, doi: 10.1002/adma.202102401.
- [22] O. N. Senkov, T. I. Daboiku, T. M. Butler, M. S. Titus, N. R. Philips, and E. J. Payton, 'High-temperature mechanical properties and oxidation behavior of Hf-27Ta and Hf-21Ta-21X (X is Nb, Mo or W) alloys', *Int J Refract Metals Hard Mater*, vol. 96, Apr. 2021, doi: 10.1016/j.ijrmhm.2020.105467.
- [23] B. Kang, T. Kong, H. J. Ryu, and S. H. Hong, 'Superior mechanical properties and strengthening mechanisms of lightweight Al_xCrNbVMo refractory high-entropy alloys (x = 0, 0.5, 1.0) fabricated by the powder metallurgy process', *J Mater Sci Technol*, vol. 69, pp. 32–41, Apr. 2021, doi: 10.1016/j.jmst.2020.07.012.
- [24] S. Sheikh, S. Shafeie, and Q. Hu, 'Alloy design for intrinsically ductile refractory high-entropy alloys', *J. Appl. Phys*, vol. 120, p. 164902, 2016, doi: 10.1063/1.4966659.
- [25] S. Guo, C. Ng, J. Lu, and C. T. Liu, 'Effect of valence electron concentration on stability of fcc or bcc phase in high entropy alloys', *J Appl Phys*, vol. 109, no. 10, p. 103505, May 2011, doi: 10.1063/1.3587228.
- [26] H. Huang *et al.*, 'Phase-Transformation Ductilization of Brittle High-Entropy Alloys via Metastability Engineering', *Adv. Mater*, vol. 29, p. 1701678, 2017, doi: 10.1002/adma.201701678.
- [27] L. Liliensten *et al.*, 'Design and tensile properties of a bcc Ti-rich high-entropy alloy with transformation-induced plasticity', *Mater Res Lett*, vol. 5, no. 2, pp. 110–116, Mar. 2017, doi: 10.1080/21663831.2016.1221861.

- [28] B. Gorr *et al.*, 'High-Temperature Oxidation Behavior of Refractory High-Entropy Alloys: Effect of Alloy Composition', *Oxidation of Metals*, vol. 88, no. 3–4, pp. 339–349, Oct. 2017, doi: 10.1007/s11085-016-9696-y.
- [29] F. Müller *et al.*, 'On the oxidation mechanism of refractory high entropy alloys', *Corros Sci*, vol. 159, p. 108161, Oct. 2019, doi: 10.1016/j.corsci.2019.108161.
- [30] B. Gorr, S. Schellert, F. Müller, H.-J. Christ, A. Kauffmann, and M. Heilmaier, 'Current Status of Research on the Oxidation Behavior of Refractory High Entropy Alloys', 2021, doi: 10.1002/adem.202001047.
- [31] S. Suzuki, H. Matsui, and H. Kimura, 'The effect of heat treatment on the grain boundary fracture of recrystallized molybdenum', *Materials Science and Engineering*, vol. 47, no. 3, pp. 209–216, Mar. 1981, doi: 10.1016/0025-5416(81)90047-1.
- [32] J. Wadsworth, C. M. Packer, P. M. Chewey, and W. C. Coons, 'A microstructural investigation of the origin of brittle behavior in the transverse direction in Mo-based alloy bars', *Metallurgical Transactions A 1984 15:9*, vol. 15, no. 9, pp. 1741–1752, Sep. 1984, doi: 10.1007/BF02666357.
- [33] J. Wadsworth, T. G. Nieh, and J. J. Stephens, 'Recent advances in aerospace refractory metal alloys', vol. 33, no. 1, pp. 131–150, Jan. 2013, doi: 10.1179/imr.1988.33.1.131.
- [34] V. V. Satya Prasad, R. G. Baligidad, and A. A. Gokhale, 'Niobium and Other High Temperature Refractory Metals for Aerospace Applications', pp. 267–288, 2017, doi: 10.1007/978-981-10-2134-3_12.
- [35] O. Senkov, S. Gorsse, D. Miracle, S. Rao, T. B.-M. & Design, and undefined 2024, 'Correlations to improve high-temperature strength and room temperature ductility of refractory complex concentrated alloys', *Materials & Design*, vol. 239, p.112762, 2024, doi: 10.1016/j.matdes.2024.112762.
- [36] O. N. Senkov, S. I. Rao, T. M. Butler, and K. J. Chaput, 'Ductile Nb alloys with reduced density and cost', *J Alloys Compd*, vol. 808, p. 151685, Nov. 2019, doi: 10.1016/j.jallcom.2019.151685.
- [37] O. N. Senkov, S. I. Rao, T. M. Butler, T. I. Daboiku, and K. J. Chaput, 'Microstructure and properties of Nb-Mo-Zr based refractory alloys', *Int J Refract Metals Hard Mater*, vol. 92, p. 105321, Nov. 2020, doi: 10.1016/j.ijrmhm.2020.105321.
- [38] O. N. Senkov, S. I. Rao, D. B. Miracle, A. E. Mann, and A. Yousefiani, 'Effect of Re and Al additions on the microstructure and mechanical properties of Nb-18Ti-12W alloy', *Materials Science and Engineering: A*, vol. 870, Apr. 2023, doi: 10.1016/j.msea.2023.144870.
- [39] O. N. Senkov, S. I. Rao, T. M. Butler, T. I. Daboiku, and K. J. Chaput, 'Effect of Fe additions on the microstructure and properties of Nb-Mo-Ti alloys', *Int J Refract Metals Hard Mater*, vol. 89, p. 105221, Jun. 2020, doi: 10.1016/j.ijrmhm.2020.105221.
- [40] O. N. Senkov, S. I. Rao, G. H. Balbus, and B. W. J. McArthur, 'Exceptional high-temperature strength of a Mo-11%Hf binary alloy', *Materials Science and Engineering: A*, vol. 922, Feb. 2025, doi: 10.1016/j.msea.2024.147625.

- [41] K. Jing *et al.*, 'Excellent high-temperature strength and ductility of the ZrC nanoparticles dispersed molybdenum', *Acta Mater*, vol. 227, Apr. 2022, doi: 10.1016/j.actamat.2022.117725.
- [42] K. Jing *et al.*, 'Enhanced mechanical properties and thermal stability of hot-rolled Mo-0.5%ZrC alloy', *Materials Science and Engineering: A*, vol. 854, Sep. 2022, doi: 10.1016/j.msea.2022.143803.
- [43] O. N. Senkov, D. B. Miracle, K. J. Chaput, and J. P. Couzinie, 'Development and exploration of refractory high entropy alloys—A review', *J Mater Res*, vol. 33, no. 19, pp. 3092–3128, Oct. 2018, doi: 10.1557/jmr.2018.153.
- [44] O. N. Senkov, S. Gorsse, and D. B. Miracle, 'High temperature strength of refractory complex concentrated alloys', *Acta Mater*, vol. 175, pp. 394–405, Aug. 2019, doi: 10.1016/j.actamat.2019.06.032.
- [45] E. N. Sheftel and O. A. Bannykh, 'Niobium—Base alloys', *Int J Refract Metals Hard Mater*, vol. 12, no. 5, pp. 303–314, Jan. 1993, doi: 10.1016/0263-4368(93)90038-H.
- [46] F. Maresca and W. A. Curtin, 'Theory of screw dislocation strengthening in random BCC alloys from dilute to "High-Entropy" alloys', *Acta Mater*, vol. 182, pp. 144–162, Jan. 2020, doi: 10.1016/j.actamat.2019.10.007.
- [47] A. Ghafarollahi and W. A. Curtin, 'Theory of kink migration in dilute BCC alloys', *Acta Mater*, vol. 215, p. 117078, Aug. 2021, doi: 10.1016/j.actamat.2021.117078.
- [48] C. Lee *et al.*, 'Strength can be controlled by edge dislocations in refractory high-entropy alloys', *Nat Commun*, vol. 12, no. 1, Dec. 2021, doi: 10.1038/s41467-021-25807-w.
- [49] S. I. Rao, C. Woodward, B. Akdim, O. N. Senkov, and D. Miracle, 'Theory of solid solution strengthening of BCC Chemically Complex Alloys', *Acta Mater*, vol. 209, May 2021, doi: 10.1016/j.actamat.2021.116758.
- [50] S. Laube *et al.*, 'Controlling crystallographic ordering in Mo–Cr–Ti–Al high entropy alloys to enhance ductility', *J Alloys Compd*, vol. 823, May 2020, doi: 10.1016/j.jallcom.2020.153805.
- [51] J. P. Couzinié and G. Dirras, 'Body-centered cubic high-entropy alloys: From processing to underlying deformation mechanisms', *Mater Charact*, vol. 147, pp. 533–544, Jan. 2019, doi: 10.1016/j.matchar.2018.07.015.
- [52] S. I. Rao *et al.*, 'Atomistic simulations of dislocations in a model BCC multicomponent concentrated solid solution alloy', *Acta Mater*, vol. 125, pp. 311–320, Feb. 2017, doi: 10.1016/j.actamat.2016.12.011.
- [53] F. Maresca and W. A. Curtin, 'Mechanistic origin of high strength in refractory BCC high entropy alloys up to 1900K', *Acta Mater*, vol. 182, pp. 235–249, Jan. 2020, doi: 10.1016/j.actamat.2019.10.015.
- [54] L. A. Gypen and A. Deruyttere, 'The combination of atomic size and elastic modulus misfit interactions in solid solution hardening', *Scripta Metallurgica*, vol. 15, no. 8, pp. 815–820, Aug. 1981, doi: 10.1016/0036-9748(81)90257-X.

- [55] T. Suzuki, 'On the studies of solid solution hardening', *Jpn J Appl Phys*, vol. 20, no. 3, p. 449, Mar. 1981, doi: 10.1143/JJAP.20.449.
- [56] R. Labusch, 'A Statistical Theory of Solid Solution Hardening', *physica status solidi (b)*, vol. 41, no. 2, pp. 659–669, Jan. 1970, doi: 10.1002/pssb.19700410221.
- [57] O. N. Senkov, J. M. Scott, S. V. Senkova, D. B. Miracle, and C. F. Woodward, 'Microstructure and room temperature properties of a high-entropy TaNbHfZrTi alloy', *J Alloys Compd*, vol. 509, no. 20, pp. 6043–6048, May 2011, doi: 10.1016/j.jallcom.2011.02.171.
- [58] X. Yang and Y. Zhang, 'Prediction of high-entropy stabilized solid-solution in multi-component alloys', *Mater Chem Phys*, vol. 132, no. 2–3, pp. 233–238, Feb. 2012, doi: 10.1016/j.matchemphys.2011.11.021.
- [59] Y. Wu *et al.*, 'Short-range ordering and its effects on mechanical properties of high-entropy alloys', *J Mater Sci Technol*, vol. 62, pp. 214–220, Feb. 2021, doi: 10.1016/j.jmst.2020.06.018.
- [60] Y. Rao and W. A. Curtin, 'Analytical models of short-range order in FCC and BCC alloys', *Acta Mater*, vol. 226, Mar. 2022, doi: 10.1016/j.actamat.2022.117621.
- [61] J. C. Fisher, 'On the strength of solid solution alloys', *Acta Metallurgica*, vol. 2, no. 1, pp. 9–10, 1954, doi: 10.1016/0001-6160(54)90087-5.
- [62] F. Körmann, A. v. Ruban, and M. H. F. Sluiter, 'Long-ranged interactions in bcc NbMoTaW high-entropy alloys', vol. 5, no. 1, pp. 35–40, Jan. 2016, doi: 10.1080/21663831.2016.1198837.
- [63] Z. Y. Wang, D. Han, and X. W. Li, 'Competitive effect of stacking fault energy and short-range clustering on the plastic deformation behavior of Cu-Ni alloys', *Materials Science and Engineering: A*, vol. 679, pp. 484–492, Jan. 2017, doi: 10.1016/j.msea.2016.10.064.
- [64] D. A. Hardwick, 'Composites Based on Molybdenum Disilicide: Progress and Prospects', *MRS*, vol. 350, no. 1, pp. 165–176, Dec. 1994, doi: 10.1557/PROC-350-165.
- [65] P. Tsakiroopoulos, 'Alloys for application at ultra-high temperatures: Nb-silicide in situ composites: Challenges, breakthroughs and opportunities', *Prog Mater Sci*, vol. 123, p. 100714, Jan. 2022, doi: 10.1016/j.pmatsci.2020.100714.
- [66] L. Jiang *et al.*, 'A Review of Mo-Si Intermetallic Compounds as Ultrahigh-Temperature Materials', *Processes 2022, Vol. 10, Page 1772*, vol. 10, no. 9, p. 1772, Sep. 2022, doi: 10.3390/pr10091772.
- [67] O. N. Senkov, J. K. Jensen, A. L. Pilchak, D. B. Miracle, and H. L. Fraser, 'Compositional variation effects on the microstructure and properties of a refractory high-entropy superalloy AlMo_{0.5}NbTa_{0.5}TiZr', *Mater Des*, vol. 139, pp. 498–511, Feb. 2018, doi: 10.1016/j.matdes.2017.11.033.
- [68] J. K. Jensen *et al.*, 'Characterization of the microstructure of the compositionally complex alloy Al₁Mo_{0.5}Nb₁Ta_{0.5}Ti₁Zr₁', *Scr Mater*, vol. 121, pp. 1–4, Aug. 2016, doi: 10.1016/j.scriptamat.2016.04.017.

- [69] V. Soni, O. N. Senkov, B. Gwalani, D. B. Miracle, and R. Banerjee, 'Microstructural Design for Improving Ductility of An Initially Brittle Refractory High Entropy Alloy', *Scientific Reports 2018 8:1*, vol. 8, no. 1, pp. 1–10, Jun. 2018, doi: 10.1038/s41598-018-27144-3.
- [70] D. B. Miracle, M. H. Tsai, O. N. Senkov, V. Soni, and R. Banerjee, 'Refractory high entropy superalloys (RSAs)', *Scr Mater*, vol. 187, pp. 445–452, Oct. 2020, doi: 10.1016/j.scriptamat.2020.06.048.
- [71] J. P. Couzinié *et al.*, 'High-temperature deformation mechanisms in a BCC+B2 refractory complex concentrated alloy', *Acta Mater*, vol. 233, p. 117995, Jul. 2022, doi: 10.1016/j.actamat.2022.117995.
- [72] O. N. Senkov, C. Woodward, and D. B. Miracle, 'Microstructure and Properties of Aluminum-Containing Refractory High-Entropy Alloys', *JOM*, vol. 66, no. 10, pp. 2030–2042, Oct. 2014, doi: 10.1007/s11837-014-1066-0.
- [73] O. N. Senkov, J. K. Jensen, A. L. Pilchak, D. B. Miracle, and H. L. Fraser, 'Compositional variation effects on the microstructure and properties of a refractory high-entropy superalloy AlMo_{0.5}NbTa_{0.5}TiZr', *Mater Des*, vol. 139, pp. 498–511, Feb. 2018, doi: 10.1016/j.matdes.2017.11.033.
- [74] V. Soni *et al.*, 'Phase inversion in a two-phase, BCC+B2, refractory high entropy alloy', *Acta Mater*, vol. 185, pp. 89–97, Feb. 2020, doi: 10.1016/j.actamat.2019.12.004.
- [75] T. E. Whitfield, E. J. Pickering, K. A. Christofidou, C. N. Jones, H. J. Stone, and N. G. Jones, 'Elucidating the microstructural development of refractory metal high entropy superalloys via the Ti–Ta–Zr constituent system', *J Alloys Compd*, vol. 818, p. 152935, Mar. 2020, doi: 10.1016/j.jallcom.2019.152935.
- [76] T. E. Whitfield *et al.*, 'An assessment of the thermal stability of refractory high entropy superalloys', *J Alloys Compd*, vol. 857, p. 157583, Mar. 2021, doi: 10.1016/j.jallcom.2020.157583.
- [77] T. E. Whitfield, E. J. Pickering, L. R. Owen, C. N. Jones, H. J. Stone, and N. G. Jones, 'The effect of Al on the formation and stability of a BCC – B2 microstructure in a refractory metal high entropy superalloy system', *Materialia*, vol. 13, p. 100858, Sep. 2020, doi: 10.1016/j.mtla.2020.100858.
- [78] J. P. Abriata and J. C. Bolcich, 'The Nb–Zr (Niobium–Zirconium) system', *Journal of Phase Equilibria 1982 3:1*, vol. 3, no. 1, pp. 34–44, Jun. 1982, doi: 10.1007/bf02873409.
- [79] A. Fernández Guillermet, 'Phase diagram and thermochemical properties of the Zr-Ta system. An assessment based on Gibbs energy modelling', *J Alloys Compd*, vol. 226, no. 1–2, pp. 174–184, Aug. 1995, doi: 10.1016/0925-8388(95)01582-5.
- [80] J. L. Li, Z. Li, Q. Wang, C. Dong, and P. K. Liaw, 'Phase-field simulation of coherent BCC/B2 microstructures in high entropy alloys', *Acta Mater*, vol. 197, pp. 10–19, Sep. 2020, doi: 10.1016/j.actamat.2020.07.030.
- [81] H. Long *et al.*, 'Effect of lattice misfit on the evolution of the dislocation structure in Ni-based single crystal superalloys during thermal exposure', *Acta Mater*, vol. 120, pp. 95–107, Nov. 2016, doi: 10.1016/j.actamat.2016.08.035.

- [82] H. Long *et al.*, 'A comparative study of rafting mechanisms of Ni-based single crystal superalloys', *Mater Des*, vol. 196, p. 109097, Nov. 2020, doi: 10.1016/j.matdes.2020.109097.
- [83] D. Dye, A. Ma, and R. C. Reed, 'Numerical modelling of creep deformation in a CMSX-4 single crystal superalloy turbine blade', *superalloys*, vol. 911, p. e919, 2008, doi: 10.7449/2008/Superalloys_2008_911_919.
- [84] RT. Begley, WN. Platte, AI. Lewis, RL. Ammon, 'Development of niobium-base alloys (Technical Report) | OSTI.GOV', No. WADC-TR-57-344 (Pt. V). Westinghouse Electric Corp. Research Labs. Pittsburgh, 1961.
- [85] K. Jing *et al.*, 'Excellent high-temperature strength and ductility of the ZrC nanoparticles dispersed molybdenum', *Acta Mater*, vol. 227, pp. 117752, Nov. 2016, doi: 10.1016/j.actamat.2022.117725.
- [86] WD. Kloop, 'A review of chromium, molybdenum, and tungsten alloys', *Journal of the Less Common Metals*, vol. 42, no.3, pp. 261-278, Oct. 1975, doi: 10.1016/0022-5088(75)90046-6.
- [87] O. N. Senkov, D. B. Miracle, and S. I. Rao, 'Correlations to improve room temperature ductility of refractory complex concentrated alloys', *Materials Science and Engineering A*, vol. 820, Jul. 2021, doi: 10.1016/j.msea.2021.141512.
- [88] D. G. Pettifor, 'Theoretical predictions of structure and related properties of intermetallics', vol. 8, no. 4, pp. 345–349, 2013, doi: 10.1179/mst.1992.8.4.345.
- [89] D. G. Pettifor, 'New many-body potential for the bond order', *Phys Rev Lett*, vol. 63, no. 22, pp. 2480–2483, 1989, doi: 10.1103/PhysRevLett.63.2480.
- [90] S. F. Pugh, 'XCII. Relations between the elastic moduli and the plastic properties of polycrystalline pure metals', vol. 45, no. 367, pp. 823–843, Aug. 2009, doi: 10.1080/14786440808520496.
- [91] O. N. Senkov and D. B. Miracle, 'Generalization of intrinsic ductile-to-brittle criteria by Pugh and Pettifor for materials with a cubic crystal structure', *Scientific Reports* |, vol. 11, p. 4531, 123AD, doi: 10.1038/s41598-021-83953-z.
- [92] S. Sheikh, S. Shafeie, and Q. Hu, 'Alloy design for intrinsically ductile refractory high-entropy alloys', *J. Appl. Phys*, vol. 120, p. 164902, 2016, doi: 10.1063/1.4966659.
- [93] J. R. Rice and R. Thomson, 'Ductile versus brittle behaviour of crystals', vol. 29, no. 1, pp. 73–97, 2006, doi: 10.1080/14786437408213555.
- [94] H. P. Cahn RW, Ed., 'Structure of intermetallic compounds and phases', *Physical metallurgy*, pp.205-369, Jan. 1996.
- [95] T. B. Massalski, 'Comments Concerning Some Features of Phase Diagrams and Phase Transformations', *Mater Trans*, vol. 51, no. 4, pp. 583-596, Apr. 2010, doi: 10.2320/matertrans.M2010012.
- [96] U. Mizutani, 'Hume-Rothery rules for structurally complex alloy phases', *MRS Bulletin-Materials Research Society*, vol. 37, no. 2, pp: 169, 2012.

- [97] H. L. Liang, C. W. Tsai, and S. Guo, 'Design of corrosion-resistant high-entropy alloys through valence electron concentration and new PHACOMP', *J Alloys Compd*, vol. 883, p. 160787, Nov. 2021, doi: 10.1016/j.jallcom.2021.160787.
- [98] R. Gibala and T. E. Mitchell, 'Solid solution softening and hardening', *Scripta Metallurgica*, vol. 7, no. 11, pp. 1143–1148, Nov. 1973, doi: 10.1016/0036-9748(73)90236-6.
- [99] A. Sato and M. Meshii, 'Solid solution softening and solid solution hardening', *Acta Metallurgica*, vol. 21, no. 6, pp. 753–768, Jun. 1973, doi: 10.1016/0001-6160(73)90040-0.
- [100] B. v. Petukhov, 'Effect of solid-solution softening of crystalline materials: Review', *Crystallography Reports 2007 52:1*, vol. 52, no. 1, pp. 112–122, Feb. 2007, doi: 10.1134/s1063774507010130.
- [101] E. Pink and R. J. Arsenault, 'Low-temperature softening in body-centered cubic alloys', *Prog Mater Sci*, vol. 24, no. C, pp. 1–50, Jan. 1980, doi: 10.1016/0079-6425(79)90003-3.
- [102] P. Meneses and G. Champier, 'On the Mechanical Behavior of Fe-Mo Alloys', *Journal of the Society of Materials Science, Japan*, vol. 21, no. 231, pp. 1071–1074, Dec. 1972, doi: 10.2472/jsms.21.1071.
- [103] J. R. Stephens and W. R. Witzke, 'Alloy softening in binary iron solid solutions', *Journal of The Less-Common Metals*, vol. 48, no. 2, pp. 285–308, 1976, doi: 10.1016/0022-5088(76)90009-6.
- [104] E. Pink, 'Legierungsentfestigung in kubisch-raumzentrierten Metallen.', *International Journal of Materials Research*, vol. 64, no. 12, pp. 871–881, Dec. 1973, doi: doi.org/10.1515/ijmr-1973-641209.
- [105] R. J. Arsenault, 'Solid solution strengthening and weakening of b.c.c. solid solutions', *Acta Metallurgica*, vol. 17, no. 10, pp. 1291–1297, 1969, doi: 10.1016/0001-6160(69)90144-8.
- [106] M. G. Ulitchny, A. A. Sagues, and R. Gibala, 'Alloy softening in niobium-and tantalum-base solid solutions', No. INIS-MF--392. 1972, 1972.
- [107] S. I. Rao, C. Woodward, and B. Akdim, 'Solid solution softening and hardening in binary BCC alloys', *Acta Mater*, p. 118440, Oct. 2022, doi: 10.1016/j.actamat.2022.118440.
- [108] Y. J. Hu *et al.*, 'Solute-induced solid-solution softening and hardening in bcc tungsten', *Acta Mater*, vol. 141, pp. 304–316, Dec. 2017, doi: 10.1016/j.actamat.2017.09.019.
- [109] W. Hume-Rothery and G. Raynor, 'The structure of metals and alloys'. *Institute of metals*, pp. 98-105, Jul. 1936.
- [110] J. R. Stephens and W. R. Witzke, 'The role of electron concentration in softening and hardening of ternary molybdenum alloys', *Journal of The Less-Common Metals*, vol. 41, no. 2, pp. 265–282, 1975, doi: 10.1016/0022-5088(75)90033-8.
- [111] N. I. Medvedeva, Y. N. Gornostyrev, and A. J. Freeman, 'Solid solution softening and hardening in the group-V and group-VI bcc transition metals alloys: First principles

- calculations and atomistic modeling', *Phys Rev B Condens Matter Mater Phys*, vol. 76, no. 21, p. 212104, Dec. 2007, doi: 10.1103/PhysRevB.76.212104.
- [112] N. I. Medvedeva, Y. N. Gornostyrev, and A. J. Freeman, 'Solid solution softening in bcc Mo alloys: Effect of transition-metal additions on dislocation structure and mobility', *Phys Rev B Condens Matter Mater Phys*, vol. 72, no. 13, p. 134107, Oct. 2005, doi: 10.1103/PhysRevB.72.134107.
- [113] D. R. Trinkle and C. Woodward, 'Materials science: The chemistry of deformation: How solutes soften pure metals', *Science (1979)*, vol. 310, no. 5754, pp. 1665–1667, Dec. 2005, doi: 10.1126/Science.1118616.
- [114] M. G. Ulitschny and R. Gibala, 'The effects of interstitial solute additions on the mechanical properties of niobium and tantalum single crystals', *Journal of The Less-Common Metals*, vol. 33, no. 1, pp. 105–116, 1973, doi: 10.1016/0022-5088(73)90061-1.
- [115] J. A. Shields, R. Gibala, and T. E. Mitchell, 'Dislocation substructure in Ta-Re-N alloys deformed at 77 K', *Metallurgical Transactions A 1976 7:8*, vol. 7, no. 8, pp. 1111–1121, 1976, doi: 10.1007/bf02656593.
- [116] 'Ellingham Diagrams'. Available: https://www.academia.edu/31529802/Ellingham_Diagrams
- [117] D. Young, '*High temperature oxidation and corrosion of metals*', vol. 1, 2008, Elsevier.
- [118] C. Xu and W. Gao, 'Pilling-Bedworth ratio for oxidation of alloys', *Mat. Res. Innovat.*, vol. 3, no. 4, pp. 231–235, 2000, doi: 10.1007/s100190050008.
- [119] W. Klopp, D. Maykuth, C. Sims, and R. Jaffee, 'Oxidation and contamination reactions of niobium and niobium alloys', No. BMI-1317. Battelle Memorial Inst., Columbus, OH (United States), Feb. 1959.
- [120] J. James, J. Spittle, S. Brown, 'A review of measurement techniques for the thermal expansion coefficient of metals and alloys at elevated temperatures', *Measurement science and technology*, vol. 12, no. 3, p. R1, Mar. 2001, doi: 10.1088/0957-0233/12/3/201.
- [121] W. Knabl, G. Leichtfried, and R. Stickler, 'Refractory metals and refractory metal alloys', *Springer Handbooks*, pp. 303–333, 2018, doi: 10.1007/978-3-319-69743-7_13.
- [122] C. Leyens and M. Peters, '*Titanium and titanium alloys: fundamentals and applications*', Wiley-VCH, 2003.
- [123] S. Sheikh, L. Gan, X. Montero, H. Murakami, and S. Guo, 'Forming protective alumina scale for ductile refractory high-entropy alloys via aluminizing', *Intermetallics*, vol. 123, Aug. 2020, doi: 10.1016/j.intermet.2020.106838.
- [124] Y. Yamamoto *et al.*, 'Creep-resistant, Al₂O₃-forming austenitic stainless steels', *Science (1979)*, vol. 316, no. 5823, pp. 433–436, Apr. 2007, doi: 10.1126/SCIENCE.1137711.
- [125] P. Tsakiroopoulos, 'Alloys for application at ultra-high temperatures: Nb-silicide in situ composites: Challenges, breakthroughs and opportunities', *Prog Mater Sci*, vol. 123, p. 100714, Jan. 2022, doi: 10.1016/j.pmatsci.2020.100714.

- [126] F. Müller, B. Gorr, H. J. Christ, H. Chen, A. Kauffmann, and M. Heilmaier, 'Effect of microalloying with silicon on high temperature oxidation resistance of novel refractory high-entropy alloy Ta-Mo-Cr-Ti-Al', *Materials at High Temperatures*, vol. 35, no. 1–3, pp. 168–176, May 2018, doi: 10.1080/09603409.2017.1389115.
- [127] H. Chen *et al.*, 'Microstructure and mechanical properties at elevated temperatures of a new Al-containing refractory high-entropy alloy Nb-Mo-Cr-Ti-Al', *J Alloys Compd*, vol. 661, pp. 206–215, Mar. 2016, doi: 10.1016/j.jallcom.2015.11.050.
- [128] S. Sheikh *et al.*, 'Accelerated oxidation in ductile refractory high-entropy alloys', *Intermetallics*, vol. 97, pp. 58–66, Jun. 2018, doi: 10.1016/j.intermet.2018.04.001.
- [129] S. Sheikh, L. Gan, T. K. Tsao, H. Murakami, S. Shafeie, and S. Guo, 'Aluminizing for enhanced oxidation resistance of ductile refractory high-entropy alloys', *Intermetallics*, vol. 103, pp. 40–51, Dec. 2018, doi: 10.1016/j.intermet.2018.10.004.
- [130] B. Gorr, S. Schellert, F. Müller, H. J. Christ, A. Kauffmann, and M. Heilmaier, 'Current Status of Research on the Oxidation Behavior of Refractory High Entropy Alloys', *Adv Eng Mater*, vol. 23, no. 5, p. 2001047, May 2021, doi: 10.1002/adem.202001047.
- [131] K. C. Lo, Y. J. Chang, H. Murakami, J. W. Yeh, and A. C. Yeh, 'An oxidation resistant refractory high entropy alloy protected by CrTaO₄-based oxide', *Scientific Reports 2019 9:1*, vol. 9, no. 1, pp. 1–12, May 2019, doi: 10.1038/s41598-019-43819-x.
- [132] E. A. Anber *et al.*, 'Oxidation resistance of Al-containing refractory high-entropy alloys', *Scr Mater*, vol. 244, Apr. 2024, doi: 10.1016/j.scriptamat.2024.115997.
- [133] L. Backman and E. J. Opila, 'Thermodynamic assessment of the group IV, V and VI oxides for the design of oxidation resistant multi-principal component materials', *J Eur Ceram Soc*, vol. 39, no. 5, pp. 1796–1802, May 2019, doi: 10.1016/j.jeurceramsoc.2018.11.004.
- [134] S. Gorsse, W. C. Lin, H. Murakami, G. M. Rignanese, and A. C. Yeh, 'Advancing refractory high entropy alloy development with Al-predictive models for high temperature oxidation resistance', *Scr Mater*, vol. 255, Jan. 2025, doi: 10.1016/j.scriptamat.2024.116394.
- [135] B. Gorr, S. Schellert, F. Müller, H. J. Christ, A. Kauffmann, and M. Heilmaier, 'Current Status of Research on the Oxidation Behavior of Refractory High Entropy Alloys', *Adv Eng Mater*, vol. 23, no. 5, p. 2001047, May 2021, doi: 10.1002/adem.202001047.
- [136] B. Gorr *et al.*, 'Development of oxidation resistant refractory high entropy alloys for high temperature applications: Recent results and development strategy', *Minerals, Metals and Materials Series*, vol. Part F12, pp. 648–659, 2018, doi: 10.1007/978-3-319-72526-0_61.
- [137] F. Müller *et al.*, 'On the oxidation mechanism of refractory high entropy alloys', *Corros Sci*, vol. 159, p. 108161, Oct. 2019, doi: 10.1016/j.corsci.2019.108161.
- [138] K. C. Lo, Y. J. Chang, H. Murakami, J. W. Yeh, and A. C. Yeh, 'An oxidation resistant refractory high entropy alloy protected by CrTaO₄ -based oxide', *Sci Rep*, vol. 9, no. 1, Dec. 2019, doi: 10.1038/s41598-019-43819-x.

- [139] B. Gorr *et al.*, 'A new strategy to intrinsically protect refractory metal based alloys at ultra high temperatures', *Corros Sci*, vol. 166, p. 108475, Apr. 2020, doi: 10.1016/j.corsci.2020.108475.
- [140] P. Kofstad and K. P. Lillerud, 'Chromium transport through Cr₂O₃ scales I. On lattice diffusion of chromium', *Oxidation of Metals*, vol. 17, no. 3–4, pp. 177–194, Apr. 1982, doi: 10.1007/BF00738381.
- [141] N. Birks, G. Meier, and F. Pettit, *Introduction to the high temperature oxidation of metals*, Cambridge university press, Mar. 2006.
- [142] O. A. Waseem, U. Auyeskan, H. M. Lee, and H. J. Ryu, 'A combinatorial approach for the synthesis and analysis of AlxCr_yMozNbTiZr high-entropy alloys: Oxidation behavior', *J Mater Res*, vol. 33, no. 19, pp. 3226–3234, Oct. 2018, doi: 10.1557/jmr.2018.241/TABLES/4.
- [143] T. M. Butler and M. L. Weaver, 'Oxidation behavior of arc melted AlCoCrFeNi multi-component high-entropy alloys', *J Alloys Compd*, vol. 674, pp. 229–244, Jul. 2016, doi: 10.1016/j.jallcom.2016.02.257.
- [144] X. Yang *et al.*, 'Effect of Al content on the thermal oxidation behaviour of AlHfMoNbTi high-entropy alloys analysed by in situ environmental TEM', *Corros Sci*, vol. 191, p. 109711, Oct. 2021, doi: 10.1016/j.corsci.2021.109711.
- [145] K. Stern, *Metallurgical and ceramic protective coatings*, Springer Science & Business Media, Aug. 1996.
- [146] S. Wöllmer, S. Zaefferer, M. Göken, T. Mack, and U. Glatzel, 'Characterization of phases of aluminized nickel base superalloys', *Surf Coat Technol*, vol. 167, no. 1, pp. 83–96, Apr. 2003, doi: 10.1016/S0257-8972(02)00843-5.
- [147] H. Li, M. Qiao, and C. Zhou, 'Formation and cyclic oxidation resistance of Hf–Co-modified aluminide coatings on nickel base superalloys', *Mater Chem Phys*, vol. 143, no. 3, pp. 915–920, Feb. 2014, doi: 10.1016/j.matchemphys.2013.09.016.
- [148] Y. Yamamoto *et al.*, 'Creep-resistant, Al₂O₃-forming austenitic stainless steels', *Science (1979)*, vol. 316, no. 5823, pp. 433–436, Apr. 2007, doi: 10.1126/SCIENCE.1137711.
- [149] S. Sheikh, L. Gan, T. K. Tsao, H. Murakami, S. Shafeie, and S. Guo, 'Aluminizing for enhanced oxidation resistance of ductile refractory high-entropy alloys', *Intermetallics*, vol. 103, pp. 40–51, Dec. 2018, doi: 10.1016/j.intermet.2018.10.004.
- [150] S. Sheikh, L. Gan, X. Montero, H. Murakami, and S. Guo, 'Forming protective alumina scale for ductile refractory high-entropy alloys via aluminizing', *Intermetallics*, vol. 123, p. 106838, Aug. 2020, doi: 10.1016/j.intermet.2020.106838.
- [151] L. Backman, J. Gild, J. Luo, and E. J. Opila, 'Part I: Theoretical predictions of preferential oxidation in refractory high entropy materials', *Acta Mater*, vol. 197, pp. 20–27, Sep. 2020, doi: 10.1016/j.actamat.2020.07.003.
- [152] L. Backman, J. Gild, J. Luo, and E. J. Opila, 'Part II: Experimental verification of computationally predicted preferential oxidation of refractory high entropy ultra-high temperature ceramics', *Acta Mater*, vol. 197, pp. 81–90, Sep. 2020, doi: 10.1016/j.actamat.2020.07.004.

- [153] 'ISO - ISO 6507-1:2005 - Metallic materials — Vickers hardness test — Part 1: Test method'.
- [154] A. Kelly, KM. Knowles, '*Crystallography and Crystal Defects*', John Wiley & Sons, Jun. 2020.
- [155] J. Goldstein, '*Practical scanning electron microscopy: electron and ion microprobe analysis*', Springer Science & Business Media, Dec. 2012.
- [156] G. Taylor, 'Thermally-activated deformation of BCC metals and alloys', *Prog Mater Sci*, vol. 36, pp. 29–61, Jan. 1992, doi: 10.1016/0079-6425(92)90004-Q.
- [157] F. G. Coury, '*Solid solution Strengthening in HEAs*', PhD Thesis, pp. 1–140, 2018.
- [158] F. Schwartzberg, H. Ogden, and R. Jaffee, '*Ductile-brittle transition in the refractory metals*', Defense Metals Information Center, Battelle Memorial Institute, vol. 114, 1959.